Alma Mater Studiorum – Università di Bologna
in cotutela con Università Abdelmalek Essaadi

DOTTORATO DI RICERCA IN CHIMICA

Ciclo XXXII

Settore Concorsuale: 03/B1

Settore Scientifico Disciplinare: CHIM/03

TOWARDS CHEAPER, SAFER AND LOW ENVIRONMENTAL IMPACT MATERIALS FOR ENERGY STORAGE DEVICES: NATURAL RESOURCES-DERIVED CARBON BASED ELCETRODES AND AQUEOUS ELECTROLYTES FOR SUPERCAPACITORS

Presentata da: Mohammad Said El Halimi

Coordinatore Dottorato

Prof. Domenica Tonelli

Supervisors

Prof. Francesca Soavi
Prof. Tarik Chafik

Esame finale anno 2022

ALMA MATER STUDIORUM
UNIVERSITÀ DI BOLOGNA

Towards Cheaper, Safer and Low Environmental Impact Materials for Energy Storage Devices: Natural Resources-Derived Carbon Based Electrodes and Aqueous Electrolytes for Supercapacitors

Thesis submitted in partial fulfillment of the requirements for the degree of Doctor of Philosophy in Chemistry, at the University of Bologna

Mohammad Said El Halimi

Supervisors:
Professor Francesca Soavi
Professor Tarik Chafik

LEME - Laboratory of Electrochemistry of Materials for Energetics
Department of Chemistry "Giacomo Ciamician", University of Bologna

LGCVR - Laboratory of Chemical Engineering and Ressources Valorization
Faculty of Sciences and Techniques of Tangier, Abdelmalek Essaadi University

"وَلَسَوْفَ يُعْطِيكَ رَبُّكَ فَتَرْضَىٰٓ"

— (سورة الضحى - الآية 5)

"No honor is like knowledge."

— Ali ibn Abi Talib

"La sapienza è figliola dell'esperienza."

— Leonardo da Vinci

Abstract

The growing market of electrical cars, portable electronics, photovoltaic systems..etc. requires the development of efficient, low-cost, and low environmental impact energy storage devices (ESDs) including batteries and supercapacitors.. Due to their extended charge-discharge cycle, high specific capacitance, and power capabilities supercapacitors are considered among the most attractive ESDs. Over the last decade, research and development in supercapacitor technology has accelerated: thousands of articles have been published in the literature describing the electrochemical properties of the electrode materials and electrolyte in addition to separators and current collectors. Carbon-based supercapacitor electrodes materials have gained increasing attention due to their high specific surface area, good electrical conductivity, and excellent stability in harsh environments, as well as other characteristics. Recently, there has been a surge of interest in activated carbon derived from low-cost abundant sources such as biomass for supercapacitor electrode materials. Also, particular attention was given to a major challenging issue concerning the substitution of organic solutions currently used as electrolytes due of their highest electrochemical stability window even thought their high cost, toxicity and flammability.

At this regard, the main objective of this thesis is to investigate the performances of supercapacitors using low cost abundant safe and low environmental impact materials for electrodes and electrolyte. Several prototypes were constructed and tested using natural resources through optimization of the preparation of appropriate carbon electrodes using agriculture by-products waste or coal (i.e. Argan shell or Anthracite from Jerrada). Such electrodes were tested using several electrolytes formulation (aqueous and water in salt electrolytes) beneficing their non-flammability, lower cost and environmental impact; the characteristics that provide a promising opportunity to design safer inexpensive and environmental friendly devices compared to organic electrolytes.

Keywords: Supercapacitor, Nanoporous activated carbon, argan shells, anthracite, aqueous electrolytes, ammonium acetate water in salt electrolyte

Abstract

Il mercato in crescita delle auto elettriche, dell'elettronica portatile, degli impianti fotovoltaici, ecc. richiede lo sviluppo di dispositivi di accumulo di energia (ESD) efficienti, a basso costo e a basso impatto ambientale, come batterie e supercondensatori. A causa della loro lunga vita di ciclo, dell'elevata capacitanza e potenza specifiche, i supercondensatori sono considerati tra gli ESD più interessanti . Nell'ultimo decennio, la ricerca e lo sviluppo della tecnologia dei supercondensatori hanno subito un'accelerazione: in letteratura sono stati pubblicati migliaia di articoli che descrivono le proprietà elettrochimiche dei materiali elettrodici ed elettrolitici, dei separatori e collettori di corrente. Gli elettrodi per supercondensatori a base di carbone hanno guadagnato crescente attenzione grazie alla loro elevata area superficiale specifica, buona conduttività elettrica ed eccellente stabilità chimica. Recentemente, e' crescuito l'interesse verso carboni attivati derivati da fonti abbondanti a basso costo come la biomassa di scarto per realizzare componenti elettrodiche di supercondensatori. Inoltre, è sempre piu' alta l'attenzione verso la sostituzione delle soluzioni organiche attualmente utilizzate come elettroliti per il loro costo, tossicità e infiammabilità elevati.

A questo proposito, l'obiettivo principale di questa tesi è quello di indagare le prestazioni dei supercondensatori utilizzando materiali a basso costo, abbondanti, sicuri e a basso impatto ambientale per elettrodi ed elettroliti. Diversi prototipi sono stati costruiti e testati utilizzando risorse naturali attraverso l'ottimizzazione della preparazione di elettrodi di carbone utilizzando scarti di sottoprodotti dell'agricoltura o carbone naturale (ad esempio guscio di argan o antracite di Jerrada). Tali elettrodi sono stati testati utilizzando diverse formulazioni di elettroliti acquosi selezionati per la loro non infiammabilità e minor costo e impatto ambientale, caratteristiche che offrono un'opportunità promettente per progettare dispositivi più sicuri, economici e rispettosi dell'ambiente rispetto agli elettroliti organici.

Parole chiave: Supercondensatore; Carbone attivo nanoporoso; Biomassa, gusci di argan, antracite, elettroliti acquosi, acetato di ammonio, elettrolita wáter in salt

الملخص

االسوق المتنامي للسيارات الكهربائية والإلكترونيات المحمولة والأنظمة الكهروضوئية .. إلخ. يتطلب تطوير أجهزة تخزين طاقة فعالة، منخفضة التكلفة، ومنخفضة التأثير على البيئة بما في ذلك البطاريات والمكثفات الفائقة ... نظرًا لدورة تفريغ الشحن الممتدة ، والسعة النوعية العالية ، وقدرات الطاقة تعتبر المكثفات الفائقة من بين أكثر أجهزة التخزين جاذبية. على مدار العقد الماضي ، تسارعت عمليات البحث والتطوير في مجال تكنولوجيا المكثف الفائق: تم نشر آلاف المقالات في الأدبيات التي تصف الخصائص الكهروكيميائية لمواد الإلكترود والإلكتروليت بالإضافة إلى الفواصل ومجمعات التيار. اكتسبت مواد أ قطاب المكثفات الفائقة القائمة على الكربون اهتمامًا متزايدًا نظرًا لمساحة سطحها العالية ، والتوصيل الكهربائي الجيد ، والاستقرار الممتاز في البيئات القاسية ، فضلاً عن الخصائص الأخرى. في الآونة الأخيرة ، كان هناك زيادة في الاهتمام بالكربون المنشط المشتق من مصادر وفيرة منخفضة التكلفة مثل الكتلة الحيوية لمواد القطب الفائق المكثف. أيضًا ، تم إيلاء اهتمام خاص لمسألة التحدي الرئيسية المتعلقة باستبدال المحاليل العضوية المستخدمة حاليًا كإلكتروليتات نظرًا لأعلى نافذة استقرارها كهروكيميائي رغم تكلفتها العالية وسميتها وقابليتها للاشتعال.

في هذا الصدد ، الهدف الرئيسي من هذه الأطروحة هو التحقيق في أداء المكثفات الفائقة باستخدام مواد منخفضة التكلفة وآمنة ومنخفضة التأثير على البيئة للأقطاب الكهربائية والإلكتروليت. تم إنشاء العديد من النماذج الأولية واختبارها باستخدام الموارد الطبيعية من خلال تحسين إعداد أقطاب الكربون المناسبة باستخدام المنتجات الثانوية الزراعية أو نفايات الفحم (مثل قشرة الأركان أو الفحم الحجري لمنطقة جرادة). تم اختبار هذه الأقطاب الكهربائية باستخدام العديد من تركيبات الإلكتروليت (مائية وماء في إلكتروليتات ملحية) استفادة من عدم قابليتها للاشتعال وانخفاض التكلفة وتأثيرها على البيئة ؛ الخصائص التي توفر فرصة واعدة لتصميم أجهزة أكثر أمانًا وغير مكلفة وصديقة للبيئة مقارنة بالإلكتروليتات العضوية.

الكلمات الرئيسية: المكثف الفائق ، الكربون المنشط النانوي ، قشور الأركان ، الفحم الحجري ، الإلكتروليتات المائية ، ماء أسيتات الأمونيوم في إلكتروليت الملح

Résumé

Le marché croissant des voitures électriques, de l'électronique portable, des systèmes photovoltaïques, etc. nécessite le développement de dispositifs de stockage d'énergie (ESD) efficaces, peu coûteux et à faible impact sur l'environnement, y compris des batteries et des supercondensateurs . Au cours de la dernière décennie, la recherche et le développement dans la technologie des supercondensateurs se sont accélérés : des milliers d'articles ont été publiés dans la littérature décrivant les propriétés électrochimiques des matériaux d'électrode et de l'électrolyte en plus des séparateurs et des collecteurs de courant. Les matériaux d'électrodes de supercondensateurs à base de carbone ont attiré une attention croissante en raison de leur surface spécifique élevée, de leur bonne conductivité électrique et de leur excellente stabilité dans les environnements difficiles, ainsi que d'autres caractéristiques. Récemment, il y a eu un regain d'intérêt pour le charbon actif dérivé de sources abondantes à faible coût telles que la biomasse pour les matériaux d'électrode de supercondensateur. En outre, une attention particulière a été accordée à un défi majeur concernant la substitution des solutions organiques actuellement utilisées comme électrolytes en raison de leur fenêtre de stabilité électrochimique la plus élevée, même en dépit de leur coût élevé, de leur toxicité et de leur inflammabilité.

À cet égard, l'objectif principal de cette thèse est d'étudier les performances des supercondensateurs utilisant des matériaux abondants à faible coût, sûrs et à faible impact environnemental pour les électrodes et l'électrolyte. Plusieurs prototypes ont été construits grâce à l'optimisation de la préparation d'électrodes de carbone appropriées à partir des ressources naturelles comme des déchets de sous-produits agricoles ou de charbon (la coque d'Argan ou l'anthracite de Jerrada).

Ces électrodes ont été testées à l'aide de plusieurs formulations d'électrolytes (électrolytes aqueux et les électrolytes aqueux concentrés, appelés « water-in-salt ») bénéficiant de leur ininflammabilité, leur faible coût et de leur impact environnemental, les caractéristiques qui offrent une opportunité prometteuse de concevoir des dispositifs plus sûrs, peu coûteux et respectueux de l'environnement par rapport aux électrolytes organiques.

Mots-clés : Supercondensateur, Charbon actif nanoporeux, coques d'argan, anthracite, électrolytes aqueux, acétate d'ammonium water in salt électrolyte

Acknowledgment

Above all, I thank Allah (God) for providing me with strength, courage, and the ability to complete this work successfully.

My heartfelt appreciation goes out to my wonderful family, who have given me unconditional love and support through every stage of my life.

I would like to express my sincere gratitude to my principal supervisors Prof. Francesca Soavi and Prof. Tarik Chafik, their passion and enthusiasm in research has encouraged me to learn new skills and to gain new knowledge beyond my research field. Their patient guidance, encouragement, and support throughout my whole PhD journey has made my study and life easier. Without their help and mentoring, it is hard to imagine how I can pass through the obstacles that I encountered in the past years.

I acknowledge the LGCVR Laboratory (Laboratory of Chemical Engineering and Valorisation of Resources) at Abdelmalek Essaadi University and the Associate Laboratory LEME (Laboratory of Electrochemistry of Materials for Energetics) at University of Bologna for all the resources available to me during this thesis. I also thank the directors Prof. Tarik Chafik and Prof. Catia Arbizzani, and all the professors and the researchers of these institutions for their availability and assistance.

The following entities and projects are acknowledged for providing the material support for the fulfilment of the present thesis research: The Minister for Higher Education, Scientific Research and Executive Training-Morocco. The Ministry of Foreign Affairs and International Cooperation-Italy. The National Centre for Scientific and Technical Research (PPR2 16/17 project CNRST Morocco). The Italy-South Africa joint Research Program 2018–2020 (Italian Ministers of Foreign Affairs and of the Environments). The bilateral project CNR Italy-CNRST Morocco "Green Supercapacitors" (SAC.AD002.014, n. 7974, C.U.P. B54I20000790005). Erasmus+ Program (European Commission)-Mobility scholarship (Mobility 3+).

I am thankful to Prof. Agustín Pérez-Cadenas and Prof. Francisco Carrasco-Marín for accepting and helping me during my stay within "Carbon Research Group", Department of Inorganic Chemistry, University of Granada. Their help and technical advices helped me to gain significant experiences in both based carbon material synthesis and electrochemical experimentation. ¡muchas gracias!

I am grateful also to Prof. Carlo Santoro at the University of Milan Bicocca for his helpful discussion and advice on the work during several meetings, *and for supporting my applications for the project funding.*

I want to thanks my colleague Ouassim Boujibar a former PhD student at LGCVR Tangier currently Post doc at laboratory of Physico-Chimie des Matériaux et des Electrolytes pour l'Energie - PCM2, Université de Tours, France, for for the assistance regarding the textural-structural characterization of the prepared carbon materials.

Also, I would like to thank Prof. Matteo Calvaresi and Edoardo Jun Mattioli from the NanoBio Interface Laboratory, Department of Chemistry "Giacomo Ciamician", at University of Bologna for their great collaboration and help concerning the Molecular Dynamic (MD) simulation study.

During this journey, I and blessed to meet great people and friends:

- *For my colleagues at LGCVR and at the department of Chemistry, Faculty of Sciences and Techniques of Tangier: Mouad, Hanane, Ahmed, Khadija, Zoubair, Mounir, Houdaifa, Mohamed, Hamza, Bilal. I want to say 'شكرا على كل شيء'.*

- *For my compañeros at Carbon Research Group, University of Granada: Jssica, Jemina, Diana, Dr. Louisa, Dr. Sergio, Safae, and Núria "Gracias por los buenos recuerdos".*

- *For i miei colleghi at LEME: Federico, Giovanni, Dr. F. De Giorgio, Dr. M. Meshkour, Dr. M. Rahmonipoor, Bora, Pietro, Tomasso, Luigi, Ramona, Alessandro, Nicola, A. Brilloni, Giampaolo,"Vorrei ringraziarti per la tua gentilezza, grazie per tutti I momenti indimenticabile di gioie e dello scambio* culturale".

In Tangier, I would thank my cousin Naoufal who helped me a lot during those years. Also, for my friends: Aymane, Abdalah, Hamza, Zakaria, Ibrahim, Ismail, Abdellah, Mohamed, Azdine, Ismail, Reda, Abdeleilah, Yassin, Hicham, Reda and Abderahim "Thanks for the strong friendship that gathered us"

In Granada, I would thank my dear friend Mustapha who hosted me in my first days there. Also, this stay allowed me to meet many friends from different countries: For, Salmane, Bendehiba, Hashem, Mohamed, and Zakaria 'شكرا' our adventures in Andalucia will never be forgotten. Paolo "grazie" and Rodolfo "gracias" our ski trips will be always remembered, Obaid "rahmat", Bruno "obrigado" for the great time we spent together in Granada.

In Bologna, I would thank my dear friends Hakim, Ahmed, Lotfi and Youssef, who helped me in my first days there. Also, I want to express my heartfelt gratitude for the landlord Mr. Abo Ali that welcomed me like a family member and provided a great stay in his apartment. I am also grateful to my neighbors: Said, Zakaria, Haj Omar and Haj Abdesalam, and my friends: Dr. Karam, Dr. Mohamed, Dr.Elsayed, Mohanad, Ahmed, Khalil, Mouath, Abdelah and Mahmoud for all the beautiful days we spent together in Bologna.

المركز الوطني للبحث العلمي والتقني
Centre National pour la Recherche Scientifique et Technique

Ministero degli Affari Esteri e della Cooperazione Internazionale
FARNESINA

MINISTERO DELL'AMBIENTE
E DELLA TUTELA DEL TERRITORIO E DEL MARE

Erasmus+

Consiglio Nazionale delle Ricerche

TABLE OF CONTENTS

LIST OF TABLES

LIST OF FIGURES

LIST OF ABBREVIATIONS

A	Ampere
AC	Activated Carbon
ACN/TEABF4	Tetraethylammonium Tetrafluoroborate In Acetonitrile
AmAc	Ammonium Acetate
ATR	Attenuated Total Reflection
ATR-FTIR	Attenuated Total Reflection Fourier Transform Infrared Spectroscopy
BET	Brunauer-Emmett-Teller Theory
CNT	Carbon Nanotubes
CV	Cyclic Voltammetry
DFT	Density Functional Theory
EDL	Electrochemical Double Layer
EIS	Electrochemical Impedance Spectroscopy
EMITFSI	1-Ethyl-3-methylimidazolium bis-(trifluoromethylsulfonyl)-imide
ESW	Electrochemical Stability Window
EDLC	Electrostatic Double-Layer Capacitors
EDSs	Energy Storage Devices
Eq	Equation
ESR	Equivalent Series Resistance
EDL	Electrochemical Double Layer
EIS	Electrochemical Impedance Spectroscopy
ESW	Electrochemical Stability Window
EDLC	Electrostatic Double-Layer Capacitors
EDSs	Energy Storage Devices
EAN	Ethylammonium Nitrate
F	Farad
FTIR	Fourier Transform Infrared Spectroscopy
GCD	alvanostatic Charge-Discharge
GC	Glassy Carbon Electrode

GHG	Greenhouse Gas
H	Hour
HCL	Chloridric Acid
HSC	Hybrid Supercapacitors
IM	Impregnation Method
IR	Infrared Spectroscopy
ICDD	International Center For Diffraction Data
IUPAC	International Union Of Pure And Applied
LSV	Linear Sweep Voltammetry
LiTFS	Lithium Bis(Trifluoromethane)Sulfonimide
LP30	Lithium Hexafluorophosphate In Ethylene Carbonate And Dimethyl Carbonate
M	Molar Concentration
MD	Molecular Dynamic Simulation
KOH	Potassium Hydroxide
[PP13][TFSI]	N-Methyl-N-Propylpiperidinium Bis(Trifluoromethanesulfonyl) Imide:
PM	Physical Mixing Methode
PTFE	Poly(Tetrafluoroethylene) Binder
PYR14TFSI	PYR14TFSI
PSD	Pores Size Distribution
PC	Pseudocapacitors
RT	Room Temperature
SCE	Saturated Calomel Electrode
SEM	Scanning Electron Microscopy
S_{BET}	Specific Surface Area
SC_S	Supercapacitors
UNESCO	The United Nations Educational, Scientific And Cultural Organization
V	Volt
V_T	Total Pore Volume
V_{HK}/V_T	Microspore's Contribution To The Total Pore

WiSE	Water in salt electrolyte
XRD	X-ray diffraction
Ω	Ohm
$	US Dollar
k	Ionic Conductivity

The Aim of This Work

Considering the need for energy storage devices (ESDs) based on efficient, unexpensive, low environmental impact and safe materials, the main objective of the thesis was the investigation of high-performance aqueous SCs using activated carbons ACs based on low cost abundant natural resources such as Argan shells (agricultural waste) and Anthracite (natural coal) as electrodes materials. At first, low-cost conventional aqueous electrolytes such as KOH and H_2SO_4 were tested. Afterwards safe low cost and circumneutral ammonium acetate water-in-salt electrolyte was used in order to improve the performances of the SCs devices as well as its environmental friendliness.

Therefore, this thesis manuscript is structured in the following Chapters:

Chapter 1 provides an overview on energy crisis and the important role of ESDs. Supercapacitor types and electrochemical energy storage modes are discussed. Different kinds of electrode materials (based on carbon) including a literature review on biomass and coal derived ACs and their application in electrochemical double layer capacitors EDLCs using aqueous electrolytes were reported.

Chapter 2 presents a summarised overview of the used physicochemical and electrochemical characterization techniques.

In Chapter 3, porous carbons material with high specific surface area were synthesized by chemical activation using two different methods impregnation (IM) or physical mixing (PM) with two activating agent potassium hydroxide (KOH) or sodium hydroxide (NaOH) using the agricultural waste Argan shells as precursor. Textural-structural characterizations (such as SEM, FTIR spectroscopy, X-Ray diffraction, Raman spectroscopy and N_2 adsorption/desorption isotherm measurement) of the prepared ACs and the carbonized precursor were performed. The selected sample showed a honeycomb-like structure with large spherical cavities, high specific surface area reaching to 2251 m^2/g and micro-mesopore size distribution. The investigation of the electrochemical properties of this carbon material has shown that the porous carbon electrode exhibit interesting performances as revealed by high capacitive behavior using aqueous electrolytes. At 0,1 A g^{-1} the specific capacitance reached 250 F g^{-1} and 192 F g^{-1} using H_2SO_4 and KOH electrolytes, respectively. The assembled symmetric supercapacitor based on the as-prepared porous carbon as electrodes and H_2SO_4 as electrolyte showed a high energy density of 8.75 Wh kg^{-1} and power density of 3.1 kW kg^{-1} as well as very low resistance of 0.21Ω cm^2 and cycling stability with 94 % capacitance retention after 10,000 cycles at a current density of 1 A g^{-1}. Such results demonstrates that renewable agriculture waste (Argan shell) can be valorized as promising candidate for applications as supercapacitor electrodes.

In chapter 4, a physical mixing activation method using KOH or NaOH was presented to synthesize ACs from natural Anthracite. The textural-structural proprieties of the as prepared Anthracite-based activated carbon were characterized by SEM, X-Ray diffraction, Raman spectroscopy and N_2 adsorption and desorption isotherm. The selected sample features high surface area about 2935 m^2/g and appropriate micro-mesopores distribution. The electrochemical performance of the supercapacitors made from Anthracite-derived ACs was investigated. Symmetrical two-electrode supercapacitor cells with 1M H_2SO_4 and 6M KOH aqueous system as electrolyte were assembled that yield to interesting values of capacitance reached 50.3 F g^{-1} and 38 F g^{-1} (at the current density of 0.1 A g^{-1}) respectively. Interestingly, when H_2SO_4 electrolyte was used, supercapacitor cells demonstrated high energy density of 7 Wh k g^{-1} and power density of 1.7 kW kg^{-1} as well as excellent capacitance retention of about 99 % after 10,000 cycles. Hence, such promising electrochemical performances, indicates that abundant low-cost Anthracite is a promising AC candidate for supercapacitor application.

In chapter 5, low-cost concentrated aqueous solutions (molality range from 1 to 30 mol kg^{-1}) based on ammonium acetate were investigated as potential electrolytes. The physical-chemical studies such as pH, ionic conductivity, viscosity, conductivity temperature dependence measurement and molecular dynamic MD simulations have shown that the super-concentrated solution feature circumneutral pH (pH = 7–8), ionic conductivity comparable to or higher than common organic electrolytes, changes in the structure of the solutions due to strong interactions between ions and/or water molecules via the formation of hydrogen bonding which causes an increase in pH values and a decrease in ion mobility, ammonium and acetate are strongly hydrated while there is no destruction in the structure of water by the ionic field. and the mixture shifts from "ion in water" (conventional solutions) to "ionic-liquid-like" (concentrated solutions) behavior.

The electrochemical measurement revealed one of the most interesting aspects which that the water in salt based on 26.4 m exhibits an electrochemical stability window ESW of 2.22 V at aluminium Al foil, 2.9 V at glassy carbon GC, and an outstanding value of 3.4 V at titanium Ti grid. It also prevented the development of symmetric SCS with the high cell voltage predicted by the study using GC and metal grids. However, the ESW is related to the kind of electrodes used in the test where the Argan shells derived activated carbon ARG-AC based electrode was able to reach only 1.3 V affected by the high carbon surface area that favoured electrochemical decomposition of the electrolyte. Even though, ARG-AC electrode exhibited an exceptional specific capacitance of 300 Fg^{-1} in the super-concentrated electrolyte. The asymmetric supercapacitor with ARG-AC electrodes and 26.4 m ammonium acetate water in salt AmAc WiSE was able to function at 1.2 V from -10°C to 80 °C with outstanding specific capacitance and low resistance. The asymmetric cell provided noticeable specific energy at extreme temperatures, ranging from 5.9 Wh kg^{-1} at 10 °C to 15.6 Wh kg^{-1} at 80 °C, values that are competitive with those of commercial SC_S with organic electrolyte. Overall, this study suggests that AmAc WiSE deserves consideration as cheap, circumneutral and environmentally friendly alternative electrolytes for designing green energy storage systems.

Chapter 6 includes the conclusions.

CHAPTER 1: INTRODUCTION

1.1 Energy Context

The world's population is growing, and the quality of living is improving, resulting large and increasing demand for raw materials and energy. Energy demand has been covered by fossil energy sources ranging from coal to oil and natural gas from the industrial revolution and the transition to the industrial age until recent time. As can be seen in **Figure 1**, fossil fuels covered more than 70% of the primary energy demand, and this value can be rises to more than 80% if nuclear power is included. As results, emissions of enormous amounts of greenhouse gas GHG, which affect negatively our health, environment and trusted to be the primary cause of global warming and climate change.

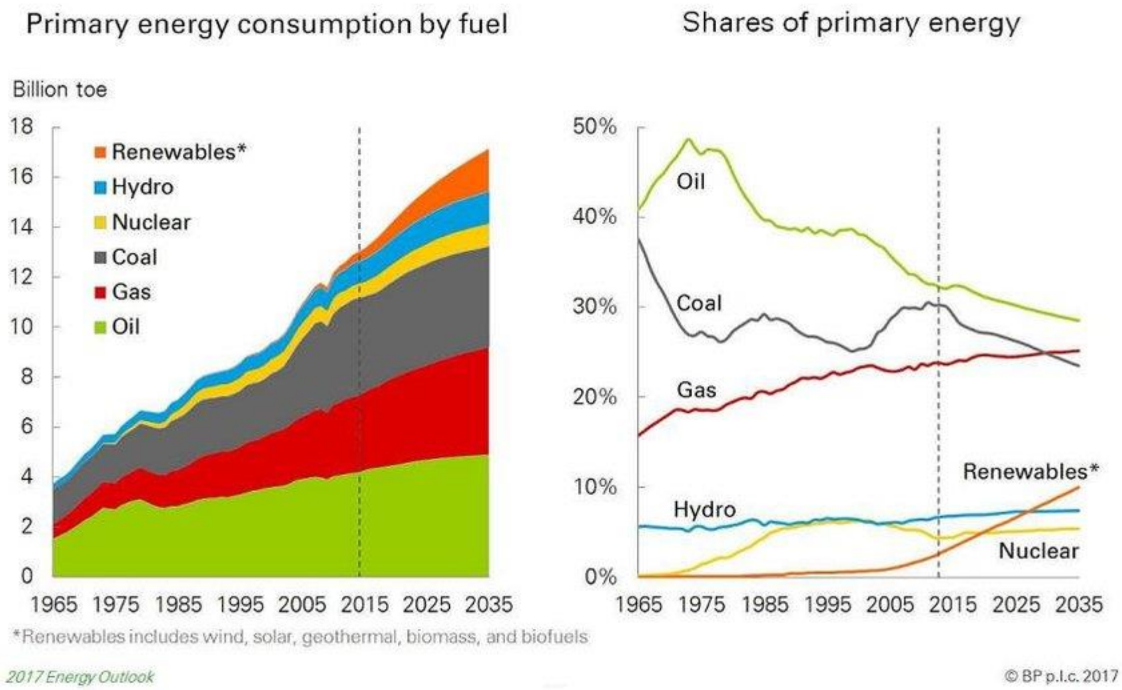

Figure 1. Trends in worldwide energy consumption from 1965 to 2035.

Thus, a rational energy transition to sustainable energy development have become the most urgent challenges the world is facing today [1]. Therefore, the global community is moving towards finding more sustainable ways dealing with production conversion and storage of renewable energies that could match the demand without causing more environmental burdens.

1.2 Renewable Energy

Renewable energy sources also known as alternative energy sources [2] can be used to produce energy repeatedly, from resources such as solar, wind , biomass , geothermal, ect. meet various needs with zero or reduced emissions of air pollutants and greenhouse gases [3]. Throughout the last few decades, there has been a huge increase in research on renewable energy sources such as solar energy and wind energy. Therefore, its adoption has been raising their proportion in energy supply, while due to their intermittency, relatively high cost, low conversion rate, and low energy output, they still accounted for a limited contribution [4].

To ensure the reliability and consistency of renewable energy sources output, a backup power supply system is required. Deployment of energy storage systems and devices can store and supply power at low output levels from renewable energies, as well as provide off-grid energy to poor and remote areas [5-7]. Such energy storage devices ESDs with high energy and power density will play a key role in the future with respect to the integration of renewable energy sources into existing power system as well as others several applications related to electric mobility and others.

1.3 Energy Storage Devices

To store energy supplied by renewable devices such as photovoltaics, energy storage / conversion systems based on batteries, fuel cells, and electrochemical supercapacitors SCs have been developed [8-13]. Lithium-ion batteries have been widely used as an efficient storage technology among them. However, the lithium-ion battery has some disadvantages associated mainly with safety power density, and cost [10, 14-17]. While, SCs have attracted attention in recent years mainly due to their high power density, long life cycle, and ability to fill the power/energy gap between batteries/fuel cells (have a high energy density) and conventional capacitors (which have a high power density). The **Figure 2** shown in compares ESDs in terms of power density and energy density as a Ragone plot.

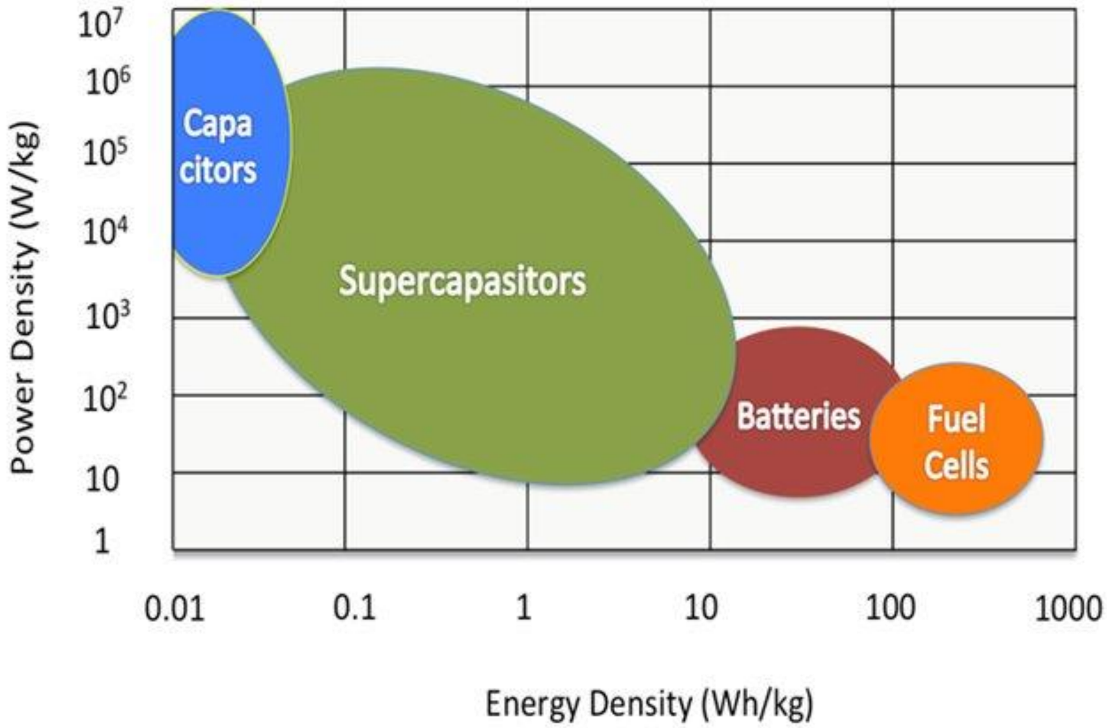

Figure 2. Ragone plot of different energy storage devices.

1.4 Electrochemical Energy Storage Modes

In general, at an energy storage device, the energy storage processes take place at the electrodes in two modes either faradaic or non-faradic.

Faradic processes are redox reactions through chemical transformations that are limited by the kinetics and the activation energies of the reactions as well as mass transport (transport of reagents), that not allow high power density. In addition, electrode materials may undergo transformations during cycling: modification of the chemical composition, of the oxidation state, modification of the volume, appearance of reaction products (gas, etc.). Finally, the electrochemical reactions involved can have a coulombic efficiency lower than 100%. For these reasons, despite the high charge storage capacity, faradic materials might exhibit reduced lifetime if compared to non-faradic electrodes. Indeed, the non-Faradic process occurs through an electrostatic storage of charges on the electrode surfaces through a phenomenon at the root of energy storage in dielectric capacitors. It is a rapid surface phenomenon completely reversible and does not yield to any chemical or structural changes in the involved material. Hence, the process reversibility may yield to a high power density and a theoretically unlimited lifetime.

1.5 Supercapacitors

Supercapacitors (SC_S), also known as ultracapacitors, are a type of electrical energy storage that are ideal for situations requiring rapid energy storage while still delivering high power[18]. In 1987, they were introduced to the market as farad-sized SC_S for computer memory backup power[19]. SCs are classified into three categories depending on their charge storage mechanism [20, 21]; electrostatic double-layer capacitors EDLC, pseudocapacitors PC, and hybrid supercapacitors HSC (**Figure 3)**.

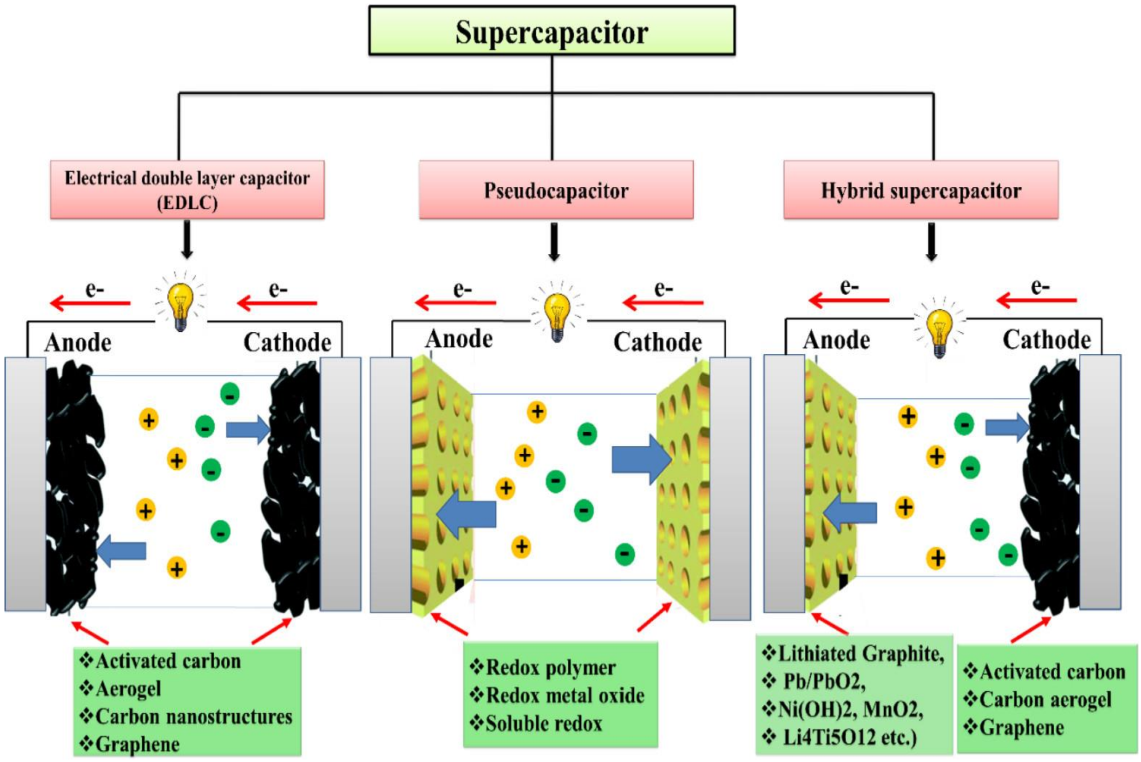

Figure 3. Classifications of SC_S showing the types of electrode materials and mechanism used [22].

1.5.1 Electrostatic Double-Layer Capacitor EDLC

The EDLCs are symmetrical SC_S constituted of two electrodes based on carbon. The storage mechanism consists on the adsorption of ions at the active material / electrolyte interface via the formation of an electrochemical double layer EDL (capacitive processes) [23, 24]. The EDL has been described by different models including that of Helmholtz (second half of the 19th century), which simply considers the formation at the electrode / electrolyte interface of a layer of ions, for example of anions if the electrode is positively charged (**Figure 4a**)[25]. Guy and Chapman's model (early 20th century) considers the formation of a diffuse layer associated with thermal agitation in which the potential decreases exponentially (**Figure 4b**)[26, 27] . Finally, Stern's model (1924) combines these two approaches by forming a compact layer in the vicinity close to the electrode and then a diffuse layer (**Figure 4c**)[28].

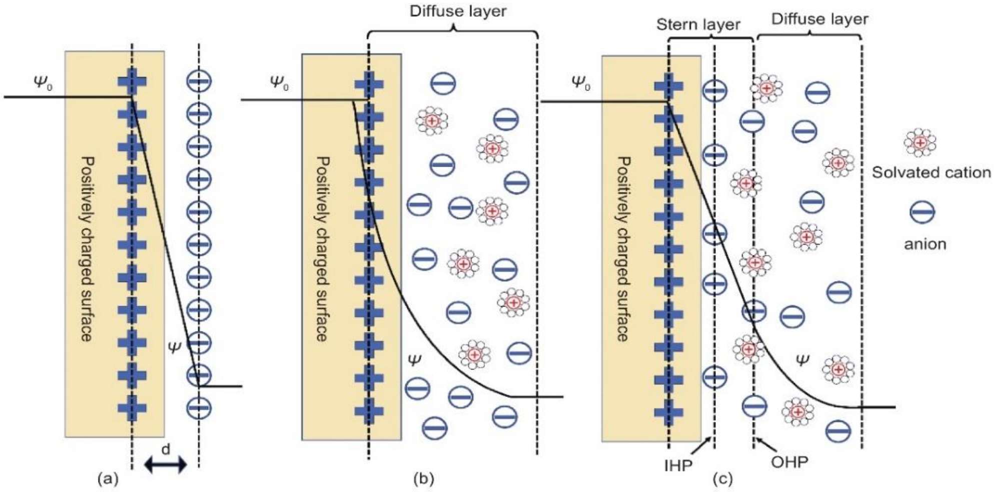

Figure 4. Different EDL models: (a) Helmholtz[25], (b) Gouy-Chapman[27] and (c) Stern[28]. (d) presents the electric double layer distance in Helmholtz model. Ψ_0 and Ψ are potentials at the electrode surface and electrode/electrolyte interface, respectively.[29]

The capacitance (double layer capacitance) depends on the quantity of ions adsorbed on the surface of the electrode. Thus, the structure and texture of carbon electrode material, especially its, specific surface area and pore size distribution in addition of selecting appropriate electrolyte will greatly affect its performance in terms of capacitance and energy density [21]. While, EDLCs sustain high power density and excellent cyclic stability due to the storage capacity associated with characteristics with respect to charges diffusion and adsorption [23, 30].

1.5.2 Pseudocapacitors

PC electrodes are based mainly on electro-active materials such as metal oxides (e.g. MnO_2, RuO_2) [31, 32] and conducting polymers (e.g. polypyrrole, polyailine) [33, 34]. In this systems the energy storage mechanism is far more complicated than that of an EDLC, occurring via charge storage through reversible redox reactions as well as electrochemical adsorption/desorption [35], i.e., intercalation/de-intercalation and doping/de-doping of ions at the electrode/electrolyte interface as Faradaic charge transfer process [39]. A comparison of charge storage in a EDLC and a PC shown in **Figure 5**.

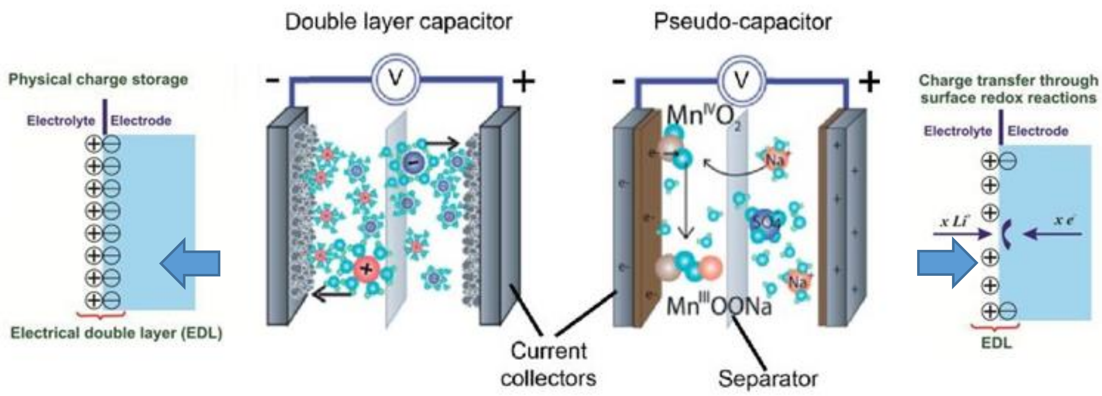

Figure 5. Comparison between double layer capacitor, pseudo-capacitor. Adapted from Ref [36]

Despite the capacitance values and energy density can be increased significantly by the involved Faradaic processes, PC deliver lower power density than EDCLs due to the fact that Faradaic processes are often slower than non-Faradaic processes [37]. Also, the storage mechanism i.e. transition redox reactions on metal oxides and conducting polymers decays the cycle life of PCs [38-40].

1.5.3 Hybrid Capacitors

Hybrid capacitors, which are an association of EDLC and PC [41, 42]. Those kind of SCs have been designed so as to obtain a capacitor with synergistic properties, where the PC electrode makes it possible to obtain a high energy density, and the capacitive electrode allows high power density.

Although PCs and hybrid capacitors deliver superior specific capacitance than that of EDLCs, their potential applications are limited by inferior cycle performance, and high cost [32].

However, in the last few decades, researchers have made great efforts to develop high specific capacitance and low cost EDLCs, involving advanced active materials for electrodes. based on carbon materials owing to its various structural forms [43].

1.6 Carbon Based Materials For EDLC Electrodes

A variety of carbon materials with different structure have been used to store charge in EDLC electrodes, including activated carbon AC, carbon nanotubes CNTs and graphene, regarding their large surface area, high porosity, electronic conductivity and chemical stability as well as wide operating temperature range [44], as highlighted in **Table 1**.

Table 1. Characteristics of carbon materials used as EDLCs electrodes material.

Adapted from Ref [45]

Material	Carbon nanotubes	Graphene	Activated carbon
	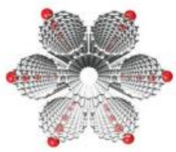	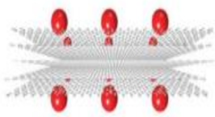	
Conductivity	High	High	Structure dependent
Volumetric capacitance	Low	Moderate	High
Cost	High	Moderate	Low

A large specific surface area generally results a high specific capacitance, while, pore sizes and their distribution might significantly affect the EDLC kinetics. Classification proposed generally, the porosity is classified following IUPAC (International Union of Pure and Applied Chemistry [46] :

- macropores with a diameter greater than 50 nm
- mesopores with a diameter between 2 and 50 nm
- micropores with a diameter of less than 2 nm.

In addition to subcategories of micropores such as supermicropores with diameters between 0.7 nm and 2 nm, and ultramicropores less than 0.7 nm [46] .

1.6.1 Activated Carbon

AC is a promising material for SC_S electrodes because of related low cost, high conductivity, and good thermal stability and corrosion resistance. Several synthesis routes are reported for the preparation AC_S with high specific surface area and appropriate pores size distribution suitable for EDLC electrodes [47]. Note that such characteristics are, also, influenced by the precursor, the synthesis and activation process [48, 49]. AC_S production process (carbonization and activation) is easy in addition; unexpansive natural abundant resources can be used as precursors.

The activation consists of oxidation following physical or chemical processes that allow creation of a random network of pores (macropores, mesopores or micropores).

Usually, Physical activation is carried out through carbonization of materials (biomass, hard coal, etc.) at temperatures of the order of 900 °C to 1100 °C under an oxidizing atmosphere. The porosity is developed by structural rearrangement and oxidation of carbon resulting in pores creation an opening and/or enlargement.

Chemical activation proceeds in the presence of a chemical agent (phosphoric acid, zinc chloride, potash, etc.) through dehydration, carbonization and structural reorganization of the precursor, permitting development of micropores and mesopores [50]. Note that controlling the activation parameters was reported to obtain specific surface area of almost 3,000 $m^2.g^{-1}$ [44] and obtain an interconnected pores network of different size (**Figure 6**).

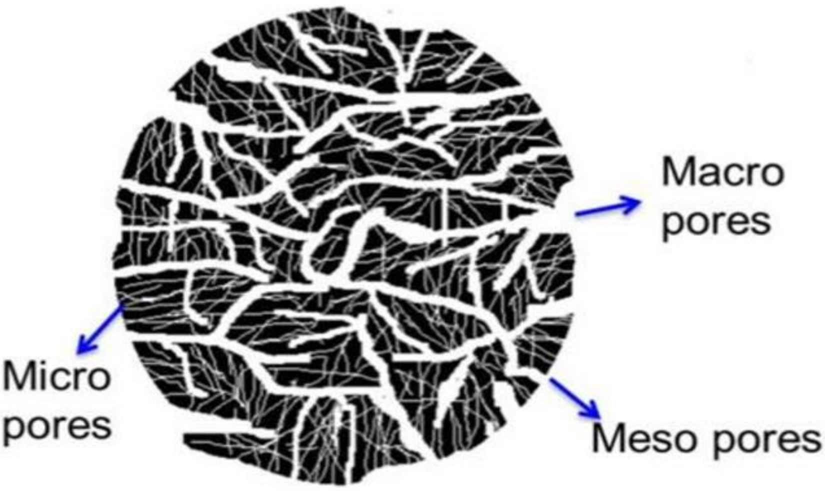

Figure 6. Scheme illustrating the porosity developed in a grain of AC

1.6.1.1 Bio-waste Derived AC Based EDLC Using Aqouese Electrolytes

Biomass, one of the most promising renewable energy sources on the planet; it is natural, abundant, low cost, and environmentally friendly. In term of economic and sustainable production of AC, biomass is getting more attention as precursors. The fabrication process of biomas-derived AC takes place into two stages [51]. The first step is carbonization, throughout which the carbon-rich organic precursor undergoes heat treatment to remove the non-carbon elements. Consecutively, in order to increase surface area, the carbon material is physically or chemically activated using oxidizing gases or oxidizing agents (e.g. KOH, NaOH, $ZnCl_2$, H_3PO_4), respectively [52-54]. Chemical activation uses dehydrating agents to inhibit the formation of tar and increase the yield of carbon, whereas physical activation gasifies the char (the interstices) in steam to enhance the pores.[55]. Chemical activation is advantageous since it requires only one step and lower pyrolysis temperatures, produces a higher carbon yield with a large surface area, and microporosity could be developed and controlled [56]. Using low-cost biomass such as bio-waste (agriculture by-products or food industry waste) derived AC_S for SC electrode material applications not only solves the waste management problem [57, 58], but also generates revenue for supply chains, thereby shifting the economy toward a circular economy [59]. In recent years, there has been a surge of interest in producing AC from biomass for durable development [59-64]. So many sources of bio-waste, including animal, mineral, plant, and vegetable waste, have been reported in the literature as base materials for the production of AC with the aim to be used as an electrode material in SC_S [59, 65-70]. For instance, Yang et al. Developed porous carbon with SSA of 1471.4 m^2/g from corncob, that delivers high energy density of 20.15 Wh/kg in 6 M KOH electrolyte [71]. Following the same procedures, Mitravinda et al. investigated corn silk derived AC which showed a promising energy density of ~32.28 Wh/kg and a power density of 870.68 W/kg[72]. This is made possible by the exceptional mesoporous fiber-like morphology, which promotes rapid electrolyte diffusion into and out of the pores during charging and discharging. In another study, Yin et al. used coconut fibers to develop 3-dimensional hierarchical porous carbon [73], the high SSA of 2898 m2/g and the pore volume of 1.59 cm3/g allow the assembled device using in 6 M KOH as electrolyte to reach a high energy density of 53 Wh/kg and an impressive power density of 8200 W/kg. Also, Qin et al. synthesized Pine nut shell derived AC using physical activation[73]. The obtained interconnected porous structure with different pore size distribution (micro-, meso-, and macropores) assisted the prepared electrode with this material to demonstrate in 6 M KOH electrolyte a high cyclic stability of 98 % after 10,000 cycles [73]. **Table 2** reports electrochemical performance of more investigated Bio-Waste derived carbons for SC_S using aqueous electrolyte.

Table 2. Electrochemical performance of Bio-Waste derived carbons for SC_S using diferent aqueous electrolytes [59].

Bio-waste Resource	SSA (m^2/g)	Electrolyte	Specific Capacitance (F/g)	Energy Density (Wh/kg)	Power Density (kW/kg)	Cyclic Stability	Ref
Corncob	1471	6 M KOH	293 (1A/g)	20.15	0.5	99.9 (4000)	[71]
Corn Husk	1370	6 M KOH	127 (1A/g)	4.4	0.248	90 (5000)	[74]
Rice Straw	1007	1 M H_2SO_4	332	7.8	0.15	99 (5000)	[75]
Rice Straw	2786	6 M KOH	317 (1A/g)	18.4	0.45	99.4 (5000)	[76]
Rice Husks	3831	6 M KOH	350 (0.1A/g)	6.9	122.6	99 (10,000)	[77]
Rice Straw	3333	6 M KOH	400 (0.1A/g)	14	0.5	80 (5000)	[78]
Orange Peel	2521	6 M KOH	407	–	–	100 (5000)	[78]
Orange Peel	350	2 M KOH	268	32	0.7	100 (8000)	[79]
Allium Cepa	2962	3 M KOH	189.4 (0.1A/g)	22.1	0.039	90 (4500)	[80]
Coconut Fibers	2898	6 M KOH	142 (10A/g)	53	8.2	76 (10,000)	[73]
Coconut Coir	2900	6 M KOH	247.1 (0.2A/g)	33.6	4.2	100 (10,000)	[81]
Cucumber	389	6 M KOH	143 (0.5A/g)	4.38	0.45	97 (1000)	[82]
Jackfruit Shell	511.4	0.5 M KOH	292 (1A/g)	40	1.48	94 (10,000)	[83]
Durian Shell	617.87	0.5 M KOH	591 (1A/g)	41.47	0.73	96 (10,000)	[83]
Potatoes	–	2 M KOH	236 (0.5A/g)	6.8	0.31	96 (10,000)	[84]
Mushroom	935.8	1 M Na_2SO_4	253 (0.5A/g)	35.9	0.36	90 (10,000)	[85]
Aloe Peels	1286	6 M KOH	264 (0.5A/g)	–	–	91 (5000)	[86]
Pitaya Peel	1872	6 M KOH	255 (1A/g)	–	–	96.4 (5000)	[87]
Peanut Shell	1623	0.1 M H_2SO_4	291	–	–	–	[88]
Pine Nut Shell	956	6 M KOH	128 (0.5A/g)	–	–	98 (10,000)	[89]
Polyalthia	644	1 M Na_2SO_4	365 (1A/g)	27.5	0.499	92 (5000)	[90]
Soyabean Seeds	–	6 M KOH	281.4 (0.5A/g)	23.4	—	100 (10,000)	[91]
Acai seeds	3120	1 M KOH	346 (1 mA/cm^2)	48	–	88.3 (5000)	[92]
Coffee Grounds	763	1 M H_2SO_4	–	15	0.075	88 (10,000)	[93]
Coffee Grounds	3549	6 M KOH	440 (0.5A/g)	101	0.9	92 (10,000)	[94]
Coffee Seeds	1824	6 M KOH	148 (0.5A/g)	12.8	6.64	97 (10,000)	[94]
Bean Sprout	1114	6 M KOH	421 (1A/g)	5.44	0.3	96.2 (10,000)	[95]
Olive Seed	1700	1 M H_2SO_4/1M Na_2SO_4	224 (0.25A/g)	3–5	20–30	91 (12,500)	[96]

1.6.1.2 Coal Derived AC Based EDLC Using Aqueous Electrolytes

Coal is a low-cost carbon-rich material existing with huge natural reserve (World coal reserves in 2020 stood at 1074 billion tonnes) [97]. This make it as precursor for other carbon-derived materials. Also, developing coal's non-combustion technology could open up a large market and increase its economic value [98]. There are five types of coal: peat, lignite, subbituminous, bituminous, anthracite, and anthracite. Peat is a soft, crumbly, dark brown substance formed by the decomposition of dead and partially decaying organic matter over many generations. Peat contains the least amount of carbon (less than 60%). Lignite, also known as brown coal, a coal with a brown and carbon content varies between 65 and 70%. Subbituminous coal, also known as black lignite, is a dark brown or grey-black coal. The carbon content of subbituminous coal ranges between 70 and 76 %. With a carbon content ranging from 76 to 86 percent, bituminous coal is the second highest quality of coal. Bituminous coal is the second highest grade coal, with a carbon content of 76–86%. Anthracite is the highest grade coal it’s dark black coal, has a low moisture content and a carbon content of nearly 95% [99]. **Figure 7** describes a representative structure of different coals types, as well as their degree of coalification.

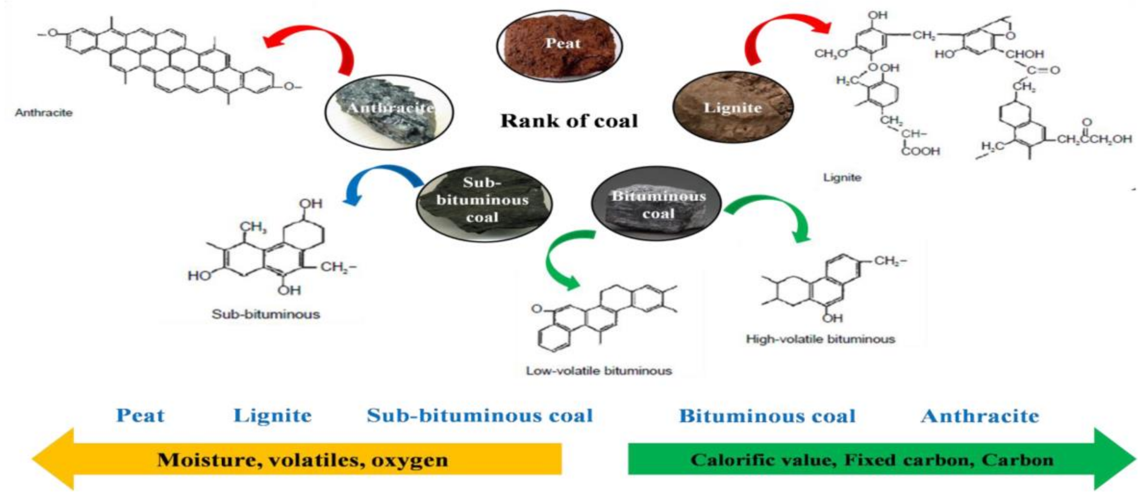

Figure 7. Schematic representation of different rank coals and their structural moiety. Adapted from Ref [22]

However, coal in general is attracting a lot of interest as a row material for preparing AC with a large specific surface area. Similarly to the AC synthesis from biomass, coal derived activated could be synthetized by activation physical activation using using air, O_2, steam, CO_2, etc. or by chemical activation using KOH, $ZnCl_2$, NaOH, H_3PO_4, etc. Using such AC derived from low cost abundant natural resources could be greatly beneficial for SC_S technology. In recent years, many researches have been investigated different coal type-based AC and its performances as SC electrodes material. Zhao et al. [100] used KOH chemical activation to produce AC from hypercoal with a high surface area of 2540 $m^2\,g^{-1}$ and obtained a maximum capacitance of 46.0 F g^{-1} for high-performance EDLC. Shi et al [101] assembled a high performance SC of specific capacitance of 280 F g^{-1} and energy density of 38.9 Wh kg^{-1} at 0.5 A g^{-1} using high surface area porous AC synthesized from anthracite. Zhu et al.[102] prepared high performance coal derived AC_S via a facile KOH activation, the optimized sample higher surface area of 2457 $m^2\,g^{-1}$ and larger total pore volume of 1.448 $cm^3\,g^{-1}$ the characteristics that allowed the material to displayed a high specific capacitance of 384 F g^{-1} at a scan rate of 5 mV s^{-1} in 6 M KOH. **Table 3** summarize different some coal derived AC that have been successfully used as SC_S electrodes materials that demonstrated high specific capacitance as well as high power density in aqueus electrolytes.

Table 3. Electrochemical performance of Coal derived carbons for SCs using different aqueous electrolytes, and energy and power performance of the SCs assembled with these materials

materials	electrolyte	surface area (m^2 g^{-1})	specific capacitance (Fg^{-1})	energy density (Wh kg^{-1})	power density (WK g^{-1})	ref
coal	6 M KOH	2457	384	4.20	100	[102]
coal	6 M KOH	1773	141	35	6250	[103]
lignite	6 M KOH	1945.66	230	31.94	574.92	[104]
coal	1 M H_2SO_4	3150	317	28.17	199.94	[105]
Zhundong coal	6 M KOH	132.5	205	28.47	256.25	[106]
coal	6 M KOH	948.55	227	31.52	540.34	[107]
coal	6 M KOH	2308	308	42.77	531.03	[108]
low-rank coal	6 M KOH	1872	211	29.30	586.11	[109]
coal	6 M KOH	2168	254	7.64	1000	[110]
coal	6 M KOH	1303	260	7.20	500	[111]
coal-tar pitch	6 M KOH	1294.60	292	8.16	6740	[112]
coal	0.1 M KOH	2092	128	17.77	266.67	[113]
bituminous coal	3 M KOH	1950	370	7.60	10000	[114]
coal-tar pitch	6 M KOH	1786	267	12	1318	[115]
coal-tar pitch	6 M KOH	3114.20	356.80	10.25	496	[116]
coal	6 M KOH	1436	176	9.70	2000	[117]
coal-tar pitch	1 M Na_2SO_4	1525	350	22.30	876	[118]
coal-tar pitch	6 M KOH	1046	242	5.56	9907	[119]
lignite	6 M KOH	1852.43	160	22.22	470.58	[120]
Powder River Basin coal	6 M KOH	1678.80	299.40	41.58	598.75	[121]
coal-tar pitch	6 M KOH	1394.60	317	6.81	25000	[122]
coal-tar pitch	6 M KOH	2028	380	9.61	238.59	[123]
coal-tar pitch	1 M Na_2SO_4	1605	377	31.13	193.60	[124]
coal	6 M KOH	2164	287	4.50	12500	[125]
coal tar	1 M H_2SO_4	1067	39	561.16	2730	[125]
coal	2 M KOH	1695.10	144	18.67	101.35	[126]

1.6.2 Carbon Nanotube

CNTs have been reported to have special features of interest for EDLC electrode. The development of high-power ECs has been motivated by their high electrical conductivity, good mechanical and thermal stability, and highly accessible network of pores[44]. CNTs can be categorized into two categories, single-walled nanotubes (SWCNTs) and multi-walled nanotubes (MWCNTs), based on differences in geometric structure and electrical and mechanical properties [44, 127]. CNTs are mainly synthesized by Arc-discharge, laser ablation, and Chemical Vapor Deposition (CVD) methods, which are an experimentally complex and require high capital equipment in addition; none of the three synthesis methods has yielded bulk high quality materials [47].

1.6.3 Graphene

Graphene, a typical two-dimensional single layer of carbon atoms, with unique morphology that is represented by a single layered 2-D lattice structure of carbon atoms, with accessible surface area different from that of any other carbon material employed in EDLCs [44]. Graphene is mainly synthesized by Chemical Vapor Deposition, Chemical or Plasma Exfoliation from natural Graphite, and Mechanical cleavage from natural Graphite, but also none of the three synthesis methods has yielded bulk high quality materials.

In summary, although the potential proprieties the industrial application of some reported carbon materials such as graphene, CNTs -based materials is still not feasible because of the small mass production, and costly complicated synthesis process. In other hand, due to its large mass production and relatively facile synthesis process, AC availability attracted many others applications including air purification, water treatment, energy storage, etc. Therefore, its demand is growing estimated by the global AC market is expected to reach US dollar($) 8.9 billion, at 2026, [128]. Indeed, from a business standpoint, developing economically viable AC using low-cost abundant natural resources-based precursors is critical such as renewable biomass or coal waste selected in the present work.

1.7 Electrolyte for EDLC

Several criteria are decisive for the choice of an electrolyte but the two main criteria are the electrochemical stability window and the ionic conductivity.

The operating voltage of a supercapacitor essentially depends on the electrochemical stability window of the electrolyte used [18, 129]. The conductivity of the electrolyte largely depends on the equivalent series resistance of the supercapacitor [130]. The fallowing relation defines the ionic conductivity κ:

$$\kappa = F \, \Sigma_i \, z_i \, C_i \, \mu_i \qquad (1)$$

while

- k is the ionic conductivity ($S.cm^{-1}$)
- F is the Faraday constant ($C.mol^{-1}$)
- z_i is the charge of ion i
- C_i is the concentration of ions i ($mol.cm^{-3}$)
- μ_i is the mobility of ions i ($cm^2.V^{-1}.s^{-1}$)

The used temperature range of the electrolyte used is also a criterion to be taken into account, depending on the intended application; the temperature range of the electrolyte use also influences its conductivity. Furthermore cost and environmental impact should also be taken into consideration when choosing the electrolyte [18].

The electrolytes can be classified into three categories: organic, ionic liquids and aqueous. Each has its own set of advantages and disadvantages, which are reported in **Table 4**.

Table 4. Comparison of common electrolytes used in supercapacitor [18, 131-133].

Electrolyte	**Examples**	**Potential (V)**	**Conductivity**	**Other characteristics**
Aqueous	H2SO$_4$, KOH, Na_2SO_4, NH_4Cl	~1.2	High	Cheap, safe, low environmental impact
Organic	Acetonitrile, propylene carbonate	~3–3.5	Moderate	Flammable, toxic, require low water content (<5ppm)
Ionic liquid	Imidazolium, pyrrolidinium	~4.5	Low	Low flammability, costly

1.7.1 Aqueous Electrolytes

Aqueous electrolytes were used in supercapacitor due to related main advantage such as high conductivity reaching 700 $mS.cm^{-1}$ for example using sulfuric acid, this high conductivity makes it possible to obtain high capacitances, and low resistances. In addition, their price and environmental impact remain low; unlike organic electrolytes with no risk of explosion in case of overheating, and their temperature range of use that is limited by that of water. While, their main disadvantage is the narrow electrochemical stability window due to the decomposition of water which occurs at a thermodynamic potential of 1.23 V.

1.7.2 Organic Electrolytes

The most widely used organic solvents in SC_S are propylene carbonate and acetonitrile. Organic electrolytes made it possible to increase the voltage of the SC_S up to 2.7 V, due to their large electrochemical stability window. The ionic conductivity of organic electrolytes is lower than that of aqueous electrolytes, also the radius of the solvated ions in organic electrolytes are larger than those of aqueous electrolytes. These two properties explain that the capacitance obtained in organic electrolytes is lower than that obtained in aqueous electrolytes [134]. In addition to the high price of organic electrolytes, they are toxic and may arise safety issues (due to their very low flash point), inconvenient to assemble in air and pose environmental problem (organic solvents which are difficult to recycle leake by evaporation during the production).

1.7.3 Ionic Liquids

Ionic liquids are obtained with salts having a melting point below 100 ° C and generally used as liquid electrolytes at room temperature. Note that no solvent is used and only the ions of the salt. The first ionic liquid was described in 1914 by Walden: ethylammonium nitrate (EAN)with a melting point of 12 °C, but research on ionic liquids really started in the 1970s [135, 136]. Among the most investigated ionic liquids we find: 1-ethyl-3-methylimidazolium bis(trifluoromethylsulfonyl)imide (EMITFSI), N-methyl-N-propylpiperidinium bis(trifluoromethanesulfonyl)imide [PP_{13}][TFSI], 1-butyl-1-methylpyrrolidinium bis(trifluoromethanesulfonyl)imide (PYR_{14}TFSI) and others [137, 138]. Because their high electrochemical stability, non-flammability, and high thermal stability, they are getting more attention as electrolyte for SC_S [139] although their relatively low ionic conductivity and their very high cost.

Overall, even their small electrochemical stability window, aqueous electrolytes have more potential prospects in SCs application because of their very high ionic conductivity that is much higher than that of other electrolytes, low cost, safe, and low environmental impact.

CHAPTER 2: CHARACTERISATION TECHNIQUES

In this chapter, the overall characterisation techniques used throughout this thesis are reported with a brief description including:

- Physical-chemical characterizations techniques used to investigate the textural and structural proprieties of the prepared carbon materials and the physical-chemical proprieties of ammonium acetate water in salt electrolyte, such as scanning electron microscopy (SEM), X-ray diffraction (XRD), raman spectroscopy (RS) , N_2 adsorption isotherms, attenuated total reflection-Fourier transform infrared spectroscopy (ATR-FTIR) and molecular dynamic (MD) simulation. (Section 2.1)
- Electrochemical characterization techniques used to investigate the electrochemical performances of the prepared ACs-based electrodes and SC_S, such as cyclic voltammetry (CV), galvanostatic charge-discharge (GCD) and electrochemical impedance spectroscopy (EIS). (Section 2.2)

2.1 Physical-chemical Characterizations

2.1.1 Scanning Electron Microscopy

The SEM uses an incident beam of sufficiently accelerated electrons, also called primary electrons, which interact with the sample. This results in internal modifications of the target (thermal agitation, absorption of electrons, creation of electron-hole pairs, etc.) and various emissions of electrons (secondary, backscattered, transmitted and Auger) and photons over a wide spectrum of wavelength (X-rays, ultraviolet, visible, infra-red,…). The signals emitted are used in imaging or spectroscopy and provide information in particular on the morphology and topography of the observed sample. **Figure 8** shows a schematic of a scanning reflection microscope.

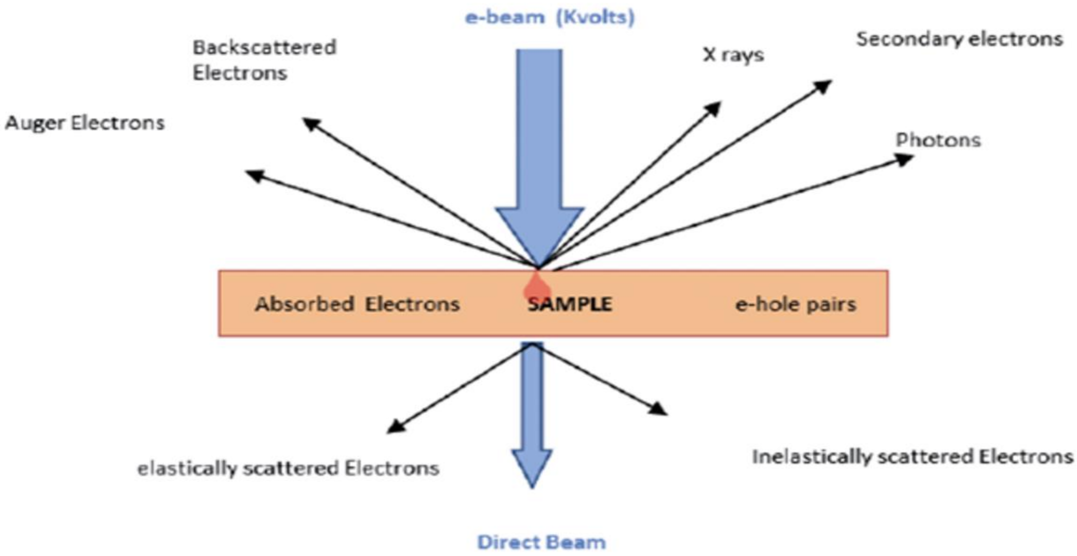

Figure 8. Diagram of the different types of interaction that can take place between an electron beam from the SEM and matter.

In this work the as-prepared samples were observed by scanning electron microscopy (SEM, SH–4000M) at an acceleration voltage of 15 Kv.

2.1.2 X-ray Diffraction

The crystal structure of the samples was analyzed by X-ray diffraction (XRD). This non-destructive structural analysis technique is based on the diffraction of a monochromatic beam of X-rays by the reticular planes in an ordered solid. Thus, it makes it possible to identify and quantify the crystalline phases, to determine the crystallographic structure of these phases, and to estimate the size of the crystallites. The material to be analyzed is thus exposed to X-rays of known wavelength and the rays diffracted by the material are analyzed. The crystalline nature of the compounds in the sample is revealed by the analysis of diffractions along particular directions using Bragg's law:

$$2d_{hkl}.\ \sin\theta = n.\lambda \qquad (2)$$

Where n is the order of the reflection, λ is the wavelength of the incident X-ray, dhkl is the distance between two reticular planes defined by the numbers h, k and l and θ is the Bragg angle (half angle diffraction). **Figure 9** shows the diffraction of X-rays along the reticular planes.

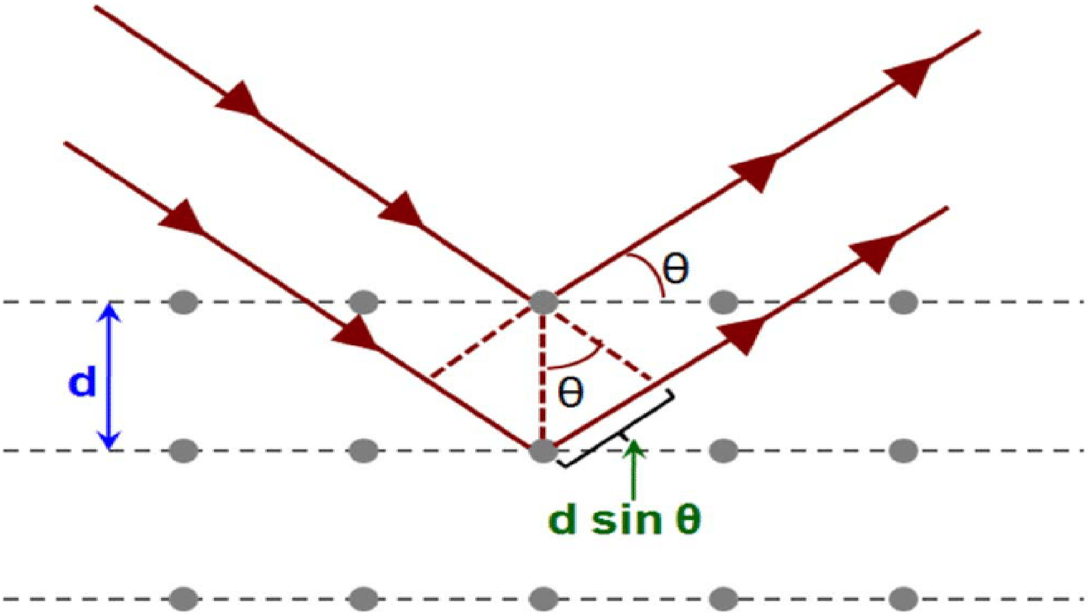

Figure 9. Diagram of X-ray diffraction along the reticular planes.

In powder diffraction, the wavelength is kept constant while the Bragg angle varies. The angular scan restores a diffractogram showing diffraction peaks at the values of 2θ corresponding to the hkl planes present in the sample. By comparison with the diffractograms of diffractions of reference materials listed in databases such as that of the International Center for Diffraction Data (ICDD), it is then possible to identify the phases present in the sample.

In this study, XRD analyses were conducted on two Phillips X'Pert-PRO diffractometers (PW3064/PW3830) using copper Kα radiation (λ = 0.154 nm) at a voltage of 40/45 kV and a current of 30/40 mA. The general acquisition conditions correspond to an angular range from 10 to 90°, with a step of 0.017° for an acquisition time of 1.81 seconds per step.

2.1.3 Raman Spectroscopy

Raman spectroscopy, very complementary to ray diffraction, is based on the inelastic process of the interaction of light with matter. By illuminating a sample with monochromatic radiation (laser beam), almost all of the photons constituting the light beam are re-emitted without interaction with matter. However, a small quantity of these photons interacts with matter and is scattered in all directions of space. In this fraction of light energy particles, the majority of photons are emitted at the same frequency as the incident radiation and constitute Rayleigh scattering. For only a tiny part of these scattered photons, a change in frequency resulting from an exchange of energy between the photons and the material is observed, which constitutes Raman scattering. Raman scattering is very weak compared to Raylight scattering and fluorescence scattering. It proved to be difficult to use until the development of powerful laser sources and highly selective holographic filters to suppress the strong Rayleigh scattering signal **(Figure 10)**

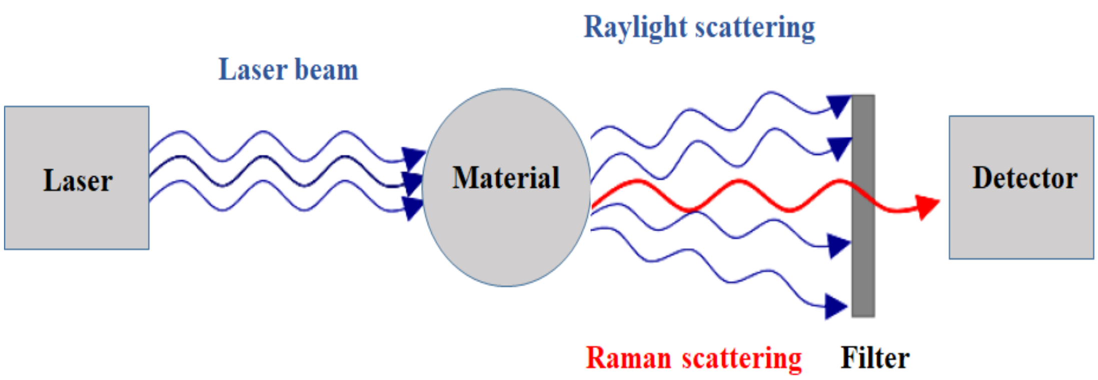

Figure 10. Process of light scattering by matter.

Raman spectroscopy is frequently applied for the characterization of carbonaceous materials, from graphite to amorphous carbonaceous materials. It is considered a powerful tool for analyzing the degrees of graphitization of carbonaceous materials.

2.1.4 N_2 Adsorption Isotherm

In this study, the textural characteristics of the prepared carbon were studied by measuring N_2 adsorption isotherms at 77 K using Micromeritics ASAP 2020 apparatus. The measurement of nitrogen adsorption and desorption isotherms allows the determination of the specific surface and other parameters related to the porous texture of a material. It is based on the physical adsorption of nitrogen at its normal liquefaction temperature (77K), in the pores of the material. The quantity of N_2 adsorbed depends on three parameters:

- the extent of the solid/gas interface,
- the gas pressure,
- the temperature.

Briefly, a known mass of the material is brought into equilibrium with a nitrogen pressure at 77K, then one proceeds by progressively increasing the relative equilibrium pressure (ratio of the pressure p to the saturated vapor pressure of the nitrogen P_0) until the saturated vapor pressure of the dinitrogen P0, there is first adsorption on the surface of the material then capillary condensation in its pores in increasing order of their size. The measure of the amount adsorbed per gram of adsorbent as a function of the P/P0 ratio at constant temperature gives the adsorption isotherm. The desorption isotherm is obtained during the reverse phenomenon, by decreasing the relative equilibrium pressure, where desorption takes place in the pores in decreasing order of their size. **Figure 11** presents the IUPAC classification of adsorption/desorption isotherms involving physical adsorption [140, 141], Moreover, there are essentially six types of isotherms, each type is observed in practice, but by far, the most common are types I, II and IV. Type I is the characteristic example of a microporous material, while type II is given by a nonporous or merely macroporous material and type IV is an example of a predominantly mesoporous material [141].

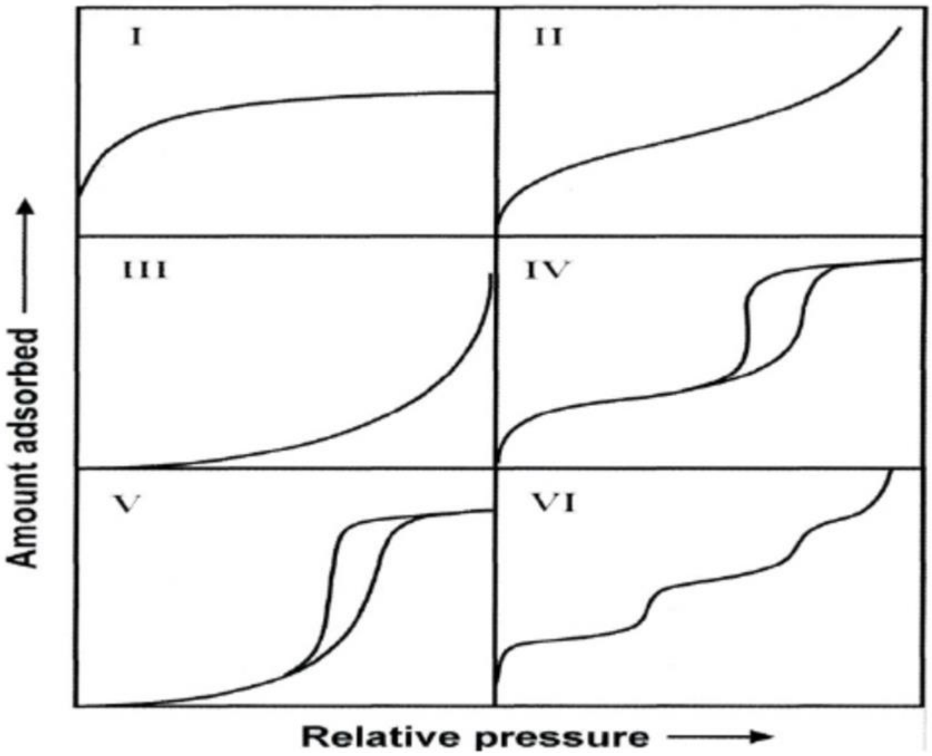

Figure 11. IUPAC classification of physical absorption isotherms

Physisorption experiment involves physical adsorption of a specific gas over the material's surface (including filling pores and cavities) and determining the total surface area, pore size distribution and pore volume, pore size distribution and pore volume. Many principles that provide mathematical models of the adsorption to derive the necessary information from the physisorption experiment, such as the Langmuir theory[142]. However, the most helpful model is the Brunauer-Emmett-Teller theory (BET) [140, 141]. The BET model is an extension of the principle of monolayer molecular adsorption to multilayer adsorption where many molecules can adsorb on top of each other at each adsorption site. Assuming that the gas molecules will adsorb to the solid forming infinite layers, these layers do not interact with each other [140]. BET theory permits the measurement of specific surface area (S_{BET}) of the sample. The calculations of pore size distribution were performed by simulating experimental data of adsorption isotherms by Density Functional Theory (DFT) [8]. This method is based on calculations of the densities of N_2 molecules when approaching the AC surface, calculated according to different parameters of the fluid/solid system (adsorbate/adsorbent) such as pressure, temperature, geometry of pores of the adsorbent as well as its chemical nature.

2.1.5 Molecular Dynamics (MD) Simulation

Molecular dynamics (MD) is a computer simulation method for analyzing atom and molecule physical movements. The atoms and molecules are allowed to interact for a set amount of time, providing a view of the system's dynamic "evolution." The trajectories of atoms and molecules are determined in the most common version by numerically solving Newton's equations of motion for a system of interacting particles, where forces between the particles and potential energies are frequently calculated using interatomic potentials or molecular mechanics force fields. The technique is mostly used in biophysics, materials science, and chemical physics [143].

In this thesis, MD simulation adopted to investigate the behavior of ammonium acetate solutions at the atomistic level using amber16 software.

2.1.6 Fourier Transform Infrared Spectroscopy - Attenuated Total Reflectance

FTIR is an effective method for identifying the chemical structure of different functional groups in a given sample. An infrared (IR) spectrum is obtained by passing IR radiation through a sample and determining what fraction of the incident radiation is absorbed in a particular wavenumber or frequency. The energy at which any peak in an absorption spectrum appears corresponds to the frequency of a vibration or bending of a part of a sample. Moreover, chemical bonds in different environments will absorb varying intensities and at varying frequencies. Thus, IR spectroscopy involves gathering absorption information and analysing it in the form of a spectrum [144, 145].

ATR (Attenuated Total Reflection) is an FTIR sampling method that enables the measurement of the sample directly in the solid or liquid state without further treatment. The phenomenon used here is the total internal reflection which generates an evanescent wave in the measured sample [144].

In this thesis, ATR spectra of aqueous solutions were carried out with an FTIR Brucker Alpha spectrometer equipped with an ATR head.

2.2 Electrochemical Characterisation

Note: The preparation method of the carbon based electrodes, the used separators, currents collectors, reference electrode, counter electrode, ect, will be mentioned in materials and methods section of the appropriate chapter.

The electrochemical measurements of the prepared electrodes performed in 3 electrodes configuration using 3 electrodes cell (**Figure 12**) includes: counter electrode, working and reference electrode. Moreover, in 2 electrodes configuration using a Swagelok-type cell, consisting of a Teflon body within which the sandwich: current collector-prepared electrode-separator-prepared electrode-current collector is deposited between two stainless steel pistons as shown in **Figure 13**.

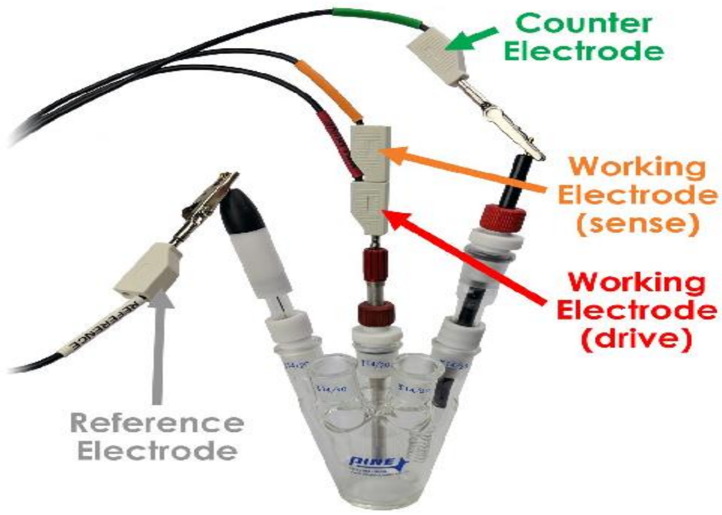

Figure 12. Three-Electrode Setup

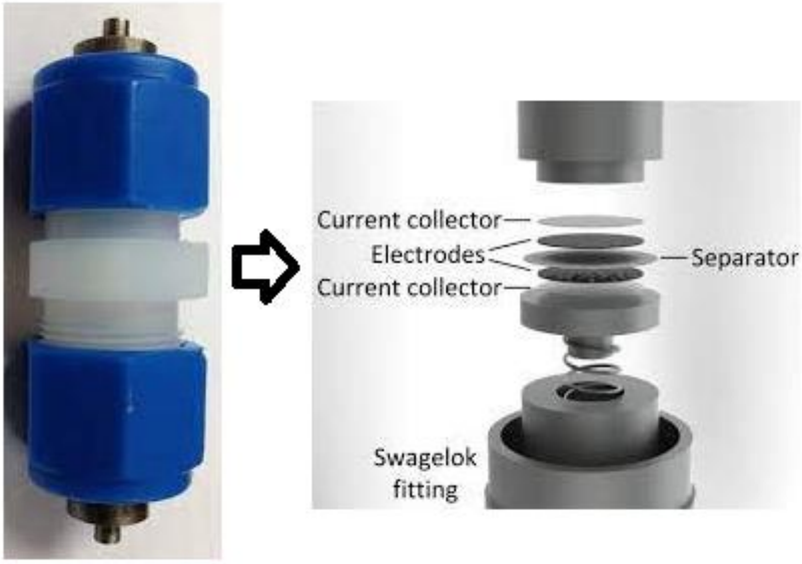

Figure 13. Two Electrode Swagelok Cell

Three main electrochemical characterization techniques were used: cyclic voltammetry, galvanostatic charge-discharge and electrochemical impedance. The measurements are carried out using a Bio-Logic VSP300 potentiostat/galvanostat controlled by the EC Lab software.

2.2.1 Cyclic Voltammetry

Cyclic voltammetry (CV) is a potentiodynamic electrochemical measurement technique. Typically, a linear potential sweep is carried out between two terminals E1 and E2, this sweep speed is expressed by Eq.3:

$$U = U_0 + vt \qquad (3)$$

With:

- U the potential of the electrode (in V)

- U_0 the potential of the open circuit of the electrode (OCV) (in V)

- v the scanning rate (in V / s)

- t time (in s)

By varying the potential of the studied electrodes, a current is produced as a result of the electrochemical reactions taking place in them, we then speak of a faradic current. In the absence of a faradic current, only the accumulation of charged ions on the surface of the polarized electrodes produces a current called capacitive. Cyclic voltammetry in particular allows us to know where the oxidation and reduction potentials of the species present in the studied electrolytes are located, to define the electrochemical limits of the electrolytes and electrodes used (electrochemical stability window) as well as to determine the specific capacitance (mass or surface) of materials.

The voltammogram of an ideal supercapacitor corresponds to a perfect rectangle (**Figure 14a**) where no faradic process is observed (absence of peaks) and where the phenomena are completely reversible. However, experimentally the intensity-potential curves generally present some differences compared to the perfectly rectangular voltammogram (**Figure 14b**). These differences are explained by the presence of electrical resistances in the supercapacitor system. These resistances due in particular to the electrolyte and to the diffusion resistance in the porosity of the electrodes material which affect the voltammetric signal.

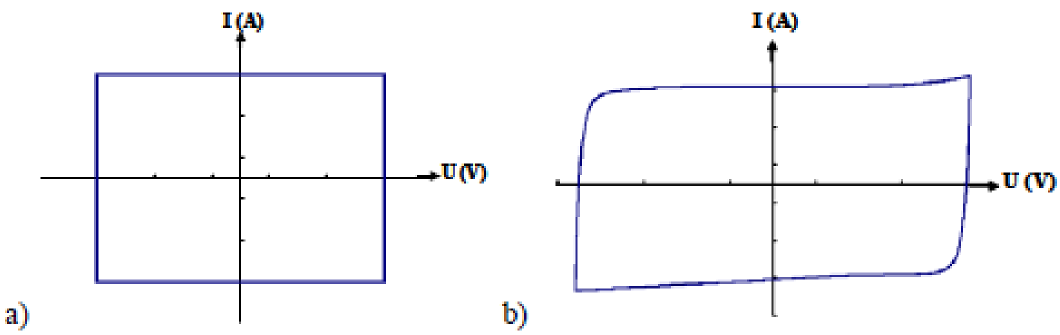

Figure 14. Voltamograms of ideal (a) and real (b) supercapacitive behavior.

Indeed, in its simplified representation, the electrode of a supercapacitor may correspond to a double layer capacitor in series with a resistance attributed to the electrolyte. Furthermore, and considering the porous nature of the electrode, a second resistance parallel to the double layer capacitance is required to exhibit the behavior of the electrode / electrolyte interface. All of these resistive contributions affect the signal and move it away from that of ideally capacitive behavior.

2.2.2 Galvanostatic Cycles

Galvanostatic cycling consists in following the evolution of the potential at the terminals of the system studied by imposing on it a constant current of intensity I. By applying a negative discharge current up to a low limit of potential (fixed by the study in voltammetry cyclic for example) and conversely a load current up to a high potential limit (set in the same way). The resulting voltage-time plot should ideally be linear with alternating positive and negative slopes (**Figure 12a**). For the same reasons as previously discussed deviations from linearity can occur, with series resistance causing the cell voltage to drop rapidly (**Figure 12b**) when switching from charging to discharging.

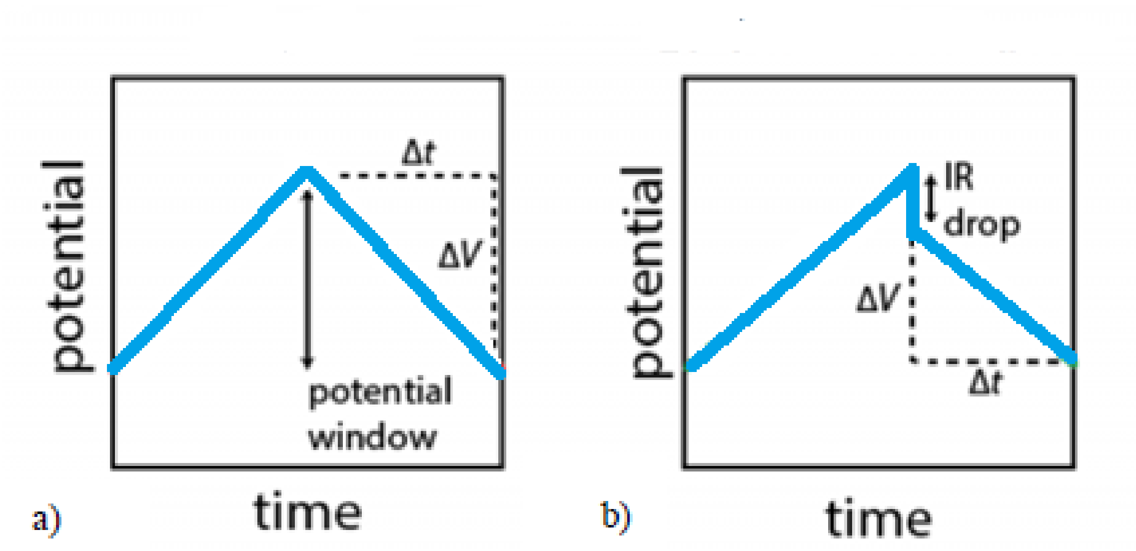

Figure 15. Galvanostatic charge-discharge curves: ideal (a) and non-ideal (b) case.

Galvanostatic cycling also makes it possible to know the cyclability of the supercapacitor by monitoring the performance over a large number of charge / discharge cycles.

The coulombic efficiency is frequently used to evaluate the cycle stability of electrode materials and devices by comparing the first and end cycles. When the charge–discharge current densities are equal, the coulombic efficiency (η) is defined as the ratio of discharging time to charging time. The following Eq can be used to calculate it:

$$\eta = \frac{tD}{tC} \text{ x } 100\% \qquad (4)$$

Where t_D and t_C are the discharge and charge times in seconds, respectively.

During cycling, an increase in resistance might take place. This increase can be related to the degradation of the materials constituting the supercapacitor; in particular, corrosion of current collectors, faradic surface reactions due to the presence of functional groups on the surface of carbons or decomposition of the electrolyte can occur. Likewise, during cycling, the capacitance of the cell decreases. The increase in resistance and decrease in capacitance should be as small as possible.

2.2.3 Electrochemical Impedance Spectroscopy

Electrochemical systems can be characterized by complex impedance spectroscopy. This technique consists in applying to the terminals of the cell a sinusoidal voltage of low amplitude and frequency *f* around a stationary voltage throughout the measurement:

$$U(t) = U0 + \Delta U \sin(\omega t) \quad (5)$$

with:

- U_0 the stationary voltage of the cell (V), in this case the open circuit voltage
- ω the pulsation in rad.s^{-1} (= $2\pi f$)
- ΔU the amplitude of the voltage variation (V)

The intensity of the generated current therefore varies sinusoidally with time, and has a phase shift φ with respect to the imposed voltage variation:

$$I(t) = I_0 + \Delta I \sin(\omega t + \varphi) \quad (6)$$

The voltage and current generated can also be written in complex form:

$E(\omega) = \Delta E\, e^{j(\omega t)}$

$I(\omega) = \Delta I\, e^{j(\omega t + \varphi)}$

Complex impedance is defined as the ratio of complex voltage to complex current according to Eq.7:

$$Z\omega = \frac{\Delta E}{\Delta I} e^{-j\varphi} = \mathbf{Z' + Z''} \quad (7)$$

With Z ’and Z’ ’the real and imaginary parts of the impedance, respectively. In an electrochemical impedance spectroscopy measurement, a broad frequency spectrum is scanned. The Nyquist diagram represents the opposite of the imaginary part versus the real part for each frequency, and is widely used to represent the impedance spectrum. The Nyquist diagram of a supercapacitor is shown in **Figure 16**.

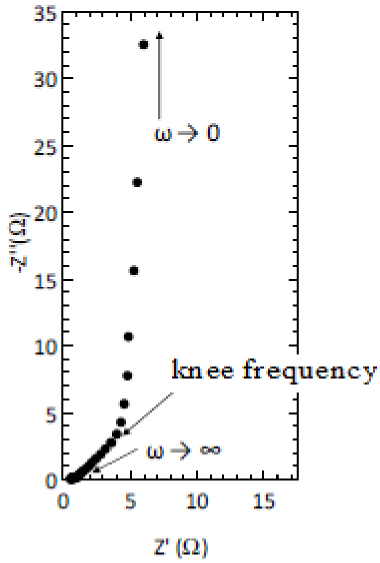

Figure 16. Nyquist plot of a carbon / carbon supercapacitor obtained by electrochemical impedance spectroscopy.

The complex impedance is constituted of a real part, which corresponds to resistance, and an imaginary part, which corresponds to capacitance. In porous carbon based supercapacitor the electrolytes ions adsorption take place at the surface of the electrodes. The movement of electrolyte ions from the bulk electrolyte to the electrode surface results a resistance corresponding to the uncompensated resistance, then ions penetrate further into the pore depth to charge with resistance. For symmetric device, the high frequency resistance corresponds to the so called equivalent series resistance (ESR). At high frequencies, the ions can only reach the electrolyte's outer surface, with real resistance denoted as ESR. When frequency decreases, at mid-frequency, the ions can move deeper into the pores, resulting higher resistance. At low frequency, both capacitance and resistance reach their theoretical maximums with no change, resulting in an almost vertical line. The "knee frequency" is defined as the intersection of the low frequency vertical line and the mid-frequency line.

CHAPTER 3: ARGAN SHELL-DERIVED CARBON AS SUPERCAPACITOR ELECTRODES MATERIAL

Energy density: 8.75 Wh kg^{-1}

Power density: 3.1 kW kg^{-1}

Equivalent series resistance: 0.21 Ω cm^2

Capacitance Retention (long-term cyclability test): 94 % after 10,000 cycles

Abstract

A low-cost and high-performance carbon material for supercapacitor electrodes is produced via a simple carbonization followed by chemical activation process using a renewable natural resource: Argan sells. Following an empirical approach the preparation parameters were optimized so as to obtain well-developed porosity and large surface area AC. Such characteristics make it possible to improve significantly electrochemical performance as revealed by the comprehensive testing carried out using lab Scale prototypes. So far the Argan shell derived carbon based electrodes tested with H_2SO_4 and KOH electrolytes exhibited interesting specific capacitance, high energy density and rate performances as revealed the tests carried out with symmetric supercapacitor cells. Thus, the valorisation of available and renewable agriculture by products as feedstock for an easier carbon derived electrodes may help contribution to local sustainable development in the context of circular economy through creation of high technology added value through application as ESDs such as SC_S.

3.1 Introduction

Despite the fact that lithium-ion batteries have governed the portable energy market for decades, there are expanding concerns about their operational safety, relatively low power density, and cycling stability [41, 146]. These concerns have sparked a lot of interest in developing next-generation of energy-storage devices with improved performance properties [147, 148], with SC_S being one of the most intriguing. The electrode materials and electrolyte used in SC_S are key components that determine their performance [146, 149]. AC_S have emerged as a highly marketable electrodes material due to their large specific surface area (SSA), high conductivity, reliable stability, and low costs [150, 151]. The use of ACs derived from biomass, particularly biowaste, has caught the interest of the energy-storage device community in recent years [96, 152-154]. The main reasons for their popularity are: the low cost, sustainability, abundance, and environmental friendliness of the raw materials, as well as the high performance of the resulting ACs [155, 156]. For these reasons, bio-waste based precursors such as bamboo [157, 158], orange-peel [79], cherry blossom [159], sunflower heads [160], sugar cane bagasse [161], mango stone [162], olive stone [96], coconut shell [163], almond shells [164], ect. have been used for the synthesis of Acs with supercapacitor application purpose.

In the present work an agriculture by-product resulting from oil extraction of the Argan fruit (Argania Spinosa) has been selected as precursor. UNESCO committee classified Argan tree as intangible cultural heritage of humanity in 2014, due to its multiple uses and contribution to the local economy as well as ecological sustainability, the [165]. The production of Argan fruit in Morocco is currently on the rise as a result of increasing worldwide interest in its culinary and cosmetic applications. So far, Morocco produced up to 4000 tons of Argan oil per year, leaving behind about 80,000 tons of hard shells per year[166]. Because there is no immediate use for such a large quantity of by-product, no significant economic value can be generated. Rather, it is primarily used as a domestic combustible by the local population[167]. However, these lignocellulosic-rich Argan shells [168, 169] are a promising precursor for developing porous AC_S-based for supercapacitor electrodes.

The use of such abundant and renewable bio-waste is critical not only for developing low-cost, high-performance ESDs, but also for transforming these wastes into high value-added product while addressing the circular economy and waste management issues. In this work, a simple pyrolysis and chemical activation strategy is used to produce a high-performance carbon material from Argan shells. The derived carbon electrodes with high surface area and well-developed porosity exhibits superior capacitive performances, including high specific capacitance, remarkable rate performance, and outstanding cycle stability obtained with aqueous electrolytes. Such performances making it promising candidate for high-performance supercapacitor electrodes that allow an important potential of economical valorisation.

3.2 Experimental

3.2.1 Preparation of Bio-Waste Argan Sells-Based Carbons

The carbonization process carried out for Argan shells (with 50 g of washed and dried shells) contained in a crucible placed in a stainless steel reactor, itself positioned inside a horizontal oven. After purging for 10 minutes under a flow of N_2, the reactor was heated under a flow of N_2 of 100 cm^3/min at a rate of 10°C/min until reaching 700°C, then maintained at this temperature for one hour. Finally, the reactor was allowed to cool to room temperature under a flow of 100 cc/min of N_2. The resulting char is designated AS-C.

The Argan shell precursor noted, AS-C, was crushed and sieved in order to retain the particle size fraction between 500 and 1000 µm. The chemical activation was carried out using sodium hydroxide (NaOH) or potassium hydroxide (KOH), according to two different methods: Impregnation (IM) and physical mixing (PM). In the case of the impregnation process, 4 g of AS-C precursor was impregnated in a solution containing 16 g of KOH or NaOH dissolved in 50 ml of distilled water and the solution was kept under stirring for 2 hours at 60°C. The resulting slurry was dried overnight in an oven at 110°C. Regarding chemical activation by physical mixing, 16 g of NaOH or KOH was physically mixed with 4 g of the AS-C sample at room temperature. It should be noted that this process was carried out in the absence of water. After impregnation and physical mixing, the samples obtained were heat treated under a flow of 600 cm^3/min of N_2 in a programmable temperature oven following the sequence below:

- Heating from room temperature to 850°C with a rate of 5°C/min;
- Hold at 850°C for one hour;
- Cooling to room temperature.

After the heat treatment, all the activated carbons were washed with an HCl solution (5 M), then with distilled water until reaching neutral pH, and then dried at 110°C overnight.

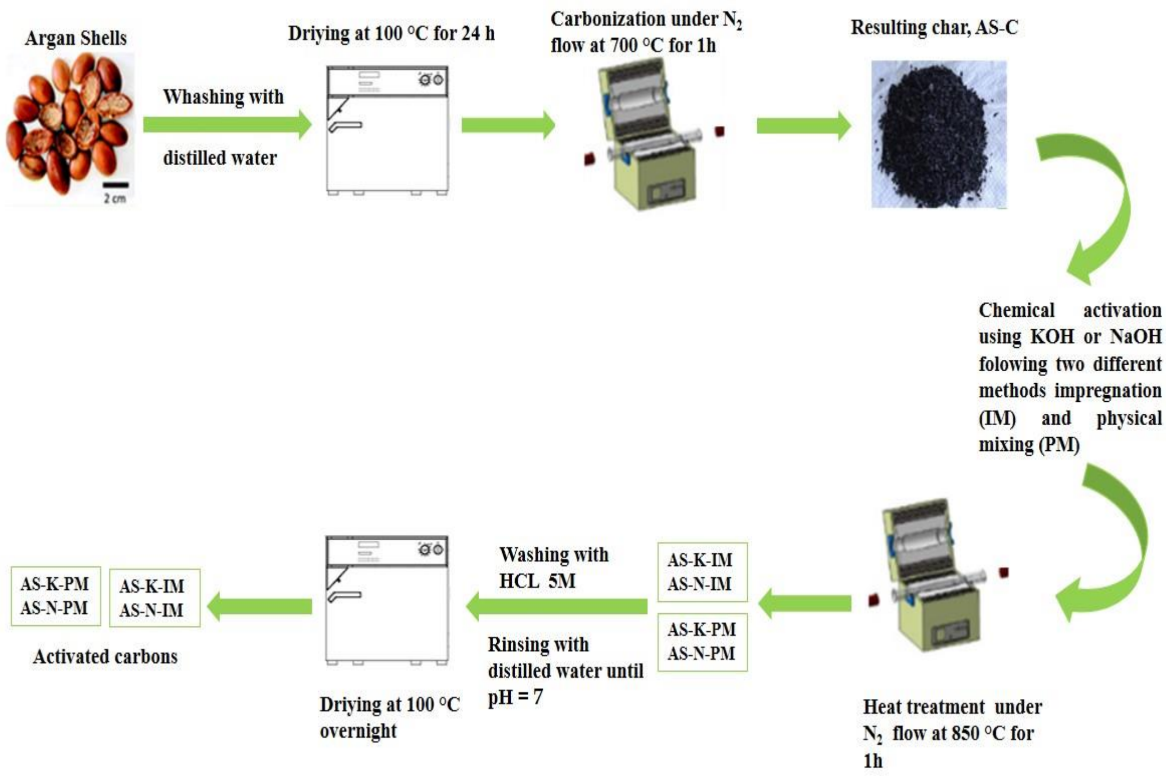

Figure 17. Summary of the preparation process of activated carbons from Argan shells.

Table 5 groups the nomenclatures of the various activated carbons prepared according to the type of precursor, the activating agent and the method of preparation.

Table 5. Nomenclature of the different activated carbons.

Agent activant	**Activation method**	**Sample nomenclatures**
KOH	Impregnation (IM)	AS-K-IM
	physical mixing (PM)	AS-K-PM
NaOH	Impregnation (IM)	AS-N-IM
	physical mixing (PM)	AS-N-PM

3.2.1 Textural Characterizations of the as Prepared Samples

SEM micrographs of AS-K-IM and AS-K-PM samples, gotten after activation with KOH applying impregnation and mixing methods, are shown in **Figure 18a** and **b**, respectively. A honeycomb-like structure with large spherical cavities appears to be present in both samples. Furthermore, in contrast to the smooth cavities of AS-K-PM, the surface of AS-K-IM has rifts and crannies caused by chemical etching throughout the liquid phase in the impregnation process. The SEM images of AS-N-PM and AS-N-IM samples obtained after activation with NaOH (**Figure 18c** and **d**, respectively) display irregular and heterogeneous surface morphology with pores of various sizes and shapes.

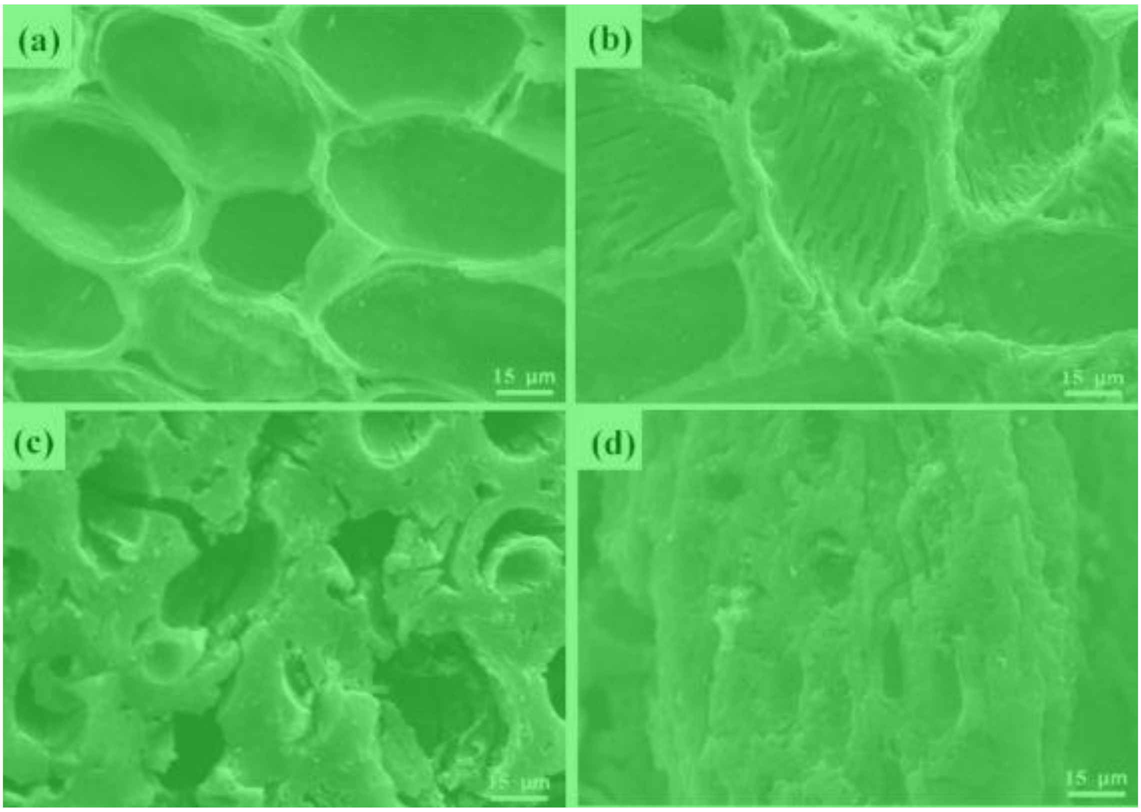

Figure 18. SEM micrographs of the prepared activated carbons: (a) AS-K-PM, (b) AS-K-IM, (c) AS-N-PM and (d) AS-N-IM.

The surface functional groups on the prepared ACs were evaluated using FTIR transmission spectra. The FTIR spectra of AC gotten within the wave numbers 3600 to 700 cm^{-1} are shown in **Figure 19**.

The band observed in the 3400 cm^{-1} region corresponding the stretching vibration of an O–H. The second peak at 3228 cm^{-1} could be attributed to N–H stretching alkyl or aryl amine. The band near 2995 cm^{-1} matches up to C-H stretching, particularly in polynuclear systems. Peaks about 2922–2854 cm^{-1} can be related to asymmetric and symmetric C-H stretching in alkyl groups such as methyl and methylene [170]. The $RCONH_2$ structure was observed at 1653 cm^{-1}, which used to be the amides group final confirmation proof [171]. A strong band at 1558 and 1498 cm^{-1} can be attributed to C=O in carbonyl and carboxylic groups respectively. The bands at 1267–1187 cm^{-1} can be associated to C-OH stretching vibrations in the carboxylic, phenolic or lactonic groups suggesting the presence of oxygen functional group. As reported by D Prahas et al., the bands at 1078 and 815 cm^{-1} may be related with esters such as CH3-CO-O- as well as with cyclic C-O-C groups conjugated with carbon–carbon doubles C=C-O-C in aromatic structures [172].

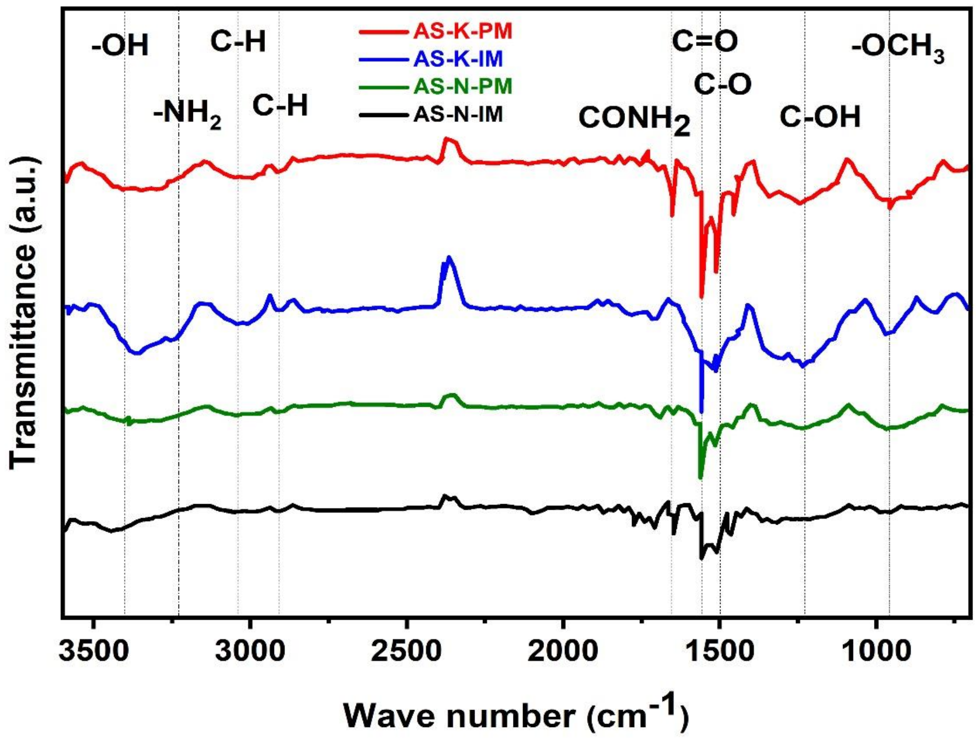

Figure 19. FTIR spectrum of all prepared activated carbons.

The X-ray diffraction patterns of the as-prepared AC samples and the carbonized precursor (AS-C) are shown in **Figure 20**. The AS-C sample's XRD profile revealed two broad humps at approximately 2θ ~25° and 2θ ~43°, which are closely associated with the (002) and (100) graphitic planes, respectively [173]. There were no other well-defined peaks associated with any other distinct phases, which is typical of amorphous carbons of this type. However, after activation of the AS-C samples, these two humps almost disappeared in all of the AS-N-IM, AS-N-PM, AS-K-PM, and AS-K-IM samples, implying destruction of graphitic crystalline planes, which would be an intended effect of the activation process. However, a key finding is the development of high-intensity X-ray diffraction patterns at lower scattering angles (<2θ ~ 15°), revealing the porosity development, which can be linked to defect generation during the activation process [174].

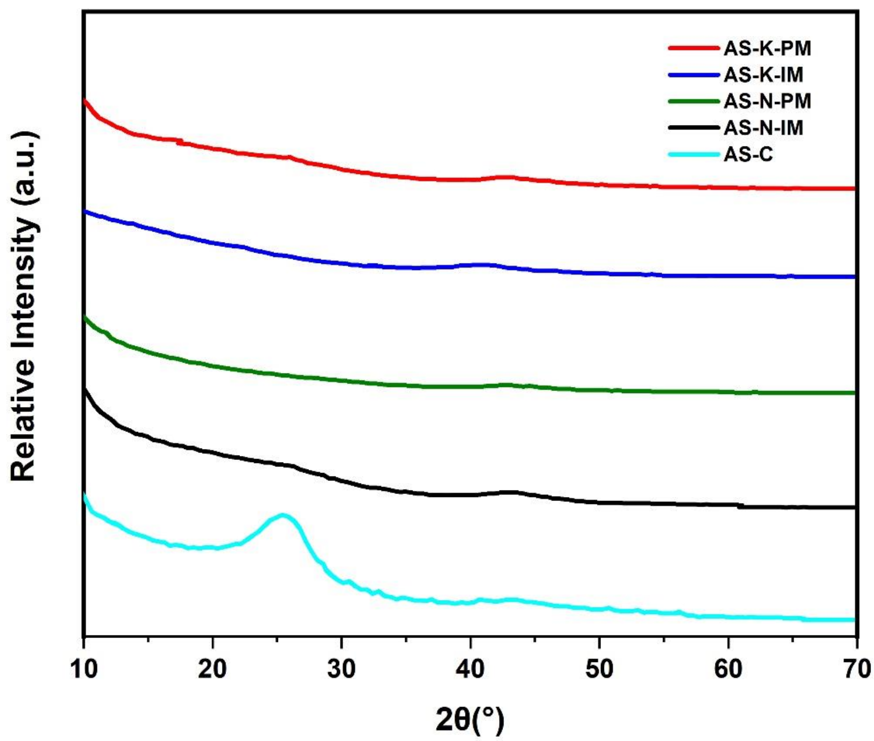

Figure 20. X-ray diffraction patterns of the carbonized precursor and the prepared activated carbons.

The Raman spectrum of the prepared active carbons and the carbonized precursor is shown in **Figure 21**. There are two peaks in all of the as-prepared carbon samples, located at 1350 cm^{-1} and 1580 cm^{-1}, which correspond to the D and G bands of graphitic material, respectively. The D band is related to the vibration of disordered sp^3 carbon, while the G band is due to the vibration of sp^2 carbon [175]. The graphitization degree of the samples is indicated by the I_D/I_G intensity ratio. Where that, the graphitization degree is inversely proportional to the I_D/I_G intensity ratio. When comparing the spectra of the AC_S to those of AS-C, the intensity ratio of the AC_S was found to be higher. This appears to be linked to a decrease in the graphitization degree of AC_S as a result of the activation treatment destroying the graphitic crystalline structure within the AS-C. The results that are in good accord with the above XRD results, suggesting that AC_S are very defective. Several investigations have found that defects on carbon layers can alter the surface properties, hence improving EDLC [176, 177]. As a result, the AC_S with the most defects are thought to have a high capacitance.

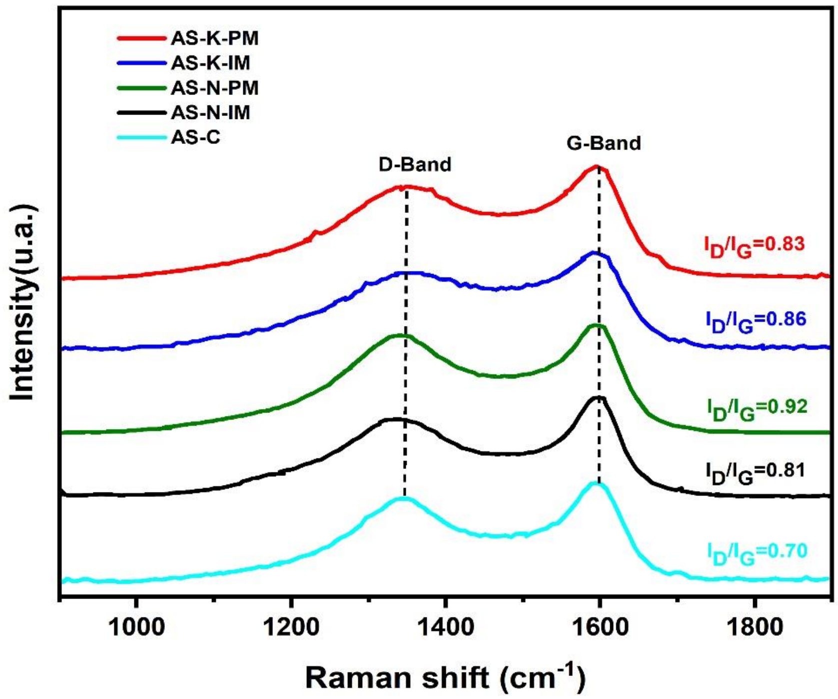

Figure 21. Raman spectra of the prepared activated carbons and the carbonized precursor.

The nitrogen adsorption isotherms measured at 77 K were used to investigate the developed porosity within the activated samples; the adsorption isotherms are included in **Figure 22**. Which are characteristic of type I with steep uptakes below $P/P_0 = 5 \times 10^{-4}$, demonstrating mainly microporous materials [46]. **Table 6** summarizes the textural parameters of the synthesized active carbons and the carbonized precursor. The BET surface area and total pore volume rise considerably following activation, from 51 m^2/g and 0.04 cm^3/g for the AS-C sample to 2251 m^2/g and 1.04 cm^3/g.

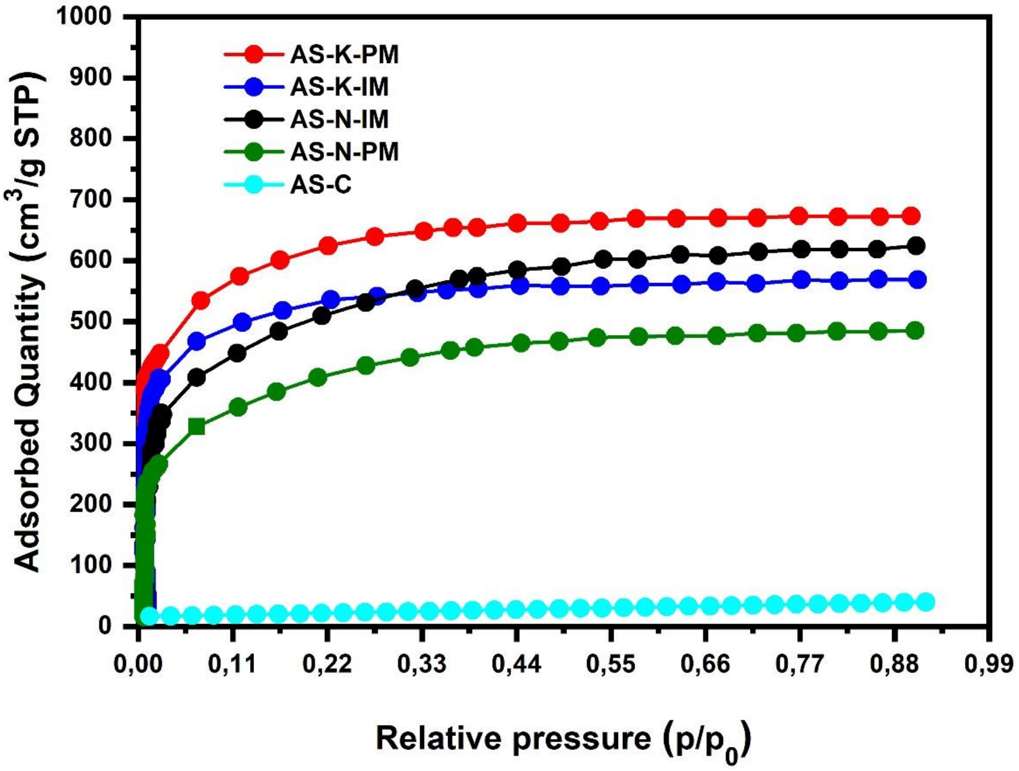

Figure 22. Nitrogen adsorption isotherms measured at 77 K for the prepared activated carbons and the carbonized precursor.

Table 6. Textural parameters of the carbonized precursor and the prepared activated carbons.

Sample	S_{BET}	**Pore volume (cm^3/g)**			
		V_T	V_{micro}	V_{meso}	V_{micro}/V_T (%)
AS-C	51.54	0.04	0.02	0.02	50.00
AS-K-PM	2251.04	1.04	0.93	0.11	89.42
AS-K-IM	1889.63	0.87	0.80	0.07	91.95
AS-N-PM	1462.71	0.74	0.58	0.16	78.37
AS-N-IM	1826.96	0.96	0.73	0.23	76.04

The pores size distribution (PSD) derived from N_2 adsorption isotherms, using DFT calculations are displayed in **Figure 23**. It is clear that the produced porosity is mostly microporous in nature, with a small amount of mesopores, as shown by the shoulders between 20 and 40 Å. This micro- and mesoporous AC_S distribution can provide a large surface area for electrosorption of electrolyte ions and convenient paths for ion diffusions, resulting in significantly quicker ion transfer[178, 179]. Remarkably, the KOH activated samples had a greater amount of nanopores than the NaOH activated samples, while the AS-K-PM sample had the highest specific surface area.

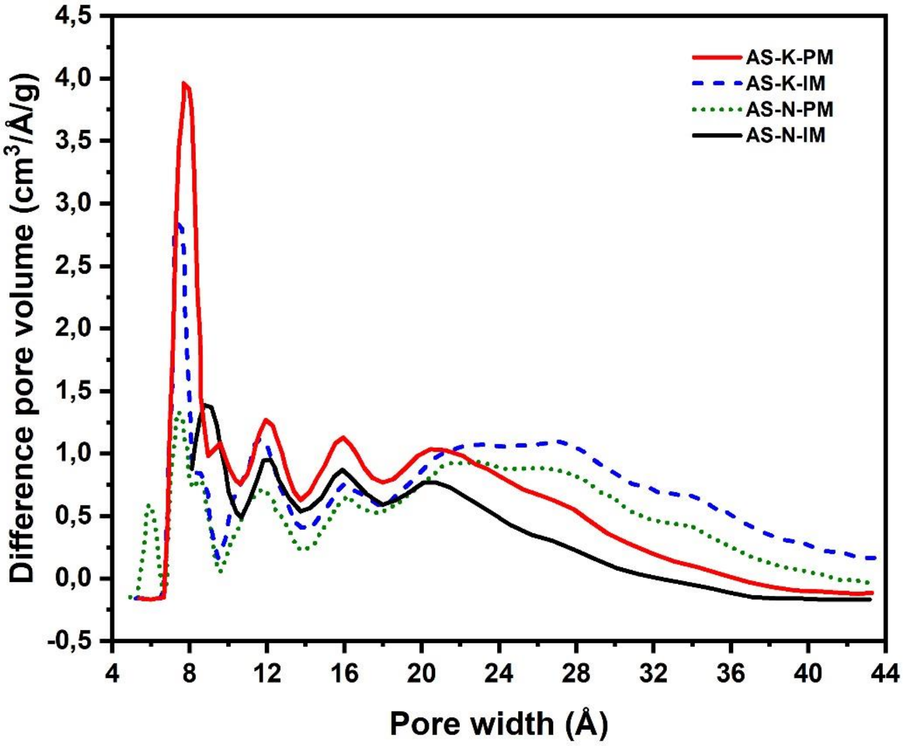

Figure 23. Pore size distribution of the prepared activated carbons.

Based on the above structural and textural characterization results and some previous primarily electrochemical test of all the samples, the AS-K-PM sample showed better capacitance behaviour, therefore in this study this sample was used as electrodes material for assembling supercapacitor cells using aquouse electrolyte.

3.2.2 Electrodes Preparation

The working electrodes were prepared using homogeneous mixture of 90% Argan sells derived activated carbon AS-K-PM and 10% poly(tetrafluoroethylene) binder PTFE (60% suspension in water) dried overnight at 100 °C, then pasted by pressure at 5 bar on two identical 5 mm graphite discs. The graphitic electrodes were impregnated with the appropriate electrolyte for 48 hours before electrochemical measurements.

In order to investigate the potential application of AS-K-PM as electrodes material for aqueous supercapacitor device, the impregnated electrodes were assembled in a two-electrode configuration using 1M H_2SO_4 and 6 M KOH as electrolytes and glass fibrous material as a separator.

3.2.3 Electrochemical Measurements

The symmetric SC_S were characterized using cyclic voltammograms (CV), galvanostatic charge-discharge experiments (GCD), impedance measurements, and cyclability test. These analyses were coupled to provide information concerning supercapacitor performance at various scan rates, current density, and capacitive retention after multiple uses. Such properties are, throughout turn, measures of power density, energy density, and capacitive retention.

The cyclic voltamogram CV curves of the assembled cells were carried out within voltage range of 0 to 1 V in 1M H_2SO_4 and of 0 to 0.6 V in 6 M KOH, using scan rates ranging from 5 to 100 mV s^{-1}. are depicted in **Figure 24 a-b)**. Worth noting that even when the scan rates increase from 5 to 100 mV s^{-1}, all the CV curves show reversible and quasi-rectangular shapes typical for electrochemical double-layer (EDL) capacitors with a low diffusional restriction to the electrolyte indicating well developed porosity.

The GCD plots at different current densities were shown in **Figure 24 c-d)**. At all the tested current densities from 0.1 to 3 A g^{-1} the GCD curves assembled cells have quasi-triangular shapes, which indicate again that the AS-K-PM has good capacitive behaviour with low resistance and a very good diffusion of the electrolyte inside the pores. In addition, linear and symmetrical shapes of the charging and discharging curves, indicates excellent electrochemical reversibility.

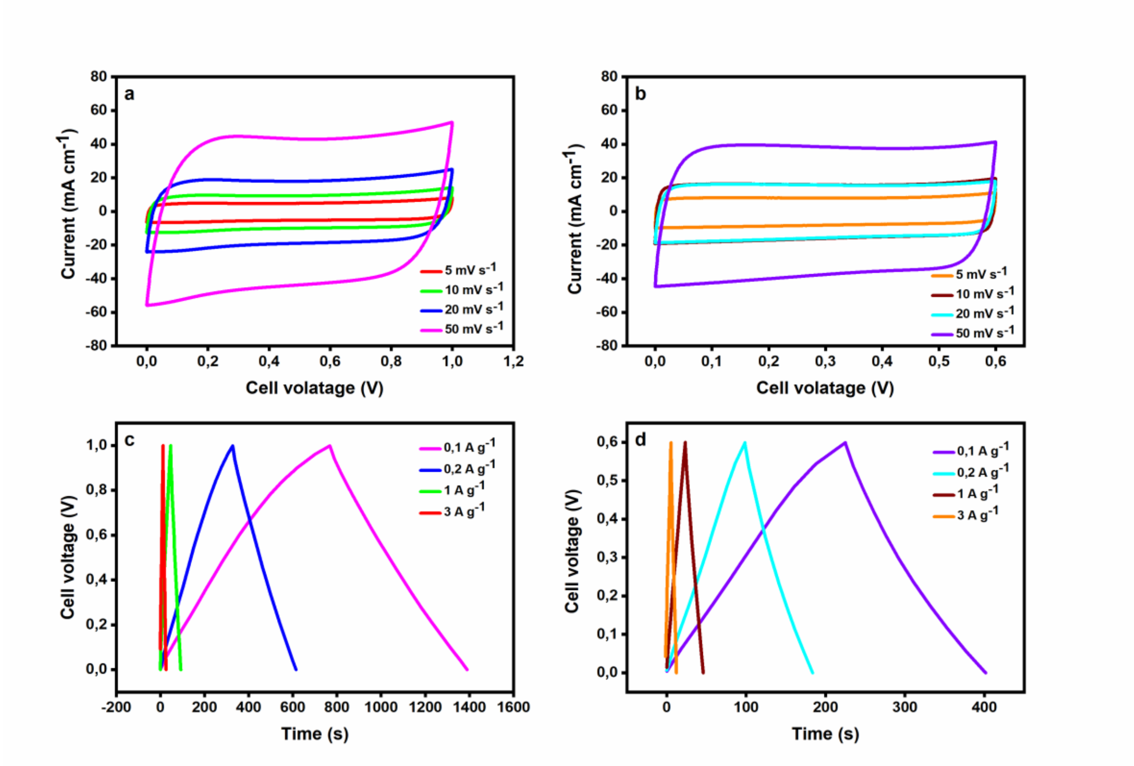

Figure 24. Electrochemical performance of the assembled AS-K-PM based symmetric devices: CV curves at various scan rates with H_2SO_4 electrolyte a) and with KOH electrolyte b); GCD curves at various current densities with H_2SO_4 electrolyte c) and with KOH electrolyte d).

Based on the GCD curves, the specific capacitance of the assembled symmetric cell was calculated using the following Eq:

$$C_{sp} = (I \times dt / m \ dV) \quad (8)$$

Where I is the discharge current (A), dV/dt is the slope of the discharge curve, and m is the total mass of the two electrodes (in g).

The specific energy (E) and power (P) were determined by applying Eq. (9) and (10) respectively:

$$E\ (Wh\ kg^{-1}) = 1 / 2 \times Csp\ (Fg^{-1}) \times \Delta V^2\ (V) \quad (9)$$

$$P(W\ kg^{-1}) = E\ (Wh\ kg^{-1}) / \Delta t\ (s) \quad (10)$$

The variation of the capacitances as a function of current density are shown in **Figure 25**. The AS-K-PM based electrode exhibits higher specific capacitance of 250 F g^{-1} in 1 M H_2SO_4 and 192 F g^{-1} in 6 M KOH electrolyte at current density of 0,1 A g^{-1}. In both electrolytes, the electrodes showed a little decreases in the capacitance as the current density increases, that due to the difficulty of forming the EDL in the microspores at high current intensities. Higher capacitance values are obtained when using H_2SO_4 vs KOH, which must be related to the nature and size of the cation (H^+ vs K^+). Because H^+ cations are smaller than K^+ cations, their mobility is higher which yields to decreased resistance to the electrolytes, therefore higher capacitance.

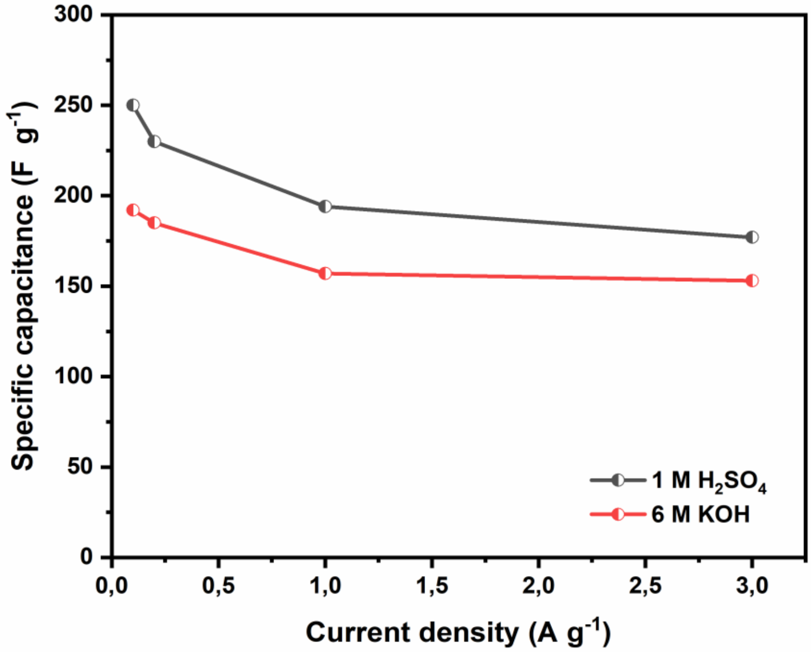

Figure 25. The variation of the capacitances as a function of current density of the AS-K-PM based electrodes in H_2SO_4 and KOH electrolytes.

The Ragone plots of the AS-K-PM based assembled symmetric cell in both electrolytes obtained by using the GCD discharge curves at different current densities are shown in **Figure 26**. It is indicated an energy density value reaching 8.75 Wh kg^{-1} at power density of 50 W kg^{-1} in H_2SO_4 electrolyte. Note that this value of energy density is larger than that of many other biomass derived carbon reported in the literature. For the same electrolyte the power density reached 3.1 kW kg^{-1} while the energy density still remained 6.15 Wh kg^{-1}. On other hand, the maximum energy density obtained in KOH was 2 Wh kg^{-1} at power density of 1.7 kW kg^{-1}.

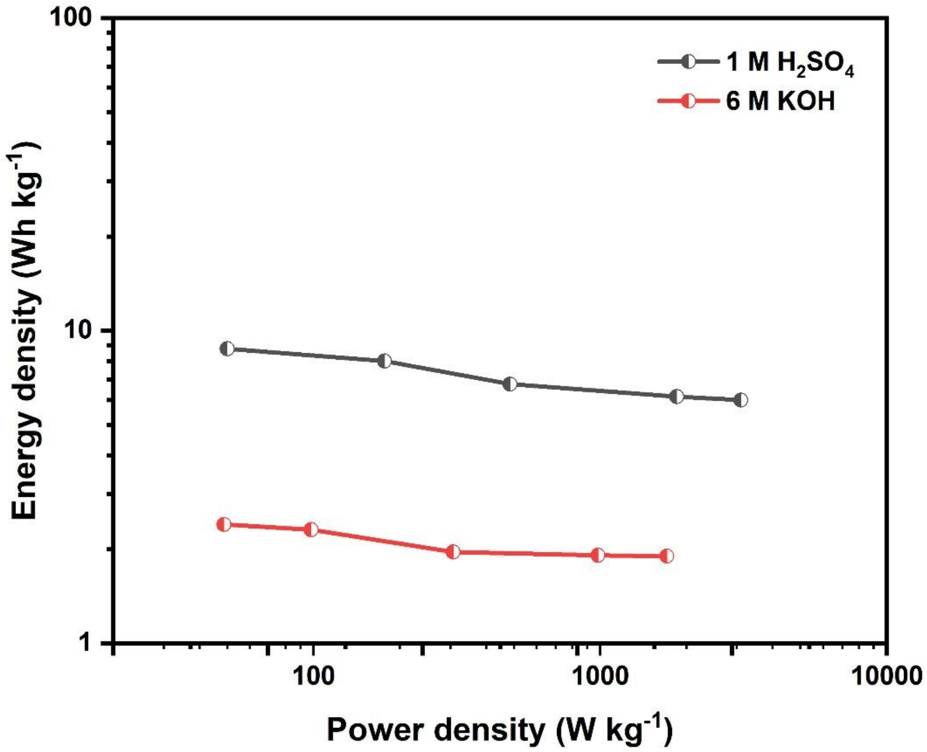

Figure 26. The Ragone plots of the AS-K-PM based assembled symmetric cell with H_2SO_4 and KOH electrolytes.

The impedance spectroscopy EIS measurements of AS-K-PM assembled symmetric cell were carried out from a frequency of 1 mHz to 100 kHz with a sinusoidal signal amplitude of 10 mV. In both cases (assembled cell with H_2SO_4 and with KOH electrolyte), the Nyquist plot in **Figure 27** shows a straight line at low frequency, indicating ideal electrodes capacitive behavior with low ionic diffusion resistance inside the porous network and across the electrode–electrolyte interfaces. The intercept in the high frequency region at the real axis corresponds the equivalent series resistance (ESR) which combines the bulk resistance of the porous carbon material, the bulk resistance of the electrolyte and the contact/interface resistance between the electrode and the current collector [180]. ESR of both cells is as low as 0.2 Ω. The resistance of the ion transfer at the electrode interface, Ri, was determined by measuring the semicircle diameter (the distance between the two intercepts of the semicircle with the real axis). The founded values are 0.21Ω and 0.79 Ω for the cell assembled with H_2SO_4 and KOH respectively. Ri value for the cell assembled with H_2SO_4 is nearly four time lower than that of the cell assembled with KOH. This finding proves that a faster charge transfer coupled with improved electrolyte ion accessibility into electrode material pores. In addition, the slope is steeper in the case of H_2SO_4 than that in KOH, indicating superior capacitive performance. Which matches the CV and GCD results discussed before.

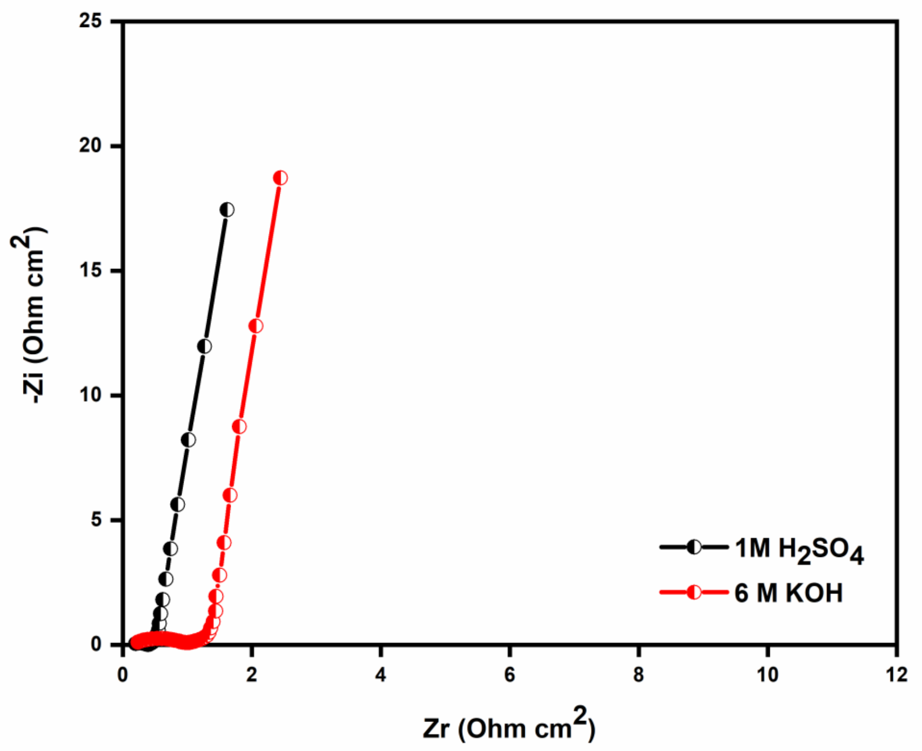

Figure 27. Nyquist plot of the assembled AS-K-PM based symmetric devices with H_2SO_4 and KOH electrolytes.

The long-term stability test of the device is an additional key factor in the SC_S practical applications. **Figure 28** shows the variation of the capacitance with the number of charge-discharge cycles at a constant current density of 1 A g^{-1}. After 10,000 cycle, the cell with H_2SO_4 and with KOH electrolytes exhibit a capacitance retention of 94% and 82% respectively. The higher capacitance retention of the cell with H_2SO_4 electrolyte is again thanks to the high ionic conductivity of the electrolyte's ions and their compatible size with the developed porosity of electrodes material.

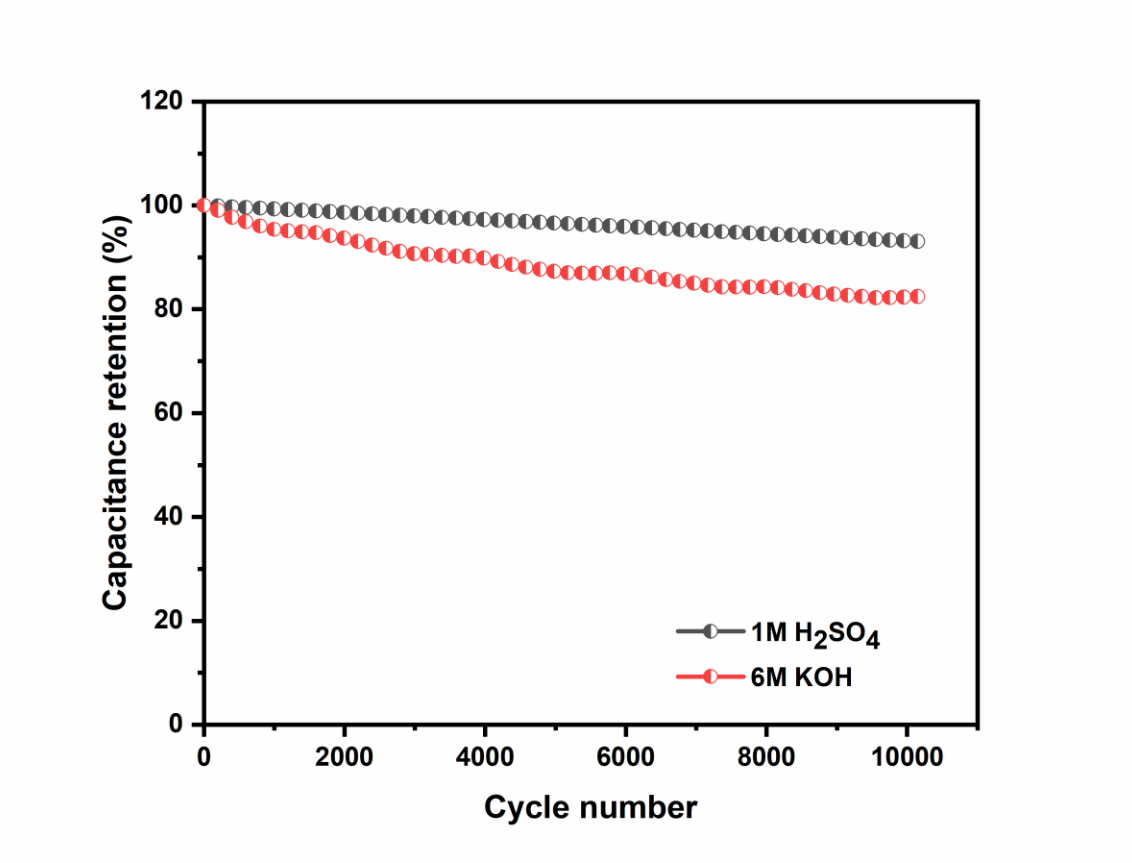

Figure 28. Cyclic stability test of the assembled ARG-AC based symmetric devices with H_2SO_4 and KOH electrolytes.

3.3 Conclusion

In summary, the agricultural waste such as Argan shells can be transformed into high added value carbon material for the preparation of SC_S electrodes. The optimisation of preparation parameters allow selecting a sample with interesting textural characteristics as indicated by the obtained high specific surface area and the well-developed porosity. The resulting carbon based electrodes using the selected sample permit obtaining interesting electrochemical performances as revealed by high capacitive response using H_2SO_4 and KOH electrolytes. At current density of 0,1 A g^{-1}, a high specific capacitance of 250 F g^{-1} and 192 F g^{-1} was obtained in 1 M H_2SO_4 and 6 M KOH electrolytes respectively. However, the assembled symmetric cell with H_2SO_4 showed a highest energy density reached 8.75 Wh kg^{-1} and a highest power density reached 3.1 kW kg^{-1} . Interestingly, the cells showed very low resistance of 0.21Ω cm^2 and 0.79 Ω cm^2, and good capacitance retention of 94% and 82% after 10,000 GCD cycle at 1 A g^{-1}, obtained with H_2SO_4 and KOH electrolytes respectively. Hence such promising electrochemical performances, may help valorisation renewable agriculture waste (Argan shell) as promising candidate for applications as supercapacitor electrodes.

CHAPTER 4: NATURAL COAL-DERIVED CARBON AS SUPERCAPACITOR ELECTRODES MATERIAL

Energy density : 7 Wh kg^{-1}

Power density: ~1.7 kW kg^{-1}

Equivalent series resistance: 0.2 Ω cm2

Capacitance Retention (long-term cyclability test): 99 % after 10,000 cycle

Abstract

High performance supercapacitor electrodes were successfully prepared using AC prepared from Moroccan anthracite natural coal. The Anthracite-derived AC prepared by one-step synthesis via KOH activation at 850 °C in N_2 atmosphere characterize by a very high surface area of 2934 m^2/g with a total pore volume of 1.33 cm^3/g and micro-mesopores distribution. The tests carried out with electrodes assembled within a symmetric prototype using 1M H_2SO_4 electrolyte show maximum capacitance of 50.3 F g^{-1}, energy density of 7 Wh kg^{-1}, power density of 13.5 kW/kg, and specific capacitance retention of 98.7 % after 10,000 cycles. The obtained electrochemical performance obviously demonstrates that anthracite-derived AC is a promising materials for supercapacitor electrodes. This paves the way to creation of added economical value to available local resources such anthracite through local production of derived carbon materials with potential application in ESDs such as SC_S.

4.1 Introduction

Efficient energy storage is one of the most important challenges concerning sustainable development and integration of renewable energy goals. Today, the growing interest devoted to transition to renewable energy technologies as well as electric mobilities pushes to accelerated evolution of energy storage systems. Recently, research efforts have been devoted to the development of high performance ESDs, including batteries, fuel cells, as well as SC_S [181]. Because of their exceptional power density, fast charge-discharge rates, excellent cycle life, and relatively low cost; SC_S have been considered as one of the most attractive energy storage system. With the aim of improving the SC_S performances, much work have been done to develop effective electrodes [182-185]. According to the literature, carbon-based materials are excellent candidate for SC_S due to their high conductivity, controllable structures, great power density, long life cycle and environmental friendliness [186-188].

Despite these potential advantages, industrial applications of some reported carbon materials, such as graphene and CNTs -based materials, are still impractical due to limited mass production, a complicated synthesis process, and the use of expensive raw materials as precursor. On the other hand, AC is preferred as the most cost-effective material for supercapacitor which could be prepared from abundant raw materials such as biomass (e.g. plants, wood, agricultural waste .etc.) and mineral resources (e.g. different types of coal). Among the preparation process of activated carbon from the previous precursors, chemical activation is considered among the most efficient, because of its simplicity and the developments of high porosity and interesting pore size distributions of interest for SC_S application [189]. Anthracite coal has major advantage regarding high carbon content [98] and therefore, its transformation into higher economic value materials using non-combustion technology may open interesting market concerning electrodes for ESDs [190]. Herein, an Anthracite collected from the oriental region of Morocco was used as precursor to prepare activated carbon using chemical activation process, with the aim of use as materials for supercapacitor electrodes. The obtained carbon material displays large specific surface area, meso-micropores size distribution, excellent specific capacitance and superior cyclic stability in aqueous electrolytes that make it a promising candidate for supercapacitor application.

4.2 Experimental

4.2.1 Preparation of Anthracite Based Activated Carbons

First, the collected raw anthracite from the oriental region of Morocco was washed with deionized water, dried at 100 °C overnight, crushed and sifted to obtain a fraction between 500 and 1000 µm. Next, the obtained powder AN-Raw underwent a chemical activation using potassium hydroxide or sodium hydroxide as activating agent. The powder was physically mixed with KOH or NaOH lentils in a mass ratio of 1/4 (4g of anthracite powder with 16g of KOH lentils) at room temperature. Then each mixtures was heated in controllable furnace for 1h at 850 °C with a heating rate of 5 °C/min under N_2 flow of 600 cm^3/min, by the end the mixture maintained until cooling down to the room temperature. Finaly, the obtained AC_S were rinsed once with chloridric acid (5M HCl) followed by multi-time rinse with distillated water until reaching neutral pH, then dried at 110 °C overnight. The as prepared AC named AN-K-AC and AN-N-AC for the sample activated with KOH and NaOH respectively.

4.2.2 Textural and Structural Properties of the Obtained Activated Carbons

SEM was used to examine the surface morphology of AN-Raw and as-prepared AC_S. As shown in **Figure 27**, the AN-Raw displaying a compact and dense surface (**Figure 29a**), while the pictures of AN-K-AC and AN-N-AC samples following activation (**Figure 29b** and **c**, respectively) exhibit irregular and heterogeneous surface morphology with pores of various sizes and shapes.

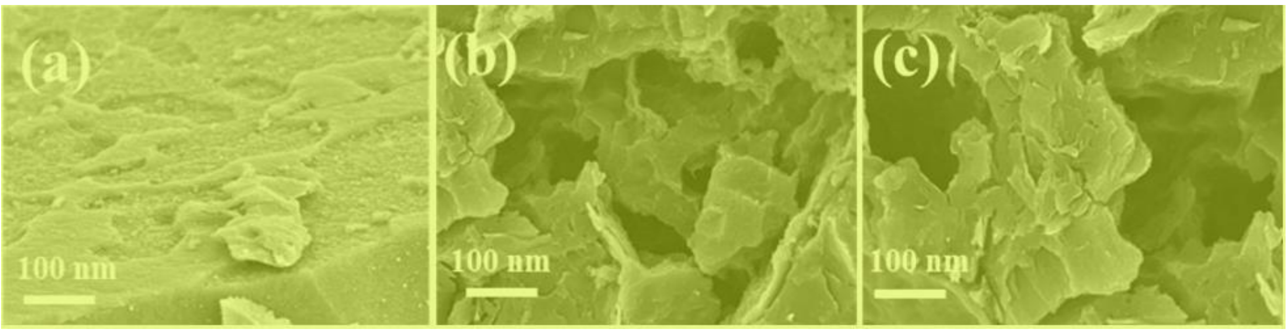

Figure 29. SEM micrographs of the (a) AN-Raw and the prepared AC_S: (b) AN-K-AC and (c) AN-N-AC.

The crystalline structure of the AN-Raw and as-prepared ACs was further investigated using X-ray diffraction and Raman spectroscopy. The AN-Raw exhibits two broadened diffraction reflections, located at about $2\theta = 25.6°$ and 43.5°, respectively, as shown in **Figure 30**. The two reflections are analogous to graphite's (002) and (100) planes, revealing amorphous carbon's dominating features [173]. The peaks of (002) and (100) were significantly broadened after activation, and their intensities dropped drastically for all samples, revealing reduction in the crystallinity and the graphitization degree in the as-obtained AC_S, producing defect generation and thus pore development due to the activation by KOH and NaOH throughout the chemical etching process.

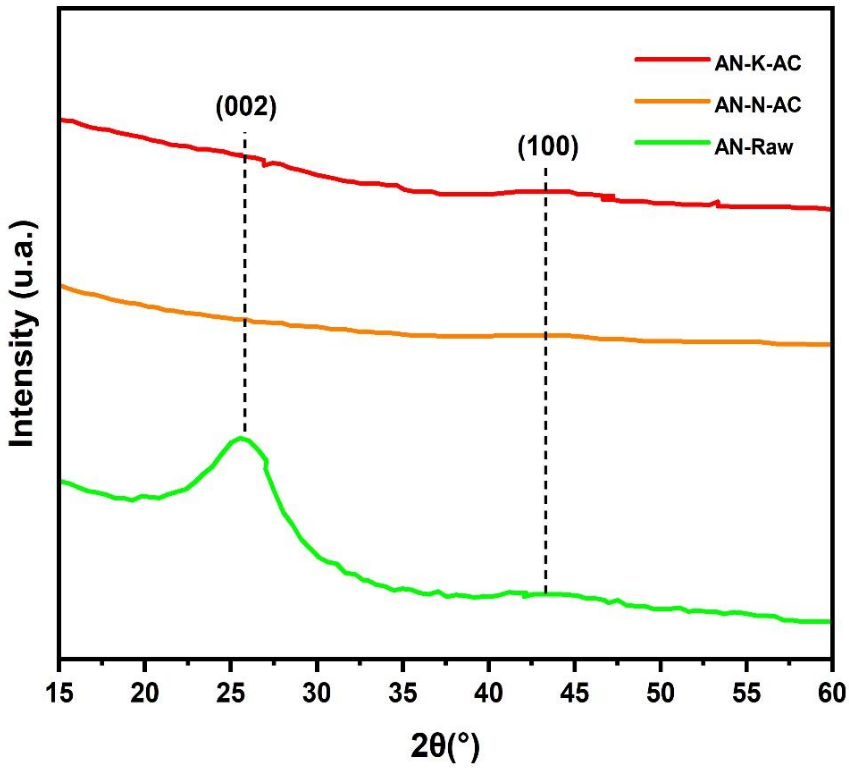

Figure 30. (a) X-ray diffraction patterns of the prepared ACs and the AN-Raw.

The Raman spectra of all the as-prepared carbon materials and the AN-Raw in **Figure 31** show two prominent peak positions at 1330 cm^{-1} and 1598 cm^{-1}, corresponding to the D (vibration of disordered sp^3 carbon) and G bands (ordered sp^2 carbon) respectively [175]. According to Raman spectra, The AC samples had a higher I_D/I_G intensity ratio than the AN-Raw sample. This also approving the reduced crystallinity of the structure within the AN-raw sample [191], which is in accord with the XRD results. As previously stated, many defects on carbon layers can influence surface morphology, increasing overall surface area and consequently EDLC. As a result, AC_S with higher defect densities are expected to exhibit higher capacitance [177]. These defect densities are assumed to be highly relying on the nature of the used activating agents, and we intend to achieve a tailored porosity by using two different agents (KOH and NaOH).

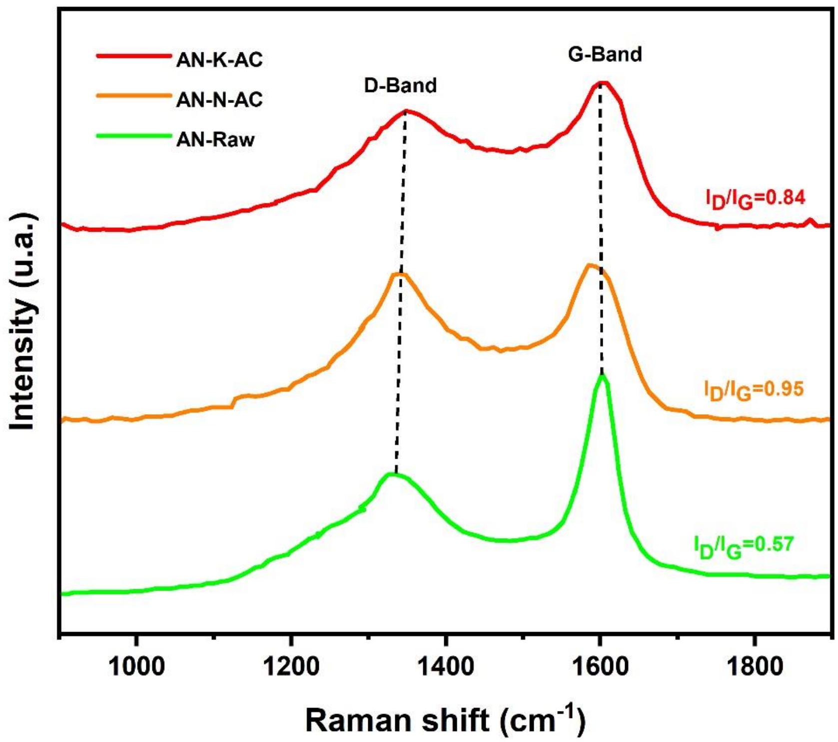

Figure 31. Raman spectra of the prepared ACs and the AN-Raw.

N_2 adsorption isotherms were used to study the porous structures of the as prepared AC_S. As envisaged, the acquired results follow the pore size distribution patterns (**Figure 32**). Significantly, all of the obtained isotherms are type I, exhibiting similar adsorption behavior at low relative pressures ($P/P_o < 0.05$), indicating the presence of high amount of micropores (pore width < 2 nm) in the investigated samples [46].

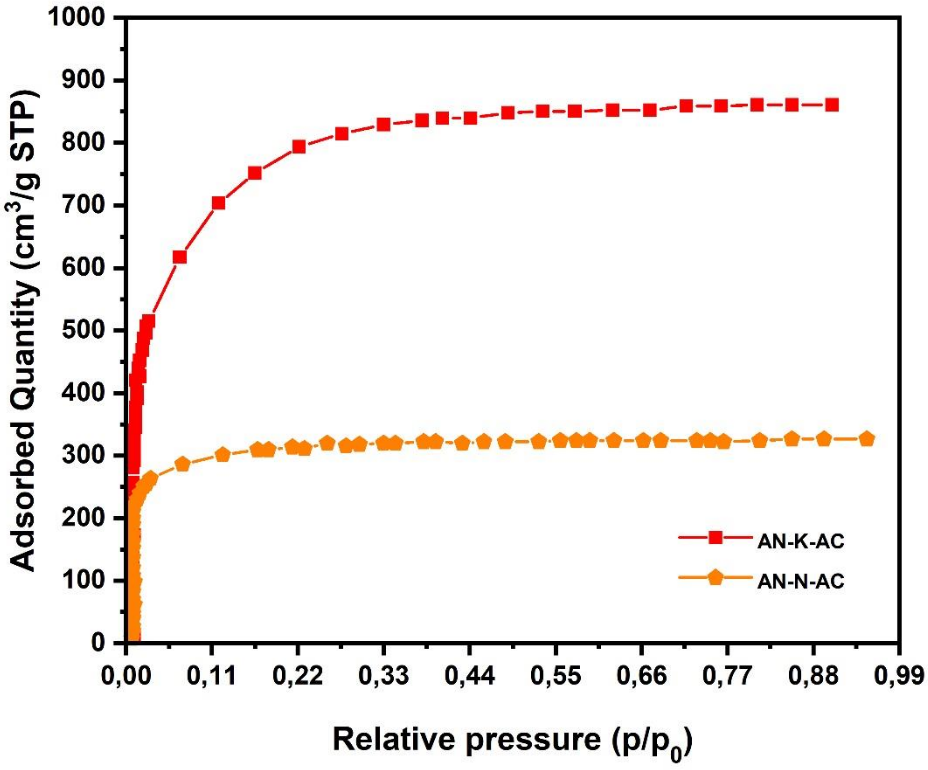

Figure 32. Nitrogen adsorption isotherms measured at 77K of the prepared AC_S.

The isotherms enable extracting the values of the BET surface area S_{BET}, the micropore volume V_{HK}, the total pore volume V_T, and the microspore's contribution to the total pore volume V_{HK}/V_T ratio, As shown in **Table 6**. The AN-K-AC sample prepared by physical mixed with KOH exhibits the highest S_{BET} and V_T of 2935 m^2/g and 1.33 cm^3/g, respectively. However, when compared to KOH activation, NaOH activation produced smaller surface areas and lower pore volumes (**Table 7**). The V_{HK}/V_T ratio indicates that the two samples are basically microporous, with the micropore volume accounting for more than 87% of the total pore volume in the case of AN-K-AC and 94 % in the case of AN-N-AC.

Table 7. Textural parameters of the carbonized precursor and the prepared ACs.

Sample	Surface area (m^2/g)		Pore volume (cm^3/g)			V_{HK}/V_T (%)
	S_{BET}	S^a_{mic}	V^b_{Total}	V_{HK}	V_{mes}	
AN-K-AC	2934.60	2110.19	1.33	1.16	0.17	87.21
AN-N-AC	1199.62	1096.85	0.50	0.47	0.03	94.00

a Calculated from the DFT equation applied to the N_2 adsorption isotherms.

b Determined at $P/P_O = 0.90$ in the N_2 adsorption isotherms.

The Density Functional Theory (DFT) method was used to calculate the pore size distributions shown in **Figure 33**. The AN-K-AC sample displays a much desirable pore size distribution with a narrow peak bassed at pore diameter width of 7.5 Å, while the other is a wider peak with its broad shoulder about 21.5 Å, and a tail spread over smaller mesoporous (20–36 Å) region in between these two dominant peaks, the sample demonstrated a significant amount of large micropores (10–20 Å), and this combination is assumed as very favorable por size distribution for supercapacitor application.
In the other hand, AN-N-AC sample showed a distinct peak only at 9 Å, and an extended tail of lower magnitude in the bigger micropore to smaller mesopore regions, As a result, as shown in **Table 7**, KOH activated samples had a total specific mesoporous pore volume of 0.17 cm^3/g, compared to 0.03 cm^3/g for NaOH activated samples.

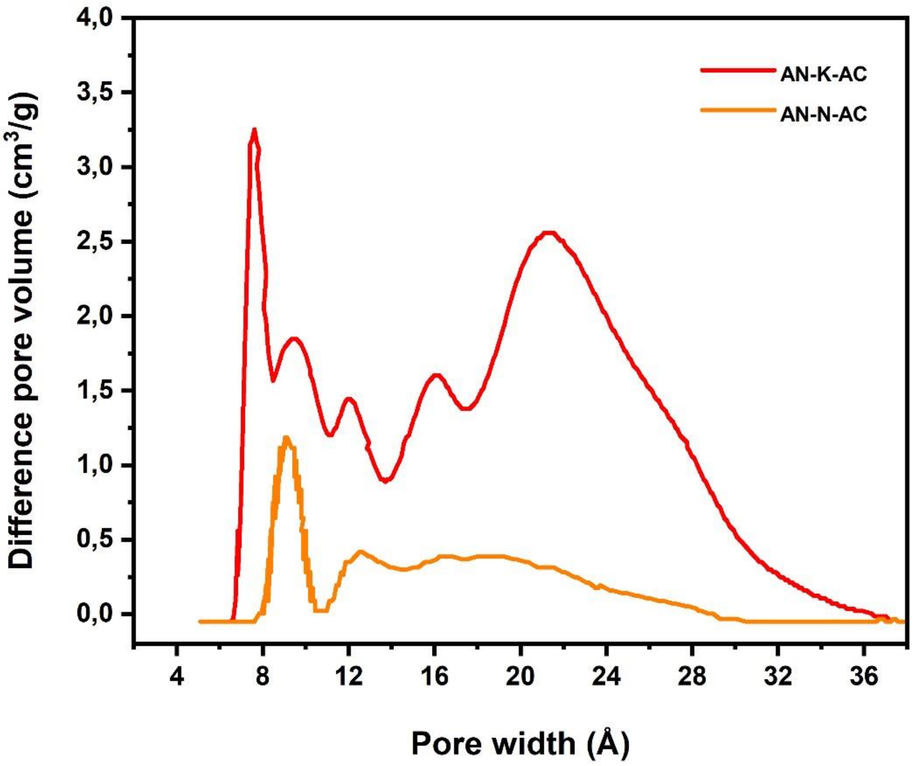

Figure 33. Pore size distribution determined for the prepared ACs using DFT calculations.

Because KOH activated samples have substantially larger total surface area and advantageous pore sizes distribution than NaOH activated samples, AN-K-AC was selected to be investigated as electrodes material for supercapacitor application using aqueous electrolyte in this work.

4.2.3 Electrodes Preparation

Electrodes were prepared by mixing 90% anthracite derived activated carbon AN-K-AC and 10% PTFE binder (60% suspension in water), next the homogenous mixture was dried overnight at 80 °C and later pasted into identical 5 mm diameter graphitic discs with a mass loading of 5 mg on each disc. The obtained graphitic electrodes impregnated in 1M H_2SO_4 and 6M KOH electrolytes for two days before electrochemical measurements. Two symmetrical supercapacitor devices (one with 1 M

H_2SO_4 and other with 6 M KOH) were assembled by sandwiching a porous glassy fibrous separator between two prepared graphitic electrodes.

4.2.4 Electrochemical Measurement

The electrochemical tests were carried out using an assembled symmetric cell including cyclic voltammetry CV, galvanostatic charge-discharge CGD, impedance spectroscopy EIS and stability test (long term charge discharge cycling) using EC-lab VMP system (Biologic) at 25 °C.

Cycling voltammetry tests (CV) were carried out within a voltage range of 0 to 1 V for the assembled cell with H_2SO_4 electrolyte, and within a range of 0 to 0.6 V for the assembled cell with KOH electrolyte. **Figure 34** shows CV curves obtained with the AN-K-AC based symmetric cell using 1 M H_2SO_4 electrolyte (**Figure 34 a**) and 6 M KOH electrolyte (**Figure 34 b**). At scan rate ranging from 5 to 50 mV s^{-1}, all the CV profiles showed a quasi-rectangular voltammograms which characterize the capacitive behaviour. Moreover, the CV profiles obtained with H_2SO_4 electrolyte represent larger rectangular shape than that in KOH electrolyte, proving better reversible capacitance and higher rate capability of AN-K-AC in H_2SO_4.

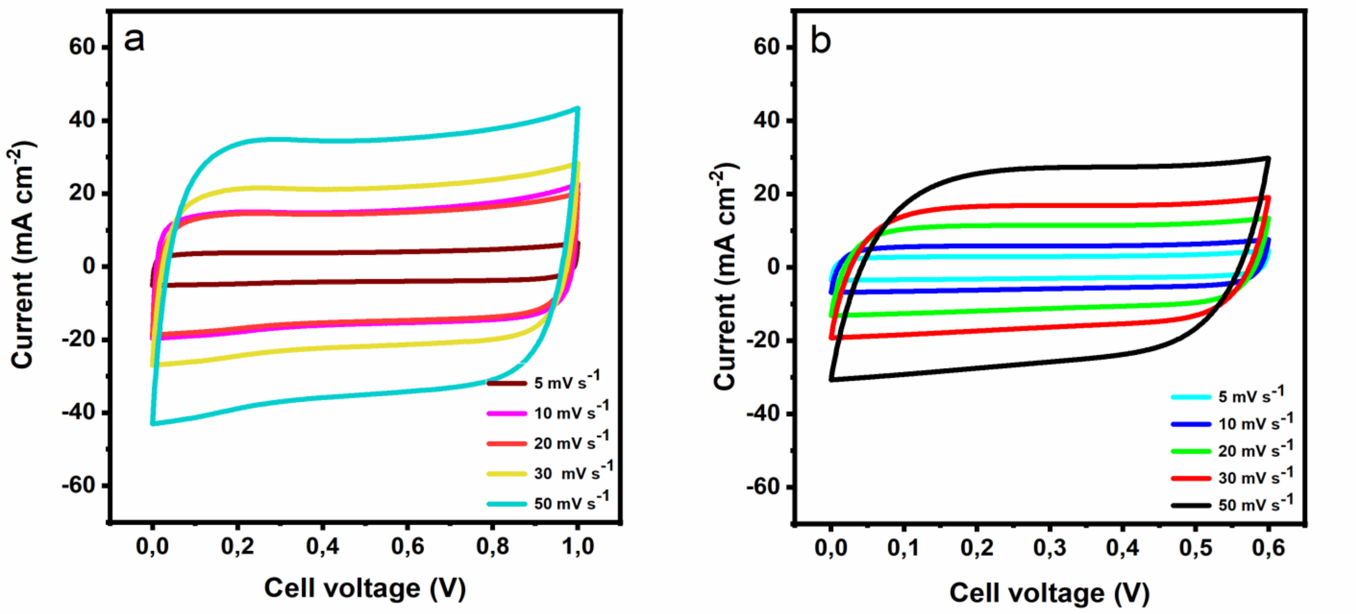

Figure 34. CV curves of AN-K-AC based cell with 1M H_2SO_4 (a) and with 6M KOH (b), at scan rate from 5 to 50 mV s^{-1}

The galvanostatic charge-discharge analysis were carried at different current density from 0.1 A g^{-1} to 3 A g^{-1} as presented in **Figure 35 a-b).** The GCD curves of the assembled cells with both electrolytes H_2SO_4 and KOH showed quasi-triangular shapes without obvious IR drops. Such profile indicate again that the prepared anthracite-derived carbons AN-K-AC behave as an ideal electrochemical double-layer (EDL) with lower internal resistance due to quick charges transfers and ions diffusion within electrode's pores.

The gravimetric capacitance was calculated from the GCD curves using the Eq. (11) [188, 192]:

$$C_{sp} = I \times dt / m \ dV \quad (11)$$

Where I is the discharge current (A), dV/dt is the slope of the discharge curve, and m is the total mass of the two electrodes (in g).

While he specific energy (E) and power (P) were determined by applying Eq. (12) and (13), respectively

$$E\ (Wh\ kg^{-1}) = 1/2 \times Csp\ (Fg^{-1}) \times \Delta V^2\ (V) \tag{12}$$

$$P(W\ kg^{-1}) = E\ (Wh\ kg^{-1}) / \Delta t\ (s) \tag{13}$$

The cells exhibit a specific capacitances (calculated from the GCD curves at current density of 0.1 A g^{-1}) of 50.3 Fg^{-1} and 38 Fg^{-1}, a maximum energy density of 7 Wh kg^{-1} and 2 Wh kg^{-1} , and a maximum power density ~1.7 kW kg^{-1} and 1.2 kW kg^{-1} using H_2SO_4 and KOH electrolytes, respectively. It should be emphasize that the high-obtained capacitance is associated with the electrode material's large surface area and well developed roporosity [193]. On the other hand, the lower values of capacitance obtained using KOH as compared with H_2SO_4 are, apparently, associated with the nature and the size of the involved cations (H^+ vs K^+). In fact, the larger size of K^+ cations may reduce their mobility as compared with smaller cations H^+. Consequently, resistance to the electrolyte increases as capacitance decreases.

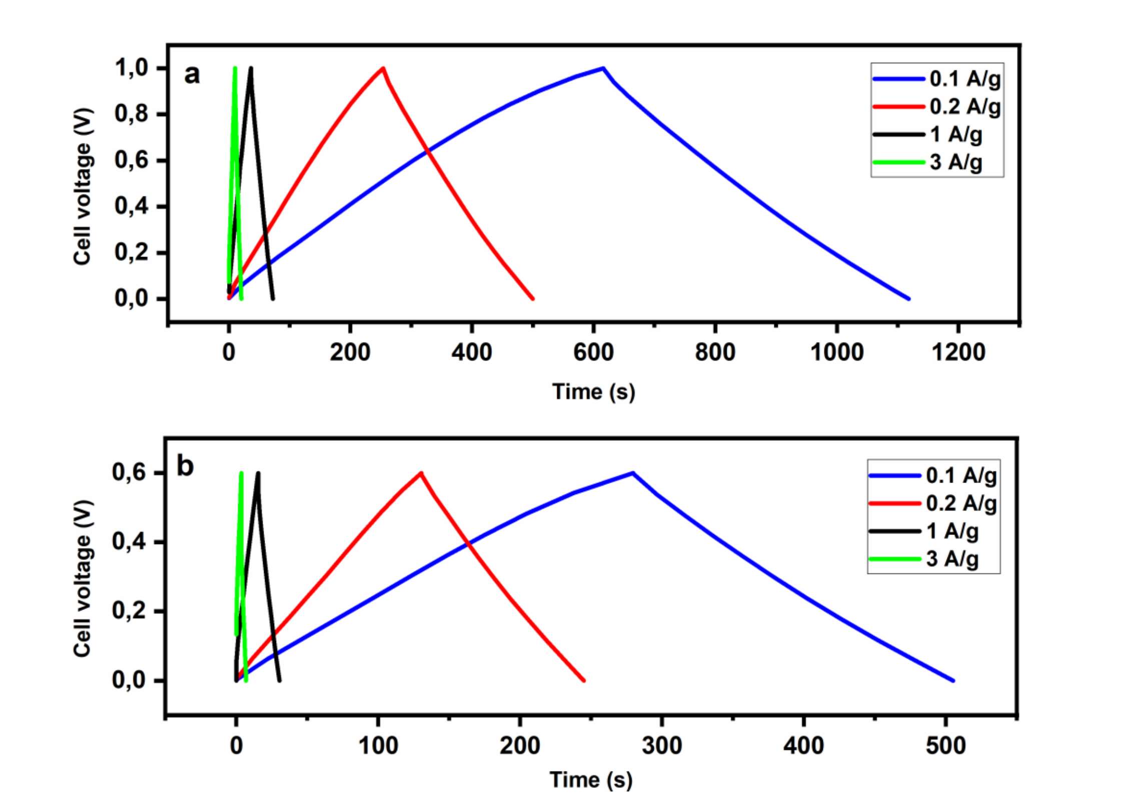

Figure 35. Galvanostatic charge-discharge of AN-K-AC based cells with 1M H_2SO_4 (a) and with 6M KOH (b), at current density from 0.1 to 3 A/ g.

To obtain more insight on the resistance and its dependence on ions diffusion, electrochemical impedance spectroscopy EIS was performed. **Figure 36** shows the obtained Nyquist impedance spectra of the assembled devices at a frequency range from 100 kHz to 10 mHz. Either device with H_2SO_4 or with KOH electrolyte, the Nyquist plot show quasi- vertical line parallel to the imaginary axis at low frequency region, indicating overall an approximately ideal capacitive behavior. Taller line obtained in case of using H_2SO_4 electrolyte than that of KOH indicating higher capacitance. This finding is in agreement with the results obtained in CV and GCD analysis. Also, the obtained ESR is as low as 0.2 and 0.7 Ω cm^2 in H_2SO_4 and KOH electrolyte respectively, confirming the low ion diffusion resistance with better compatibility of the textural properties of AN-K-AC anthracite derived-carbon with H_2SO_4 electrolytes ions nature.

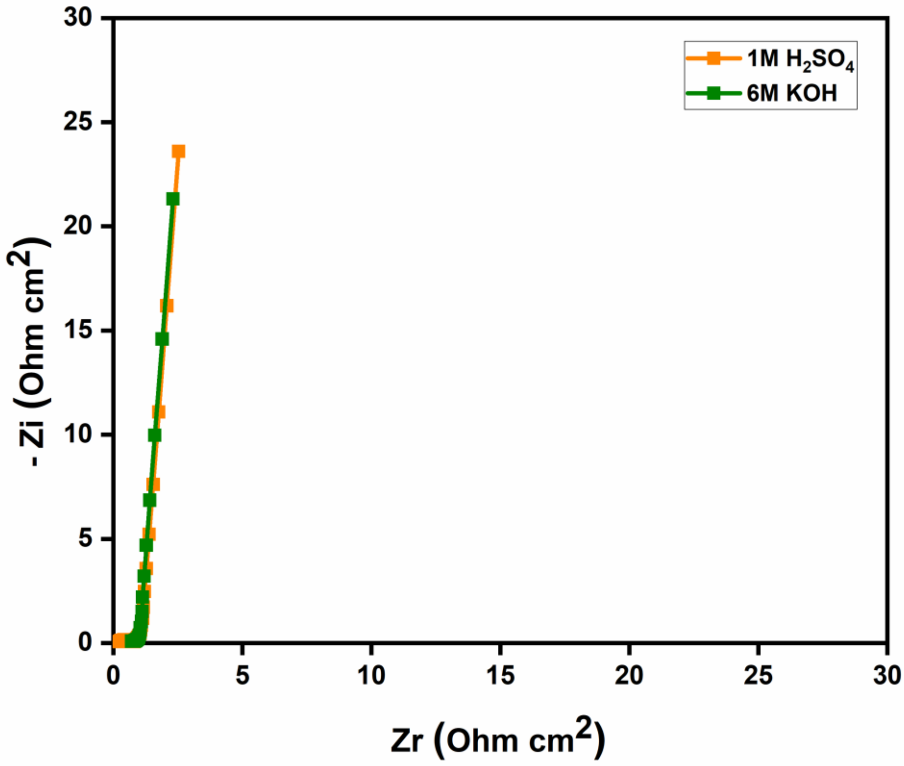

Figure 36. Nyquist plots of the AN-K-AC based cell with 1 M H_2SO_4 (a) and with 6M KOH (b), at frequency range from 1 mHz to 100 kHz.

Furthermore, long-term stability of the devices was investigated. **Figure 37** presents the cyclic performance of both cells through the variation of gravimetric capacitance over 10,000 charge discharge cycle at a constant current density of 1 A g^{-1}. It has been clearly shown that there is almost no significant decreases in the specific capacitance values of the cell assembled with H_2SO_4 electrolyte where the specific capacitance retention remained at almost 99 % in H_2SO_4, while it has decreased to 74 % for the cell assembled with KOH electrolyte. The excellent cyclic stability obtained with the cell with H_2SO_4 is again apparently associated with its appropriate ions size matching pore size distribution of AN-K-AC electrodes materials.

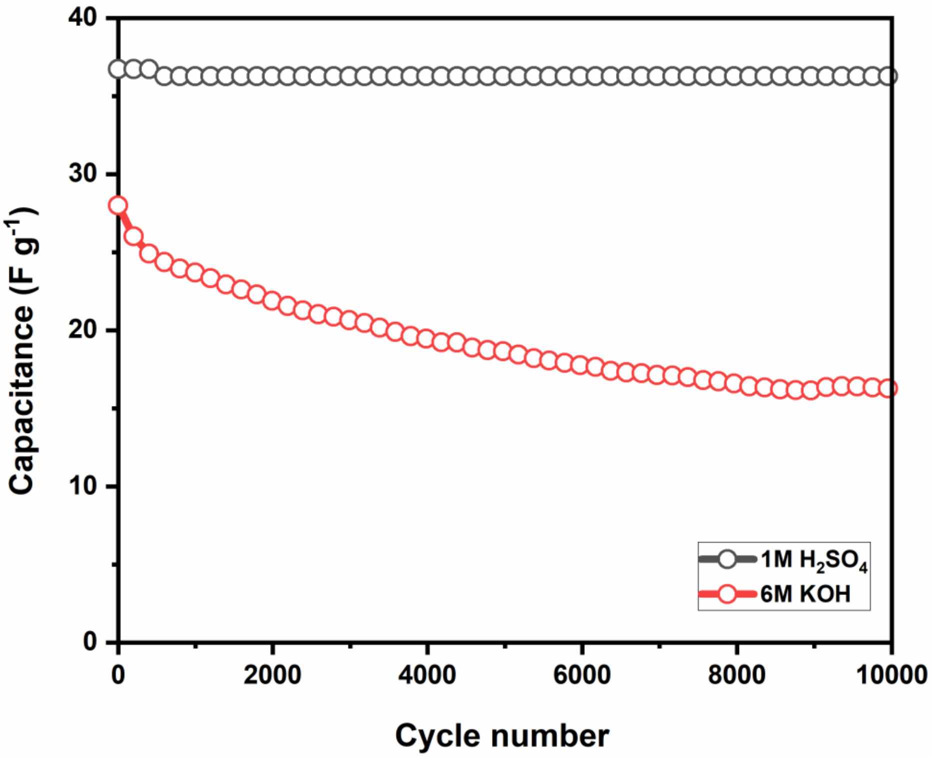

Figure 37. Variation of the gravimetric capacitance with the number of charge discharge cycles of the AN-K-AC based cells whith 1M H_2SO_4 and in 6M KOH, at current density of 1 A g^{-1}.

4.3 Conclusion

ACs prepared from natural anthracite AN-K-AC features high surface area about 2934.60 m^2/g and appropriate micro-mesopores distribution, yielding to promising electrochemical performance. The assembled supercapacitor devices using AN-K-AC as electrodes materials with 1 M H_2SO_4 and 6 KOH aqueous electrolytes yield to interesting values of capacitance reached 50.3 F g^{-1} and 38 F g^{-1} respectively. Moreover, when H_2SO_4 electrolyte was used, a maximum energy density of 7 Wh k g^{-1} and maximum power density of ~1.7 kW kg^{-1} were achieved as well as excellent capacitance retention of about 99 % after 10,000 cycles. Such result may help valorisation of the abundant low-cost anthracite as raw material for promising AC candidate for supercapacitor application.

CHAPTER 5: CIRCUMNEUTRAL CONCENTRATED AMMONIUM ACETATE SOLUTION AS WATER-IN-SALT ELECTROLYTE FOR ARGAN SHELL- DERIVED CARBON BASED SUPERCAPACITOR

Energy density : 5.9 Wh kg^{-1} (−10 °C), 9.2 Wh kg^{-1}(RT), and 15.6 Wh kg^{-1} (80 °C)

Power density: 3.7 kW kg^{-1} (−10 °C), 6.7 kW kg^{-1} (RT), and 10.4 kW kg^{-1} (80 °C)

Equivalent series resistance: 8 Ωcm^2 (−10 °C), 4.5 Ωcm^2 (RT), and 2.9 Ω cm^2 (80 °C)

Capacitance Retention (long term cyclability test): with coulombic efficiencies approaching 100%

Abstract

The exponentially growing market of electrochemical ESDs requires substitution of flammable, volatile, and toxic electrolytes. The use of Water in salt solutions (WiSE) regarded as green electrolyte might be of interest thanks to an association of key features such as high safety, low cost, wide electrochemical stability, and high ionic conductivity. Here, we report comprehensive chemical-physical study of circumneutral WiSE based on ammonium acetate so as to investigate application in electrochemical energy storage systems, with focus on the effect of pH, density, viscosity, conductivity, and the electrochemical stability window ESW with salt concentration ranging from 1 to 30 mol kg^{-1}. Data are reported and discussed with respect to the structure of the solutions investigated by complemental IR and molecular dynamic study. The study is addressed through the showcase of an asymmetric supercapacitor based on Argan shell-derived carbon electrodes tested at temperatures ranging from -10 to 80 °C.

5.1 Introduction

Today, the increasing demand for electrochemical ESDs pushes towards improving their performance and safety at lower cost and environmental impact. The electrolyte is a key component of ESDs and should address the following requirements: (i) high ionic conductivity, (ii) wide electrochemical stability window (ESW), (iii) high thermal stability, (iv) low cost, and (v) environmental compatibility.

Commercial lithium-ion batteries and electrical double layer capacitors (EDLCs) typically feature electrolytes based on lithium hexafluorophosphate in ethylene carbonate and dimethyl carbonate (LP30) and tetraethylammonium tetrafluoroborate in acetonitrile ($TEABF_4$/ACN), respectively. Table summarizes these electrolyte characteristics. The ionic conductivity (κ) and ESW are 10.8 mS cm^{-1} and 5.7 V for LP30, 56 mS cm^{-1}, and 6.1 V for $TEABF_4$/ACN. Their cost is mainly affected by the salt.

Table 8. Ionic conductivity (κ), electrochemical stability window (ESW) at room temperature and commercial cost of different electrolyte solutions and components used in ESDs.

Electrolyte solution components and composition	**Salt Concentration**	**κ**	**ESW**	**Costs**	**Ref.**
Conventional Organic electrolytes					
Tetraethylammonium tetrafluoroborate in Acetonitrile (ACN/$TEABF_4$)	1 mol/L	56 mS cm^{-1}	6.1 V	3.69$/g[a] 130$/L[b]	[194-196]
Lithium hexafluorophosphate in ethylene carbonate and dimethyl carbonate (LP30) (1.0 M $LiPF_6$ in EC/DMC=50/50 v/v)	1 mol/L	10.8 mS cm^{-1}	5.7 V	982 $/L[c]	[197-199]
Ionic liquids					
1-Ethyl-3-methylimidazolium bis-(trifluoromethylsulfonyl)-imide (EMITFSI)	3.9 mol/L	9 mS cm^{-1}	4.5 V	198 $/g[b]	[200]
1-Butyl-1-methylpyrrolidinium bis(trifluoromethanesulfonyl)imide ($PYR_{14}TFSI$)	6 mol/L	2.8 mS cm^{-1}	6.6V	22 $/g[b]	[194]
Salts used in WiSE					
Lithium Bis(trifluoromethane)sulfonimide (LiTFSI)	21 mol/kg	10 mS cm^{-1}	3 V	7 $/g[b]	[201]
Potassium acetate (KOAC)	30 mol/kg	25 mS cm^{-1}	3.2 V	0.35 $/g	[202]
Lithium acetate (LiOC) + KOAC	32mol/kg KOAc 8mol/kg LiOAc	5.3 mS cm^{-1}	2.7 V	0.9 $/g + 0.35 $/g	[117]
Sodium perchlorate	17 mol/kg	64 mS cm^{-1}	2.8V	0.33$/g	[203]

[a] *solvent cost,* [b] *salt cost,* [c]*solution costs from Sigma Aldrich ; * using different electrodes*

Novel alternative electrolytes have been proposed and the main achievements have been excellently reviewed in the literature [197, 204, 205]. Ionic liquids are an interesting class of organic electrolytes, indeed besides their good ionic conductivity and electrochemical stability, they present important advantages associated with low vapor pressure and flammability, that are key requisites to design safe ESDs. However, they cannot be considered as totally green and their toxicity has been reported as an issue for the disposal of end-of-life devices [206]. In addition, their high cost still represents a limit to larger exploitation in batteries or SC_S. As an example, EMITFSI shows a conductivity of 9 mS

cm^{-1} and an ESW of 4.5 V, while for $PYR_{14}TFSI$ the conductivity is 2.8 mS cm^{-1} and the ESW is 6.6 V. Their cost is more than 5 times higher than that of $TEABF_4$/ACN and LP30 (**Table 8**). Hence, the use of aqueous electrolytes offers a promising opportunity to design cheap and safer devices as compared to organic electrolytes because of their non-flammability, low cost, and environmental friendliness. However, due to water splitting conventional aqueous electrolytes place an intrinsic limitation on the ESD, and mainly EDLC, practical cell voltage.

A major breakthrough in electrolytic materials was achieved only a few years ago by increasing the salt concentration in appropriate salt-solvent combinations [207]. The so-called "water in salt electrolytes" (WiSE) are obtained with aqueous solutions containing salt to water volume or mass ratio higher than 1 [201]. Thanks to their molecular structure and water-to-ion interactions, WiSE have been demonstrated to reach unexpectedly wide ESW, beyond the thermodynamic stability limit of water. Therefore, WiSE are receiving considerable attention as safe electrolytes for batteries and SC_S [201, 203, 208]. The main WiSE investigated for batteries are based on fluorinated imide-based salts, usually lithium bis (trifluoromethane)-sulfonimide (LiTFSI). Suo et al., were the first to report about a WiSE based on a 21 mol kg^{-1} LiTFSI water system capable of reaching an ESW of 3 V and a conductivity of 10 mS cm^{-1} (**Table 8**) [201]. Since then, the interest in WiSE for lithium-ion batteries and SC_S has been growing [203, 208-210]. Although significant improvements were achieved with imide-based WiSE systems, several economic and environmental challenges are still ahead as pointed out by Lukatskaya et al. for LiTFSI [117]. Furthermore, the limited geographical distribution of lithium deposits in the earth's crust, relative to sodium (Na) and potassium (K) deposits, raises another concern associated with the amount of lithium salt needed for WiSE electrolytes [117]. In attempt to lower the amount of lithium salts, binary salts, like eutectic mixtures of lithium and potassium acetates, have been suggested. Mixed WiSE solutions containing 32 mol kg^{-1} potassium acetate – 8 mol kg^{-1} lithium acetate for aqueous batteries featured ESW of 2.7 V and κ of 5.3 mS cm^{-1} [117]. Moreover, EDLCs offer the possibility to us lithium-free WiSE such as potassium acetate–based WiSE, as already reported for an AC-based symmetric supercapacitor that featured excellent cyclic performance under an operating voltage of 2 V [211].

Even though, superconcentrated solutions of acetates are inherently alkaline, due to the hydrolysis reaction of the acetate anion. So far, cheaper sodium perchlorate based WiSE featuring 64.2 mS cm^{-1} and ESW of 2.8 V, has been proposed as a mild neutral electrolyte for 2.3 V EDLCs [203]. Unfortunately, this WiSE cannot be considered as totally green mainly because the perchlorate anion is known as a strong oxidizer [212] .

The present work is devoted to the study of safer and less corrosive circumneutral WiSE obtained with a highly concentrated aqueous solution of ammonium acetate (AmAc). This salt features high solubility in water of 1.48 kg L^{-1} and is composed of ions that derive from a weak base and a weak acid with similar pKa and pKb values. Such a particular characteristic makes AmAc solutions circumneutral. Here, a comprehensive chemical-physical study of AmAc solutions with concentrations ranging from 1 to 30 mol kg^{-1} is reported and discussed. Specifically, the trends of pH, density, viscosity, conductivity, and ESW with AmAc concentration will be discussed in terms of solution structure by complementary IR spectroscopy and molecular dynamics (MD) studies. The feasibility of the use of AmAc WiSE in electrochemical ESDs will be demonstrated through a showcase of SC_S using Argan-shell derived carbon electrodes and AmAc 26.4 mol kg^{-1} electrolyte.

5.2 Materials and Methods

The aqueous solutions of ammonium acetate water in salt AmAc WiSE electrolyte of different molality ranging from 1 to 30 mol/kg investigated in chapter 5 were prepared from ammonium acetate (EMSURE, 98% purity). Where, the pH, density, viscosity, conductivity, and the molecular dynamic (MD) simulation of those solutions were investigated.The pH was measured directly by pH M210 Standard pH meter MeterLab. The density of the solutions was obtained by weighting exact volumes of solution (100µL) measured with a P200 micropipette. Thus, the density determined through the relationship:

$$d = m/v \tag{14}$$

The viscosity of the solutions was obtained by a Viscoclock SI Analytics bubble viscometer. Which measures the time required for the solution flow to pass between two menisci. When the densities of the analyzed solutions approximated to a constant, their viscosity was calculated easily by relating it to the tabulated viscosity and the flow times of the pure solvent, using the formula:

$$\eta_s / \eta_0 = t_s / t_0 \tag{15}$$

Where η_s is the viscosity of the solution, η_0 is the solvent's tabulated viscosity, t_s the solution's flow time, and t_0 is the solvent's flow time in that instrument.

The conductivity of various solutions of AmAc at different temperature was measured directly with a CDM210 conductivity meter electrode MeterLab.

5.2.1 Ammonium Acetate WiSE Characteristics

Ammonium acetate (98% purity) was purchased from EMSURE. The pH of the aqueous solutions was measured by a pHM210 Standard pHmeter MeterLab. The density of the solutions was obtained by weighting exact volumes of solution (100µL) measured with a P200 micropipette. The viscosity of the solutions was obtained by a Viscoclock SI Analytics bubble viscometer. ATR (Attenuated Total Reflection) spectra of liquid aqueous solutions were carried out with an FTIR Brucker Alpha spectrometer equipped with an ATR head. The limited length of the optical path in the sample eliminated the problem of the strong attenuation of the infrared signal by highly absorbent media such as the aqueous solutions. The ionic conductivity was measured with a CDM210 conductivity meter electrode MeterLab. The solutions were thermostated in a cryostat bath at different temperatures.

5.2.2 Molecular Dynamics (MD) Simulations

Setting molecular dynamics (MD) simulations. To investigate the behavior of AmAc solutions at the atomistic level, MD simulations were carried out. Boxes with different AmAc/H_2O ratios (corresponding with the experimental WiSE concentrations investigated in this work) were built. The FF14SB force field was used to model acetate anions and ammonium cations [213] while water molecules were simulated by using the TIP5P water model [214]. Minimization and equilibration. About 5000 steps of steepest descent minimization, followed by additional 5000 steps of conjugate gradient minimization were performed with PMEMD [215]. The minimized structure was considered for a three step equilibration protocol. Particle Mesh Ewald summation was used throughout and H-atoms were considered by the SHAKE algorithm [215]. A time step of 2 fs was applied in all MD runs. Individual equilibration steps included (i) 50 ps of heating to 298 K within an NVT ensemble and temperature coupling according to Berendsen. (ii) 50 ps of equilibration MD at 298 K to switch from NVT to NPT and adjust the simulation box. Isotropic position scaling was used at default conditions. (iii) 400 ps of continued equilibration MD at 298 K for an NPT ensemble switching to temperature coupling according to Andersen.

MD simulation was carried out for the equilibrated system using PMEMD [215] Simulation conditions were identical to the final equilibrium step (iii). Overall sampling time was 100 ns.

Snapshot structures were saved into individual trajectory files every 1000 time steps, i.e. every 2 ps of molecular dynamics.

Trajectories obtained from MD simulations were post-processed using CPPTRAJ [215, 216]. For each simulated box, the density of the solution, the diffusion constants of water and ions, and the radial distribution function g(r) of acetate and ammonium ions were calculated.

5.2.3 Supercapacitor Electrode Preparation

The supercapacitor electrode was obtained using ARG-AC and polytetrafuoroethylene (PTFE) as binder (60% suspension in water), as well as multi-walled carbon nanotubes MW-CNT in an 80/10/10 weight ratio, respectively, and dried at 120 °C overnight. Finally, an amount of 6.5 mg of this mixture was pressed onto a titanium grid disk of 8 mm diameter to prepare electrodes that were subsequently dried.

5.2.4 Electrochemical Measurements

All the electrochemical measurements were performed by a Bio-Logic VSP300 potentiostat/galvanostat. The ESW was evaluated by voltammetric measurements (LSV, Linear Sweep Voltammetry). The working electrode was a glassy carbon electrode (0.07 cm^{-2}), a titanium grid (1 cm^2), or an aluminum foil (1 cm^2). Metal electrodes were used as received. The reference electrode was a saturated calomel electrode (SCE). The counter electrode was a Pt wire.

The supercapacitor was assembled by coupling two identical electrodes impregnated with a 26.4 mol kg^{-1}. AmAc electrolyte for 48 h before the electrochemical measurements using a glass fiber filter (Whatman) as a separator. The electrochemical performance of the supercapacitor was evaluated by a two-electrode setup. Cyclic voltammetry (CV), galvanostatic charge-discharge (GCD), and Electrochemical Impedance Spectroscopy (EIS) of the cell were performed at room temperature, −10 °C and 80 °C.

The supercapacitor specific capacitance (C_{sp}) was calculated from GCD curves using the following Eq.16 [217, 218].

$$C_{sp} = \frac{I \times dt}{m \ dV} \tag{16}$$

Where I is the discharge current (A), dV/dt is the slope of the discharge curve, and m is the total mass of the two electrodes (in g).

The maximum specific energy (E_{max}) and power (P_{max}) were determined by applying Eq. (17) and (18), respectively[28,29]:

$$E_{max}\,(\mathrm{Wh\ kg^{-1}}) = \frac{Csp(Fg^{-1}) \times {V_{max}}^{2}(V)}{2 \times 3.6} \qquad (17)$$

$$P_{max}\,(\mathrm{W\ kg^{-1}}) = \frac{1}{4}\ \frac{{V_{max}}^{2}(V)}{ESR\ (\Omega) \times m(kg)} \qquad (18)$$

where V_{max} is the maximum cell voltage and ESR is the cell equivalent series evaluated by the ohmic drop (ΔV) measured at the beginning of discharge (eq. 19). Given that the same current was used for the charge and discharge,

$$ESR = \frac{1}{2}\,\Delta V/I \qquad (19)$$

Practical specific energy (E) and power (P) delivered at different current densities were evaluated by the analyses of the discharge profiles by Eq. (20) and (21)

$$E\,(\mathrm{Wh\ kg^{-1}}) = I \int V dt/(3.6\, m), \qquad (20)$$

$$P = 3.6\ E/\Delta t, \qquad (21)$$

where Δt is the discharge time in seconds.

5.3 Results and Discussion

5.3.1 Physicochemical Studies of Ammonium Acetate Wise

Table 9 reports the acronym of the ammonium acetate solutions that were investigated with the corresponding values of molality, salt to solvent molar ratio, molarity, and density. We investigated solutions containing ammonium acetate (AmAc), with a molality of 1, 5, 10, 15, 20, 26.4 and 30 mol kg^{-1}. It is worth nothing that at the highest concentration only two moles of water are sheared every ion of ammonia $NH4^+$. Table 2 also reports the values of the density (d) that have been calculated under the hypothesis that the molar volumes of AmAc and water are additives Eq. (22). The experimental results differ only by less than 0.1% from the calculated values.

$$\mathbf{d}_{\mathbf{calculated}} = \frac{m_{AmAc} + m_{H_2O}}{V_{AmAc} + V_{H_2O}} \tag{22}$$

Where m_{AmAc}, m_{H_2O}, V_{AmAc} and V_{H2O} are mass and volume of ammonium acetate and water.
Using the definition of the salt molality (C_{AmAc}) and density (d_{AmAc} = 1.17 kg L^{-1}).

Table 9. Acronym of the AmAc solutions investigated with the corresponding values of molality, salt to solvent molar ratio, molarity, density calculated by Eq. (20), experimental and from MD simulations, and excess molar volume (EV).

Code	**Molality (mol/kg)**	**AmAc:H₂O Molar ratio**	**Molarity (mol/L)**	**Density (kg/L)**			**EV (mL/mol)**
				Calculated	**Exp**	**MD**	
1m	1	1.8:100	0.95	1.010	1.02	1.02	−0.25
5m	5	9:100	3.79	1.042	1.05	1.09	−0.18
10m	10	1.8:10	6,06	1.067	1.07	1.13	−0.07
15m	15	2.7:10	7.5	1.084	1.08	1.15	0.01
20m	20	3.6:10	8.58	1.096	1.09	1.16	0.16
26.4m	26.4	4.8:10	9.57	1.107	1.10	1.17	0.23
30m	30	5.4:10	10.10	1.112	1.11	1.18	0.24

To highlight this small difference, we evaluated the excess molar volume EV (**Table 9**) i.e., the difference between the experimental molar volume of the solution and the value obtained by considering that salt and solvent molar volumes are additives (Eq. (23)):

$$\mathrm{EV} = MM_{AmAc}X_{AmAc}\left(\frac{1}{d_{solution}} - \frac{1}{d_{AmAC}}\right) + MM_{H_2O}X_{H_2O}\left(\frac{1}{d_{solution}} - \frac{1}{d_{H_2O}}\right) \tag{23}$$

Where MM_{AmAc} is the ammonium acetate molar mass (77.08 g mol^{-1}), X_{AmAc} and X_{H2O} are the mole fractions of ammonium acetate and water, $d_{solution}$ is the measured solution density (experimental density values from **Table 9**).

For concentrations lower than 10 m, EV is slightly negative, therefore indicating that a weak volume contraction takes place during the dissolution of AmAc in water. On the contrary, when the concentration rises above 10 m, EV increases up to 0.23 mL at 26.4 m. This relatively positive volume change can be explained by strong ionic and molecular interactions of AmAc ions and water molecules. Specifically, volume expansion could be related to the directional character of hydrogen bonding [219].

Given that our aim was to propose a neutral WiSE, we checked the pH of the different solutions within the concentration range from 1 m to 30 m (**Figure 38.a**) AmAc is composed of weak acidic and base ions that feature the same base and acid constants. Therefore, as demonstrated bellow the pH of ammonium acetate solutions should not change with the salt concentration and be equal to 7:

The salt CH_3COONH_4 (AmAc) is composed by weak acidic and base ions that in water give the following equilibrium

$$CH_3COO^- + NH_4^+ + H_2O \leftrightarrow CH_3COOH + NH_4OH \quad (24)$$

with the equilibrium constant

$$Keq = [CH_3COOH]\,[NH_4OH] \,/\, [CH_3COO^-]\,[NH_4^+] \quad (25)$$

The acid constant of the acetic acid is

$$Ka = [CH_3COO^-][H^+] \,/\, [CH_3COOH] = 1.75 \times 10^{-5} \quad \text{(at room temperature)} \quad (26)$$

The base constant of ammonium hydroxide is

$$Kb = [NH_4^+][OH^-] / [NH_4OH] = 1.74 \times 10^{-5} \quad \text{(at room temperature)} \quad (27)$$

By combining eqs 24, 25, and 26, Keq can be rewritten as:

$$Keq = \frac{([CH_3COO^-][H^+]\,/Ka)([NH_4^+][OH^-]\,/Kb\,)}{[CH_3COO^-]\,[NH_4^+]} = \frac{[H^+][OH^-]}{Kakb} = \frac{kw}{kakb} \quad (28)$$

From the stoichiometry of ammonium acetate :

$[CH_3COO^-]=[NH_4^+]$ and $[CH_3COOH] = [NH_4OH]$ (29)

then

$Keq = [CH_3COOH]^2/ [CH_3COO^-]^2= Kw/(KaKb)$ (30)

From the acetic acid dissociation equilibrium (24):

$[CH_3COOH] /[CH_3COO^-] = [H^+]/Ka$ (31)

Rewriting the expression for Keq,

$Keq = ([H^+]/Ka)^2 = Kw/(KaKb)$ (32)

which yields the formula

$[H^+] = \sqrt{(Kw\ Ka/Kb)}$ (33)

i.e. for AmAC

$[H^+] = \sqrt{(10^{-14} \times 1.75 \times 10^{-5}/1.75 \times 10^{-4})} = 10^{-7}$ mol/L

hence, $pH= -\log [H^+] = 7$

Different from what is expected, **Figure 38.a** shows that the pH values change from almost neutral (1 m solution) to slightly basic along with the increase of the concentration. This is apparently attributed to the decrease of the proton activity.

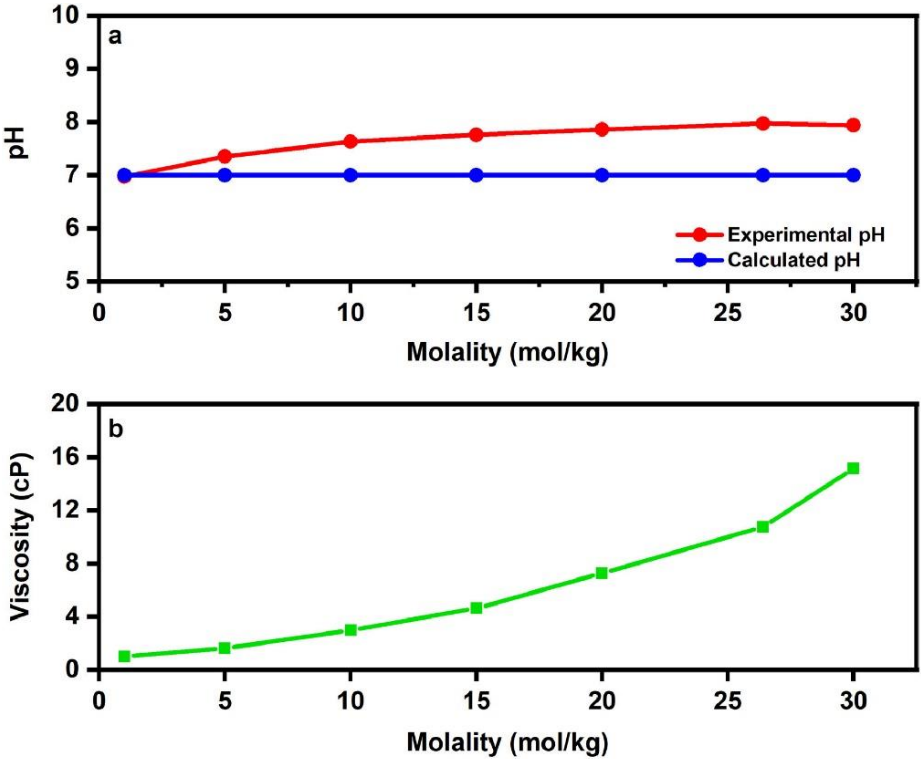

Figure 38.(a) pH and (b) viscosity of AmAc solutions with different molality at room temperature.

The viscosity of the solution increases almost exponentially with the solution molality, as shown in **Figure 38.b**. This trend deviates from the linear curve expected for the diluted solution (Einstein equation) due to involved ions interactions [220]. The absence of minimum in the curve excludes the so-called "water structure breaking" associated with the solution ionic field. At the opposite, it indicates that ammonium and acetate ions are strongly hydrated and contribute to a sort of molecular order in solution [221, 222].

It is known that Stokes-Einstein relation relates conductivity to viscosity [220]. In turn, ionic conductivity and temperature are usually described by an Arrhenius relation. The latter applies for solutions involving no-cooperative mechanism for ion conduction. Under this condition, the logarithm of the specific conductivity (κ) linearly decreases with the reciprocal of the temperature Eq. (34) [223].

$$\log \kappa = \log A^{-RT} \qquad (34)$$

where A is a constant (according to the collision theory, A is the frequency of collisions in the correct orientation), Ea is the activation energy, R is the universal gas constant and T is the temperature.

Figure 39.a present the Arrhenius conductivity plots of the different solutions. A higher conductivity is achieved at increased temperature, which is due to a decreased viscosity and increased ion mobility. The highest conductivity is obtained with the 5 m solutions, while the 30 m shows the lowest value in the whole temperature range. This finding agrees with the viscosity trends with ammonium acetate concentration discussed above. Note that the conductivity of the most diluted solution (1 m) is in the same order of magnitude as those featured by the most concentrated ones (from 20 m to 30 m). Only the 1 m solution features a clear Arrhenius-like linear plot. When the concentration increases above 1 m, the plots deviate from linearity. This non-Arrhenius behavior has already been reported for ionic liquid electrolytes, and described by the Vogel-Tamman-Fulcher (VTF) Eq. (35)[224]:

$$\kappa = A_0 \exp\left[\frac{-B}{(T-T_0)}\right], \qquad (35)$$

Where T is the absolute temperature, and A_0, B, and T_0 are adjustable parameters. According to the VTF model, ion diffusivity and conductivity are affected by several processes like molecular dissociation and cooperative motions. Particularly, the diffusivity is directly related to fluidity (the reciprocal of viscosity) and decreases with the increase of cooperativity. At the contrary, the molar conductivity is positively affected by cooperative processes [224].

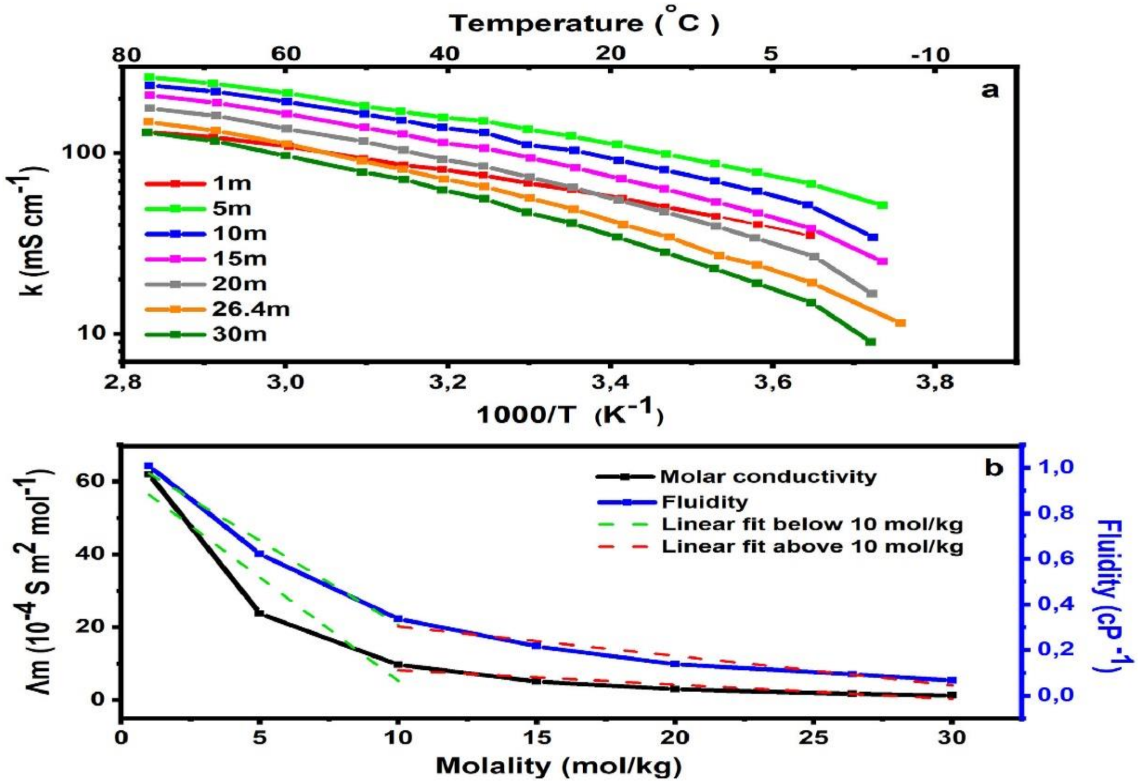

Figure 39. Arrhenius plots build on the basis of the conductivity (κ) at different temperatures of the different solutions, (b) Trend of the molar conductivity (Λm) and fluidity versus molality at room temperature.

Figure 39.b plots the variation of the molar conductivity (Λm)and fluidity versus molality of the AmAc solutions. In the concentration range from 1 m to 10 m, the molar conductivity follows the decrease of fluidity, with almost the same trend. Instead, for concentrations higher than 10 m, this decrease becomes less marked. This suggests that molecular dissociation and cooperative process affects ion conductivity of WiSE.

5.3.2 Molecular Dynamics (MD) Simulations and Fourier Transform Infrared FTIR

The structure of the solutions was investigated using MD simulations. MD trajectories were used to calculate the solution densities as a function of the solution molality. (**Table 10**). The computed and experimental densities present the same trend with a higher increase in density values at lower concentrations.

The diffusion constant D of water, acetate anion, and ammonium cation were calculated using the Einstein relation, on the calculated MD trajectories (as implemented in Amber [215]).

$$2nD = \frac{MSD}{t}, \tag{36}$$

Where n is the number of dimensions, MSD is the mean square displacement. Salt concentration influences the diffusion constant of water. Increasing the salt concentration, the water molecules move slower due to their interactions with ions **(Table 10 and Figure 40).** This is the consequence of increased interaction between water and AmAc, which is also reflected by the contraction of the system volume or higher density. Note also, the decreased ion mobility when molality increases, in agreement with the molar conductivity data reported in **Figure 39.b**. To have an atomistic insight into the structure of the mixtures, atomic radial distribution functions (g(r)) were calculated. In **Figure. 41** g(r) functions for the 1 m and 30 m solutions are reported. The Figure shows the cation-water, cation-cation and cation-anion and the anion-water, anion-cation and anion-anion radial distribution functions. Ammonium and acetate ions induce long-range electrostatic interactions in the mixture that goes from a "ion in water" behavior (1 m) to a "ionic liquid-like" behavior (30 m). Furthermore, for the 30 m solution, the ammonium and the acetate are strongly hydrated as supposed by the absence of minimum in the curve of **Figure 38.b** that excludes a "structure breaking" effect of ions in the solution. Hence, MD simulations clearly support the "structure effect" of ions suggested by the viscosity experimental data.

Table 10. Diffusion constants (D) for H_2O, acetate (AcO^-) and ammonium ($NH4^+$) from MD simulations of the AmAc solutions.

Solution Code	AmAc:H_2O Molar ratio	D (10^5, cm^2 s^{-1})		
		H_2O	AcO^-	NH_4^+
1 m	1.8:100	1.98	1.08	1.07
5 m	9:100	1.17	0.27	0.38
10 m	1.8:10	0.60	0.13	0.17
15 m	2.7:10	0.37	0.08	0.08
20 m	3.6:10	0.23	0.02	0.04
26.4 m	4.8:10	0.17	0.02	0.02
30 m	5.4:10	0.11	0.01	0.02

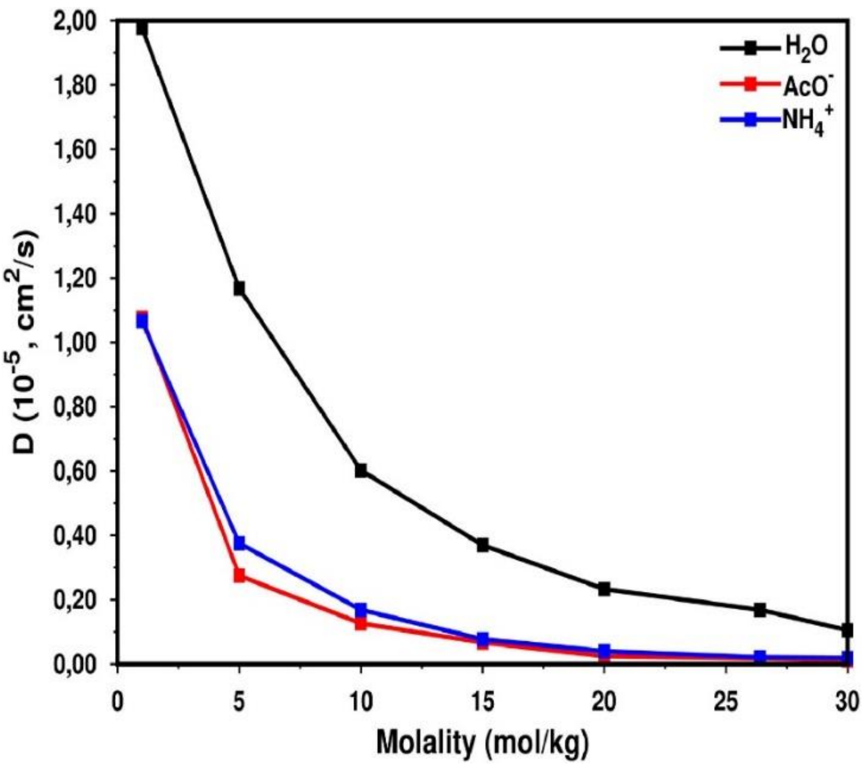

Figure 40. Trend of the diffusion constants of H2O, AcO- and NH4+ vs. molality.

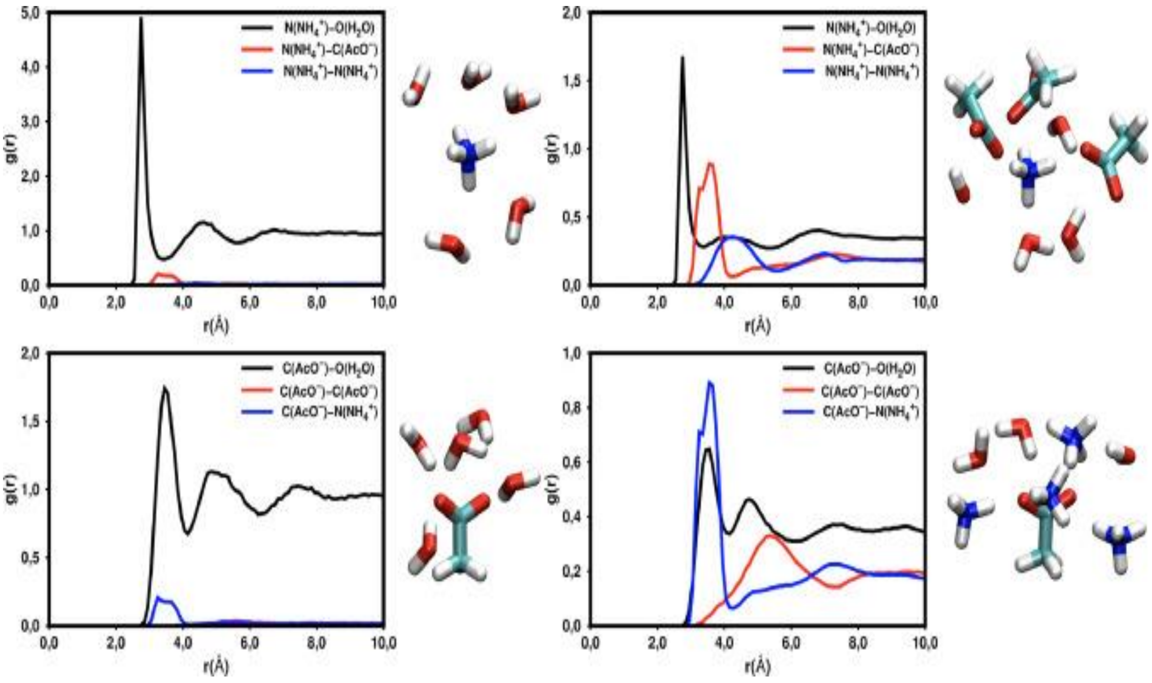

Figure 41. Radial distribution function for a 1 m mixture (left) and 30 m mixture (right) centered on ammonium cation (top) and acetate anion (bottom). A representative cluster structure is reported.

The FTIR characterization of the solutions was carried out to evaluate specific interactions between ions and water molecules. **Figure 42** shows the superimposed IR spectra of the solutions and shows a clear trend in the evolution of the signals. Typical vibrations associated with water are the stretching of the OH bond in the area between 3000 and 3200 cm^{-1}. This region is shared with the stretching of the undissociated acetic acid present in solution. The bending of the HOH angle is around 1640 cm^{-1}. These peaks strongly characterize the typical 1 m aqueous solution and cover the signals referable to the pure salt [225]. On the contrary, the spectrum of the 30 m solution does not reveal interference attributed to the presence of water, looking similar to what is expected for the pure salt. It is important to empathize that, changing solution from 1 m to 30 m, the intensity of the peak associated with HOH bending decreases and becomes insufficiently resolved, thus remaining indistinguishable from the signal relative to the carboxylate ion (symmetrical stretching around 1540 cm^{-1}, asymmetric stretching around at 1400 cm^{-1} for the 30 m solution). The marked change in the shape of the spectrum with the gradual emergence of peaks related to well-defined salt can be interpreted as an important index of the increase in salt activity in solution, combined with a marked decrease in water activity. The peak attributable to O-H stretching alone tends to shift towards lower wavenumbers and change shape from a single very large peak to a system of two peaks located around 3190 and 3012 cm^{-1}. This phenomenon is probably associated with high salt concentration and possible peaks overlapping associated with the stretching of the N-H bond, occurring approximately in the same region as of O-H bonding. Simultaneously also the C = O asymmetrical stretching around 1635 cm^{-1}, and C-O stretching around 1014 cm^{-1}, can be appreciated.

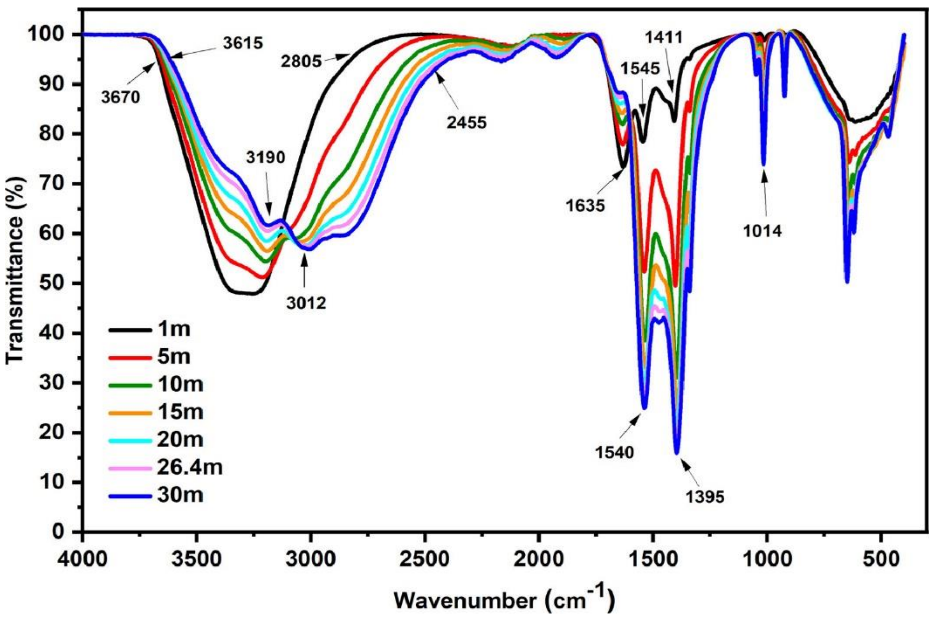

Figure 42. IR spectra superimposed of all the studied solutions.

Overall, a careful analysis of the evolution of the spectra indicates that for all the signals a certain degree of red peak shift to lower wavenumbers occurs as the salt concentration increases. Indeed, the O-H stretching shifted from 3670– 2805 cm^{-1} to 3615–2455 cm^{-1}, N-H bending from 1545 cm^{-1} to 1540 cm^{-1}, and C = O symmetrical stretching from 1411 cm^{-1} to 1395 cm^{-1}. This is apparently associated with the increased hydrogen bond strength involving ions and water molecules yielding to an evolution in the structure of the solution, which is consistent with the aforementioned pH, density, and viscosity trends.

5.3.3 Electrochemical measurement

The electrochemical stability of AmAc solutions was evaluated by linear sweep voltammetry (LSV) carried out at 20 mV s^{-1} in 1 m and 26.4 m solutions at glassy carbon electrode (GC) (**Figure 43.a**). As shown, the cathodic limit for the superconcentrated solution is -1.5 V vs SCE. It is much lower than the limit expected for hydrogen evolution via H^+ reduction in acidic solution (ca, 0.242 V vs SCE). The low cathodic limit of the 26.4 m solution is in line with the low H^+ concentration (pH≈8) and with the low availability of H^+ ions apparently involved in hydrogen bonds with the other ionic species in solution. Considering the anodic limit, it is at around +1.5 V vs SCE. It slightly decreases with the increase of concentration probably due to higher concentration of acetate ions whose oxidation limits anodic stability.

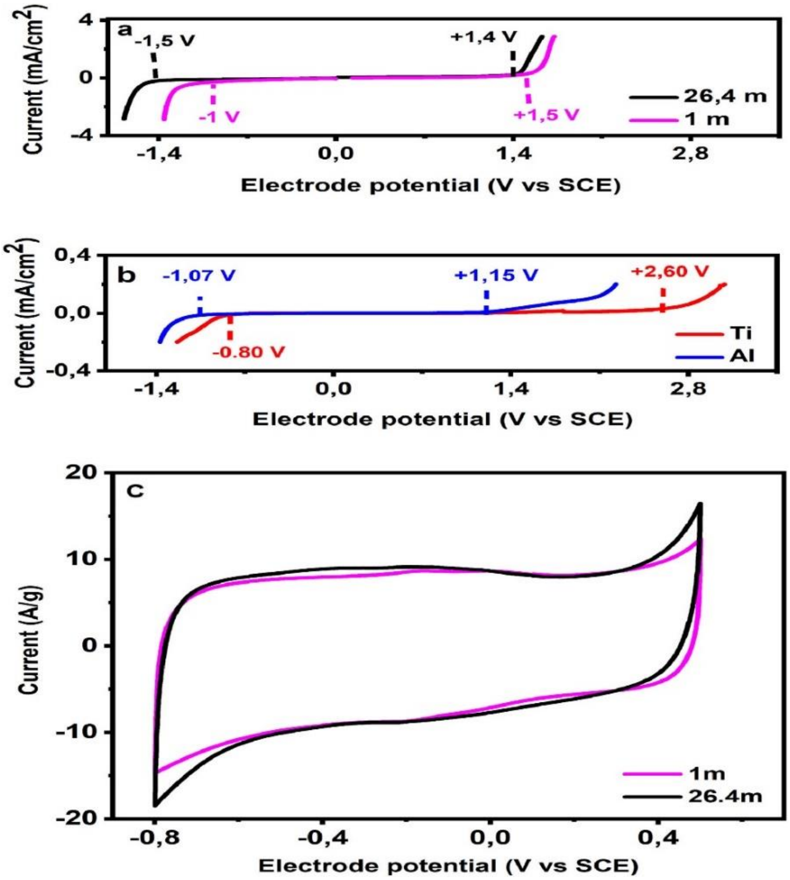

Figure 43. Linear sweep voltammetry at 20 mV-1 carried out with (a) glassy carbon electrode (GC) in 1 m and 26.4 m solutions, (b) CG, titanium grid and aluminum paper in 26.4 m solution, and (c) CG coated by 0.025 mg Argan shells derived carbon (80% ARG-AC, 10% ac acetylene black, 10% Nafion binder) in 1 m and 26.4 m AmAc.

The most interesting aspect is that using WiSEs based on ammonium acetate it is possible to obtain ESW of 2.9 V at GC, higher than 0.4 V compared to typical aqueous solutions, and close to the performance of electrolytes based on organic solvents. In order to evaluate the feasibility of the use of WiSEs in practical devices, ESW was also evaluated at current collectors that are typically used in SC_S and batteries, namely titanium grid and aluminum foil. **Figure 43.b** compares the LSVs carried out at 20 mV s^{-1} in 26.4 m AmAc. With titanium and aluminum, the cathodic limit becomes more positive because these metals promote fast kinetics hydrogen evolution compared to

GC. The cathodic limits are −1.07 V and −0.80 V vs. SCE with aluminum and titanium, respectively. Alike GC, aluminum features an anodic limit of +1.40 V vs. SCE. On the contrary, for titanium it increases to +2.60 V vs SCE. Such a wide anodic range of titanium has been already observed in LiTFSI-based WISE and attributed to the formation of a surface Ti-oxide film that partially passivates the grids and hinders electrolyte decomposition [226, 227]. Accordingly, using titanium and 26.4 m AmAc an outstanding ESW of 3.4 V should be feasible.

GCE was coated by Argan shells derived carbon (ARG-AC) and tested by CV using 1 m and 26.4 m AmAc at 20 mV s^{-1} (**Figure 43.c**). Unexpectedly, when ARG-AC electrodes are used, the ESW width does not change with the increase of AmAc concentration. Furthermore, the ESW is significantly narrower than what was observed with the titanium and GC electrodes. Indeed, with ARG-AC, the ESW is about 1.3 V, with cathodic and anodic limits that can be set at ca. 0.8 V vs SCE and 0.5 V vs SCE, respectively. In fact, the high surface area of the ARG-AC carbon (1937 m^2 g^{-1}) enhances the faradic currents related to electrolyte decomposition and narrows the potential ranges available for the supercapacitor electrode charge. This highlights the importance of the evaluation of electrolyte ESW by adopting the same electrodes that will be exploited in ESDs.

On the other hand, **Figure 43.c** even demonstrates that ARG-AC electrodes feature an excellent capacitive response, both in 1 m and 26.4 m AmAc, that is of ca. 300 F g^{-1}. This value has been extracted from the slope of the plot of the voltammetric specific charge vs. electrode potential.

The electrochemical preliminary tests of SC_S were carried out by a cell with ARG-AC electrodes featuring titanium grids and 26.4 m AmAc WiSE. **Figure 43.c** shows that with ARG-AC electrodes the cathodic stability range is 2 fold wider than the anodic one. Therefore, to fully exploit the WiSE electrochemical stability window, we adopted an asymmetric configuration of supercapacitor with positive to negative electrode mass loading ratio equal to ca 2 [228]. Taking into account the good conductivity response at low and high temperatures of 26.4 m AmAc, we evaluated the supercapacitor performance at room temperature (RT), −10 °C, and 80 °C. **Figure 44** reports the

CV, GCD, EIS, and Ragone plots of the asymmetric supercapacitor. The highest charge cut-off voltage of the asymmetric supercapacitor that enabled high coulombic efficiency (> 99%) was 1.2 V.

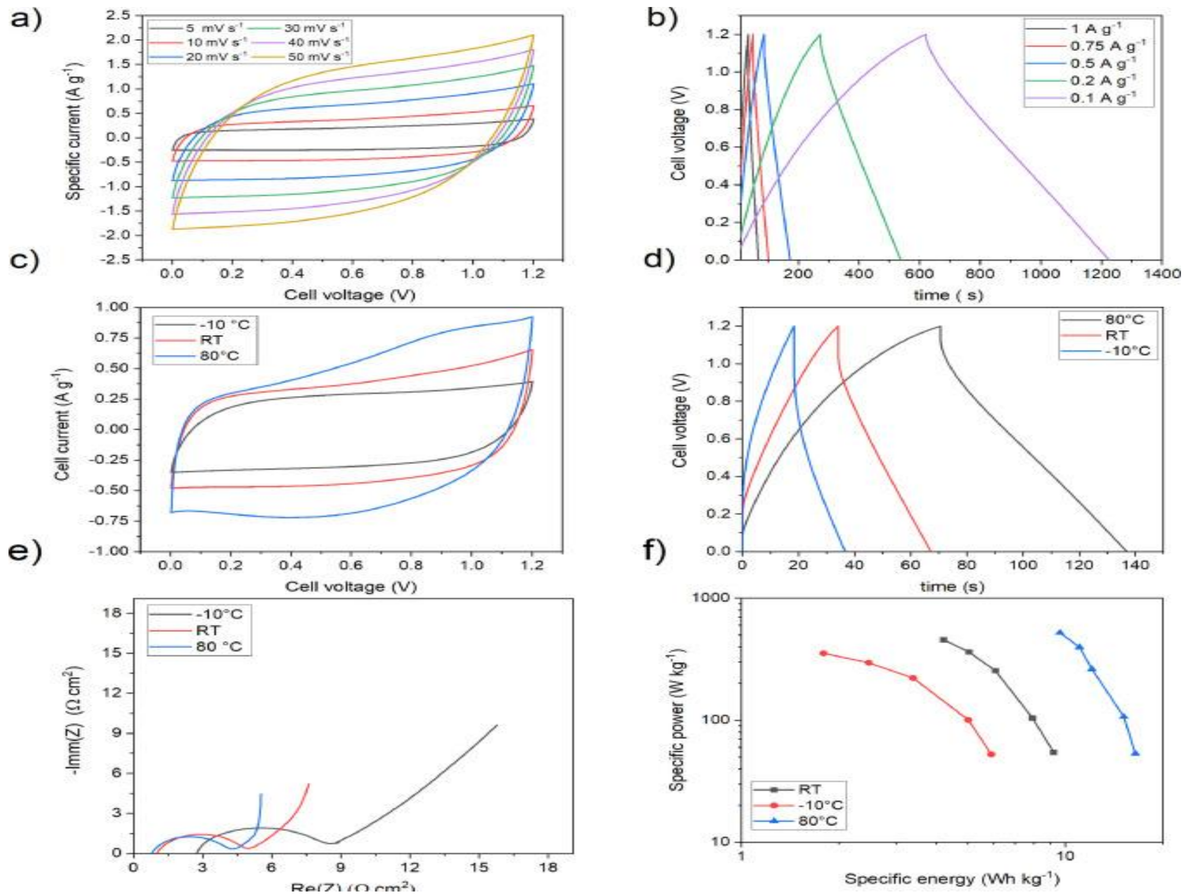

Figure 44. Electrochemical test of the asymmetric supercapacitor assembled with ARG-AC electrodes and 26.4 m AmAc WiSE: (a) CV of the assembled device at scan rate from 5 to 50 mVs-1 and (b) GCD at current densities from 0.1 to 1 Ag-1 (calculated on the basis of positive and negative electrode mass) at room temperature; (c) CV at scan rate 10 mVs-1, (d), GCD at current densities of 0.1 Ag^{-1}, (e) Nyquist plot within a frequency range from 100 KHz to 10 mHz, and (f) Ragone plots of the supercapacitor at different temperatures.

Figure 44.a shows the CVs at RT carried out with increasing the scan rate from 5 to 50 mV s^{-1} the curves exhibit a quasi-rectangular shape profile demonstrating good capacitive behaviors of the electrodes even at the highest scan rate. The GCD was performed at current density ranging from 0.1 A g^{-1} to 1 A g^{-1}. The GCD profiles at room temperature are reported in **Figure 44.b** They exhibit

triangular shape indicating good reversibility and capacitive behavior of the device. Also, all GCD curves show a small ohmic drop, therefore suggesting a low ESR. **Figure 44** (**c–e**) compare the CVs (at 10 mVs^{-1}), the GCD profiles (at 0.1 A g^{-1}) and the Nyquist plots (100 kHz - 10 mHz frequency range) collected at −10 °C, RT and 80 °C. As expected, the CV currents in **Figure 44.c** increase with temperature, due to the higher mobility of AmAc ions. A broad peak appears above 0.9 V at 80 °C. The specific supercapacitor capacitances from the CV curves in **Figure 44.c** were 31 F g^{-1}, 46 F g^{-1} and 71 F g^{-1} at −10 °C, RT and 80 °C. These values correspond to electrode specific capacitance values of 116 F g^{-1}, 173 F g^{-1}, and 266 F g^{-1} of ARG-AC. The highest specific supercapacitor capacitances were obtained at 0.2 A g^{-1} (**Figure 44.d**) and resulted 35 F g^{-1}, 50 F g^{-1} and 98 F g^{-1} at −10 °C, RT and 80 °C. Correspondingly, the maximum energy densities Emax were 7 Wh kg^{-1} (−10 °C), 10 Wh kg^{-1} (RT) and 20 Wh kg^{-1} (80 °C). The ESR values evaluated by the ohmic drop at the beginning of discharge resulted in ca. 8 Ω cm^2 at 10 °C, 4.5 Ω cm^2 at RT, and 2.9 Ω cm^2 at 80 °C. These values well compares with the medium low frequency resistance of the cells shown by the Nyquist plots reported in **Figure 44.e**. It is worth noting the low ESR exhibited by the cells even at the lowest temperature. The plots indicate that the decrease of temperature mainly impacts ion diffusion in the porous electrode architecture (low frequency tail of the Nyquist plots). On the other hand, MD simulation and experimental data reported in the previous sections already indicated that cooperative mechanisms are responsible for AmAc WiSE ion conductivity. In turn, this affects the kinetics of the electrical double layer formation at the electrode/electrolyte interface, especially at the lowest temperatures. From ESR, maximum power densities P_{max} of 3.7 kW kg^{-1} (−10 °C), 6.7 kW kg^{-1} (RT), and 10.4 kW kg^{-1} (80 °C) were measured.

The practical specific energy and power delivered by the supercapacitor at different currents and temperatures are compared in the Ragone plot reported in **Figure 44.f**. The maximum specific energy is delivered at the lowest current, while the maximum power is featured at the highest current. At 0.1 A g^{-1}, the specific energy is 5.9 Wh kg^{-1} (−10 °C), 9.2 Wh kg^{-1}(RT), and 15.6 Wh kg^{-1} (80 °C). At 1 Ag^{-1}, the specific power is 350 W kg^{-1}(−10 °C), 450 W kg^{-1} (RT) and 507 W kg^{-1} (80 °C).

Finally, **Figure 45.a** reports the results of a cycle stability test carried out at different current densities, 0.2 A g^{-1} and 1 A g^{-1} at RT and −10 °C. For a comparison, **Figure 44.b** reports the trend of the capacitance vs. cycle number of an analogous device that was assembled with the diluted electrolyte 1 m AmAc. The two cells featured very good capacitance retention with coulombic efficiencies approaching 100%. Only by the use of the superconcentrated electrolyte, it was possible to operate the cell at −10 °C over a period of four days.

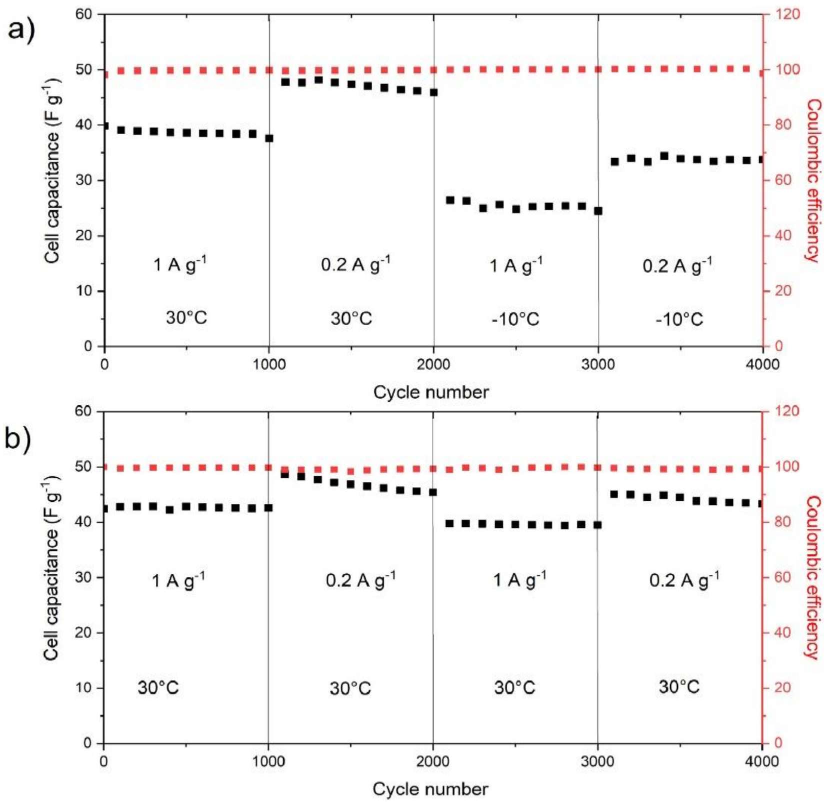

Figure 45. Trend of the capacitance under galvanostatic cycling at 0.2 A g^{-1} and 1 A g^{-1} of (a) the asymmetric supercapacitor with 26.4 m AmAc at RT and −10 °C and (b) of the asymmetric capacitor with 1 m AmAc at RT.

5.4 Conclusion

The low-cost super-concentrated aqueous solutions based on ammonium acetate feature circumneutral pH (pH = 7–8) and ionic conductivity comparable to or higher than typical organic electrolytes. MD simulations confirmed all the experimental results and provided an atomistic picture of the system. The change in the structure of concentrated solutions is due to strong interactions between ions and/or water molecules through the formation of hydrogen bonding that cause an increase in pH values and a decrease in ions mobility.

Ammonium and acetate are strongly hydrated as suggested by the absence of minimum in the curve excluding a "structure breaking" effect of ions in the solution, meaning that there is no destruction in the structure of water by the ionic field, in agreement with the viscosity results. In turn, the presence of cooperative motions is suggested by the conductivity temperature dependence, that follows a non-Arrhenius behavior like ionic-liquid electrolytes. Moreover, the MD simulation suggested. that mixture goes from an "ion in water" (conventional solutions) to an "ionic-liquid-like" (concentrated solutions) behavior. One of the most interesting aspects is that the WiSE based on 26.4 m exhibits an ESW of 2.22 V at Al foil, 2.9 V at GC, and an outstanding value of 3.4 V when Ti grid was used. Despite such interesting results, the ESW evaluated using ARG-AC electrodes was only 1.3 V wide and affected by the high carbon surface area which promoted electrochemical decomposition of the electrolyte. While this finding strongly suggests that ESW is dependent on the kind of electrodes used for the test, it also prevented the development of symmetric SC_S with the high cell voltage expected by the study carried out with GC and metal grids.

On the other hand, the ARG-AC electrodes obtained by pyrolysis and activation of argan shells exhibited an exceptional specific capacitance of 300 Fg^{-1} in the super-concentrated electrolyte. The asymmetric supercapacitor assembled with ARG-AC electrodes and 26.4 m AmAc WiSE was able to operate at 1.2 V, from −10°C to 80 °C with outstanding specific capacitance and low resistance. The asymmetric cell delivered noticeable specific energy at extreme temperatures and ranged from

5.9 Wh kg^{-1} at −10 °C to 15.6 Wh kg^{-1} at 80 °C, values that are competitive with those of commercial SC_S featuring organic electrolyte. Overall, our study suggests that AmAc WiSE deserves consideration as cheap, circumneutral and environmentally friendly alternative electrolytes for designing green energy storage systems.

CHAPTER 6: SUMMARY

Summary

The research activities carried out in this thesis aimed at contribution to local sustainable development through valorization of available local natural resources as feedstock for the production of electrodes for ESDs based on AC. The latter was prepared from Argan shells and natural Anthracite coal as precursors. In the case of Argan shells pyrolysis step was followed by KOH or NaOH chemical activation, while in the case of Anthracite only KOH or NaOH-chemical activation was needed. Several experiments were carried out so as to achieve optimisation of preparation parameters that yield to interesting textural development as indicated by the obtained high specific surface area and the well-developed porosity. At first, the electrochemical performances of the as-selected ACs sample as SC_S electrodes were investigated using H_2SO_4 and KOH aqueous electrolytes. Afterward cheap circumneutral water in salt electrolyte was also explored with the aim to address the safety issue associated with organic electrolytes largely used due of their highest electrochemical stability window even thought their high cost, toxicity and flammability.

The adopted empirical approach for optimization of textural characteristics permitted Argan shells transformation into high added value carbon material for the preparation of SC_S electrodes. The obtained AC showed interesting BET specific surface area of 2251 m^2/g and well-developed micro-mesoporous structure. The resulting carbon-based electrodes enable interesting electrochemical performances, as indicated by a high capacitive response using H_2SO_4 and KOH electrolytes. Hence using 1 M H_2SO_4 and 6 M KOH electrolytes, yield respectively, to interesting values of specific capacitance of 250 F g^{-1} and 192 F g^{-1}, obtained at a current density of 0.1 A g^{-1}. The assembled symmetric devices using H_2SO_4 demonstrated a maximum energy of 8.7 Wh kg^{-1} , maximum power density of kW kg^{-1} , and very low resistances of 0.21 and 0.79 cm^2. Ω Note that interesting capacitance retentions of 94% and 82% after 10,000 GCD cycles were achieved at 1 A g^{-1}, using H_2SO4 and KOH electrolytes respectively.

Similar approach was adopted for the preparation of AC_S using anthracite as precursor and yielding to higher value of BET surface area of about 29345 m^2/g as well as an appropriate micro-mesopore distribution for the selected sample . The assembled symmetric supercapacitor devices using anthracite derived carbon as electrodes material and aqueous electrolytes showed interesting electrochemical performances. Where the capacitance values reached 50.3 F g^{-1} and 38 F g^{-1} at current density of 0.1 A g^{-1}, using 1M H_2SO_4 and 6M KOH electrolytes, respectively. While when H_2SO_4 was used, higher energy density of 7 Wh g^{-1} and power density of 1.7 kW g^{-1} were as well as excellent capacitance retention of nearly 99% after 10,000 cycles obtained.

The achieved electrochemical performance, may help considering such renewable agricultural by products (Argan shell) and abundant low-cost anthracite as a promising candidate precursor for carbon based supercapacitor applications.

With the aim to achieve electrochemical performances comparable to or higher than typical organic electrolytes, a low-cost and low environmental impact concentrated aqueous solutions based on ammonium acetate feature circumneutral (pH = 7–8) were investigated as electrolyte. An increase in pH values and a decrease in ions mobility where the solution's concentration goes from conventional to superconcentrated that attributed apparently to structure modification of more concentrated solutions as result of strong interactions between ions and/or water molecules occurring through the formation of hydrogen bonding. The absence of a minimum in the viscosity curve excluding a "structure breaking" effect of ions in the solution indicates that there is no destruction in the structure of water by the ionic field. The presence of cooperative motions is also suggested by the conductivity temperature dependence, which follows a non-Arrhenius behavior similar to ionic-liquid electrolytes. Moreover, the MD simulation suggested that the mixture goes from an "ion in water" (conventional solutions) to an "ionic-liquid-like" (super-concentrated solutions) behavior.

Note that the Argan shells derived carbon based electrodes exhibited an exceptional specific capacitance of 300 Fg^{-1} in the super-concentrated ammonium acetate water in salt electrolyte AmAc WiSE. The asymmetric supercapacitor assembled with 26.4 m AmAc WiSE was able to operate at 1.2 V, from −10°C to 80 °C with outstanding specific capacitance and low resistance. The cell delivered noticeable specific energy at extreme temperatures ranged from 5.9 Wh kg^{-1} at −10 °C to 15.6 Wh kg^{-1} at 80 °C, values that are competitive with those of commercial SC_S featuring organic electrolyte. Overall, this study suggests that AmAc WiSE deserves consideration as cheap, circumneutral and environmentally friendly alternative electrolytes for designing green energy storage systems. For improving the performances of the supercapacitor based on AmAc WiSE, a promising option to explore is the increase of energy performance through adopting hybrid supercapacitor configuration involving redox or pseudocapacitive electrodes that features faradaic process within the WiSE ESW.

References

[1] R.A. Dias, C.R. Mattos, J.A. Balestieri, The limits of human development and the use of energy and natural resources, Energy Policy, 34 (2006) 1026-1031.
[2] N.S. Rathore, N. Panwar, Renewable energy sources for sustainable development, New India Publishing2007.
[3] N. Panwar, S. Kaushik, S. Kothari, Role of renewable energy sources in environmental protection: A review, Renewable and sustainable energy reviews, 15 (2011) 1513-1524.
[4] International energy agency (IEA) Statistics web site., 2015.
[5] A. El Shahat, A. Keyhani, Sizing high speed micro generators for smart grid systems, Smart Power Grids 2011, Springer2012, pp. 177-234.
[6] K.T. Ponds, A. Arefi, A. Sayigh, G. Ledwich, Aggregator of demand response for renewable integration and customer engagement: Strengths, weaknesses, opportunities, and threats, Energies, 11 (2018) 2391.
[7] W. Cao, Biomass-derived Activated Carbons For Electrical Double Layer Supercapacitors: Performance and Stress Effect, University of Kentucky, 2019.
[8] A. Afif, S.M. Rahman, A.T. Azad, J. Zaini, M.A. Islan, A.K. Azad, Advanced materials and technologies for hybrid supercapacitors for energy storage–A review, Journal of Energy Storage, 25 (2019) 100852.
[9] B. Luo, D. Ye, L. Wang, Recent progress on integrated energy conversion and storage systems, Advanced Science, 4 (2017) 1700104.
[10] A. Gallo, J. Simões-Moreira, H. Costa, M. Santos, E.M. Dos Santos, Energy storage in the energy transition context: A technology review, Renewable and sustainable energy reviews, 65 (2016) 800-822.
[11] M. Dhimish, N. Schofield, Single-switch boost-buck DC-DC converter for industrial fuel cell and photovoltaics applications, International Journal of Hydrogen Energy, (2021).
[12] A.A. Kamel, H. Rezk, M.A. Abdelkareem, Enhancing the operation of fuel cell-photovoltaic-battery-supercapacitor renewable system through a hybrid energy management strategy, International Journal of Hydrogen Energy, 46 (2021) 6061-6075.
[13] P. Thounthong, V. Chunkag, P. Sethakul, S. Sikkabut, S. Pierfederici, B. Davat, Energy management of fuel cell/solar cell/supercapacitor hybrid power source, Journal of power sources, 196 (2011) 313-324.
[14] J.W. Choi, D. Aurbach, Promise and reality of post-lithium-ion batteries with high energy densities, Nature Reviews Materials, 1 (2016) 1-16.
[15] T. Kim, W. Song, D.-Y. Son, L.K. Ono, Y. Qi, Lithium-ion batteries: outlook on present, future, and hybridized technologies, Journal of materials chemistry A, 7 (2019) 2942-2964.
[16] T. Chen, Y. Jin, H. Lv, A. Yang, M. Liu, B. Chen, Y. Xie, Q. Chen, Applications of lithium-ion batteries in grid-scale energy storage systems, Transactions of Tianjin University, 26 (2020) 208-217.
[17] Y. Nishi, Lithium ion secondary batteries; past 10 years and the future, Journal of Power Sources, 100 (2001) 101-106.
[18] B. Smith, R. Wills, A. Cruden, Aqueous Al-ion cells and supercapacitors—A comparison, Energy Reports, 6 (2020) 166-173.
[19] J.R. Miller, P. Simon, Electrochemical capacitors for energy management, Science Magazine, 321 (2008) 651-652.
[20] R. Kötz, M. Carlen, Principles and applications of electrochemical capacitors, Electrochimica acta, 45 (2000) 2483-2498.
[21] B.E. Conway, Electrochemical supercapacitors: scientific fundamentals and technological applications, Springer Science & Business Media2013.

[22] M. Bora, D. Bhattacharjya, B.K. Saikia, Coal-Derived Activated Carbon for Electrochemical Energy Storage: Status on Supercapacitor, Li-Ion Battery, and Li–S Battery Applications, Energy & Fuels, (2021).
[23] P. Simon, Y. Gogotsi, Materials for electrochemical capacitors, Nanoscience and technology: a collection of reviews from Nature journals, (2010) 320-329.
[24] M. Salanne, B. Rotenberg, K. Naoi, K. Kaneko, P.-L. Taberna, C.P. Grey, B. Dunn, P. Simon, Efficient storage mechanisms for building better supercapacitors, Nature Energy, 1 (2016) 1-10.
[25] H.v. Helmholtz, Ueber einige Gesetze der Vertheilung elektrischer Ströme in körperlichen Leitern, mit Anwendung auf die thierisch-elektrischen Versuche (Schluss.), Annalen der Physik, 165 (1853) 353-377.
[26] G. Guoy, Constitution of the electric charge at the surface of an electrolyte, J Physique, 9 (1910) 457-467.
[27] D.C. Grahame, The electrical double layer and the theory of electrocapillarity, Chemical reviews, 41 (1947) 441-501.
[28] O. Stern, The theory of the electrolytic double-layer, Z. Elektrochem, 30 (1924) 1014-1020.
[29] X.-y. Luo, Y. Chen, Y. Mo, A review of charge storage in porous carbon-based supercapacitors, New Carbon Materials, 36 (2021) 49-68.
[30] P. Goel, S. Sundriyal, V. Shrivastav, S. Mishra, D.P. Dubal, K.-H. Kim, A. Deep, Perovskite materials as superior and powerful platforms for energy conversion and storage applications, Nano Energy, 80 (2021) 105552.
[31] Y. Wang, J. Guo, T. Wang, J. Shao, D. Wang, Y.-W. Yang, Mesoporous transition metal oxides for supercapacitors, Nanomaterials, 5 (2015) 1667-1689.
[32] D.P. Dubal, P. Gómez-Romero, G. Korotcenkov, Metal oxides in supercapacitors, Elsevier2017.
[33] K.R. Prasad, N. Munichandraiah, Fabrication and evaluation of 450 F electrochemical redox supercapacitors using inexpensive and high-performance, polyaniline coated, stainless-steel electrodes, Journal of Power Sources, 112 (2002) 443-451.
[34] A. Clemente, S. Panero, E. Spila, B. Scrosati, Solid-state, polymer-based, redox capacitors, Solid State Ionics, 85 (1996) 273-277.
[35] V. Augustyn, P. Simon, B. Dunn, Pseudocapacitive oxide materials for high-rate electrochemical energy storage, Energy & Environmental Science, 7 (2014) 1597-1614.
[36] K. Jost, G. Dion, Y. Gogotsi, Textile energy storage in perspective, Journal of Materials Chemistry A, 2 (2014) 10776-10787.
[37] B.E. Conway, V. Birss, J. Wojtowicz, The role and utilization of pseudocapacitance for energy storage by supercapacitors, Journal of power sources, 66 (1997) 1-14.
[38] D. Majumdar, T. Maiyalagan, Z. Jiang, Recent progress in ruthenium oxide-based composites for supercapacitor applications, ChemElectroChem, 6 (2019) 4343-4372.
[39] A.K. Samantara, S. Ratha, Materials development for Active/Passive components of a supercapacitor: background, present status and future perspective, (2017).
[40] S. Sundriyal, H. Kaur, S.K. Bhardwaj, S. Mishra, K.-H. Kim, A. Deep, Metal-organic frameworks and their composites as efficient electrodes for supercapacitor applications, Coordination Chemistry Reviews, 369 (2018) 15-38.
[41] Y. Wang, Y. Song, Y. Xia, Electrochemical capacitors: mechanism, materials, systems, characterization and applications, Chemical Society Reviews, 45 (2016) 5925-5950.
[42] M. Vangari, T. Pryor, L. Jiang, Supercapacitors: review of materials and fabrication methods, Journal of Energy Engineering, 139 (2013) 72-79.
[43] N. Wu, X. Bai, D. Pan, B. Dong, R. Wei, N. Naik, R.R. Patil, Z. Guo, Recent advances of asymmetric supercapacitors, Advanced Materials Interfaces, 8 (2021) 2001710.
[44] J.H. Kang, Fabrication and characterization of nano carbon-based electrochemical double-layer capacitors, University of Waterloo, 2015.

[45] Q. Cheng, J. Tang, J. Ma, H. Zhang, N. Shinya, L.-C. Qin, Graphene and carbon nanotube composite electrodes for supercapacitors with ultra-high energy density, Physical Chemistry Chemical Physics, 13 (2011) 17615-17624.
[46] J. Rouquerol, D. Avnir, C. Fairbridge, D. Everett, J. Haynes, N. Pernicone, J. Ramsay, K. Sing, K. Unger, Recommendations for the characterization of porous solids (Technical Report), Pure and applied chemistry, 66 (1994) 1739-1758.
[47] L. Wei, G. Yushin, Nanostructured activated carbons from natural precursors for electrical double layer capacitors, Nano Energy, 1 (2012) 552-565.
[48] A.G. Pandolfo, A.F. Hollenkamp, Carbon properties and their role in supercapacitors, Journal of power sources, 157 (2006) 11-27.
[49] A. Stein, Z. Wang, M.A. Fierke, Functionalization of porous carbon materials with designed pore architecture, Advanced Materials, 21 (2009) 265-293.
[50] M. Molina-Sabio, F. Rodrıguez-Reinoso, Role of chemical activation in the development of carbon porosity, Colloids and Surfaces A: Physicochemical and Engineering Aspects, 241 (2004) 15-25.
[51] M.A. Azam, N.S.N. Ramli, N.A.N.M. Nor, T.I.T. Nawi, Recent advances in biomass-derived carbon, mesoporous materials, and transition metal nitrides as new electrode materials for supercapacitor: A short review, International Journal of Energy Research, 45 (2021) 8335-8346.
[52] A.S. Mestre, A.P. Carvalho, Nanoporous carbon synthesis: An old story with exciting new chapters, Porosity; Ghrib, T., Ed.; IntechOpen: London, UK, (2018) 37-68.
[53] K.T. Idris-Hermann, T.T.D. Raoul, D. Giscard, A.S. Gabche, Preparation and characterization of activated carbons from bitter kola (Garcinia kola) nut shells by chemical activation method using H3PO4; KOH and ZnCl2, Chemical Science International Journal, 23 (2018) 1-15.
[54] L. Jiang, L. Sheng, Z. Fan, Biomass-derived carbon materials with structural diversities and their applications in energy storage, Science China Materials, 61 (2018) 133-158.
[55] P.T. Williams, A.R. Reed, Development of activated carbon pore structure via physical and chemical activation of biomass fibre waste, Biomass and Bioenergy, 30 (2006) 144-152.
[56] Ç.d. Şentorun-Shalaby, M.G. Uçak-Astarlıogˇlu, L. Artok, Ç. Sarıcı, Preparation and characterization of activated carbons by one-step steam pyrolysis/activation from apricot stones, Microporous and mesoporous materials, 88 (2006) 126-134.
[57] L. Zhang, Z. Liu, G. Cui, L. Chen, Biomass-derived materials for electrochemical energy storages, Progress in Polymer Science, 43 (2015) 136-164.
[58] R.T. Ayinla, J. Dennis, H. Zaid, Y. Sanusi, F. Usman, L. Adebayo, A review of technical advances of recent palm bio-waste conversion to activated carbon for energy storage, Journal of cleaner production, 229 (2019) 1427-1442.
[59] S. Sundriyal, V. Shrivastav, H.D. Pham, S. Mishra, A. Deep, D.P. Dubal, Advances in bio-waste derived activated carbon for supercapacitors: Trends, challenges and prospective, Resources, Conservation and Recycling, 169 (2021) 105548.
[60] Z. Guo, N. Yan, A.A. Lapkin, Towards circular economy: integration of bio-waste into chemical supply chain, Current Opinion in Chemical Engineering, 26 (2019) 148-156.
[61] T.I. Dugmore, J.H. Clark, J. Bustamante, J.A. Houghton, A.S. Matharu, Valorisation of biowastes for the production of green materials using chemical methods, Chemistry and Chemical Technologies in Waste Valorization, (2017) 73-121.
[62] M.A. Yahya, Z. Al-Qodah, C.Z. Ngah, Agricultural bio-waste materials as potential sustainable precursors used for activated carbon production: A review, Renewable and Sustainable Energy Reviews, 46 (2015) 218-235.
[63] S. Liu, L. Ge, S. Gao, L. Zhuang, Z. Zhu, H. Wang, Activated carbon derived from bio-waste hemp hurd and retted hemp hurd for CO2 adsorption, Composites Communications, 5 (2017) 27-30.

[64] P. Manasa, Z.J. Lei, F. Ran, Biomass waste derived low cost activated carbon from carchorus olitorius (Jute fiber) as sustainable and novel electrode material, Journal of Energy Storage, 30 (2020) 101494.
[65] C.J. Raj, M. Rajesh, R. Manikandan, K.H. Yu, J. Anusha, J.H. Ahn, D.-W. Kim, S.Y. Park, B.C. Kim, High electrochemical capacitor performance of oxygen and nitrogen enriched activated carbon derived from the pyrolysis and activation of squid gladius chitin, Journal of Power Sources, 386 (2018) 66-76.
[66] R. Na, X. Wang, N. Lu, G. Huo, H. Lin, G. Wang, Novel egg white gel polymer electrolyte and a green solid-state supercapacitor derived from the egg and rice waste, Electrochimica Acta, 274 (2018) 316-325.
[67] C. Gong, X. Wang, D. Ma, H. Chen, S. Zhang, Z. Liao, Microporous carbon from a biological waste-stiff silkworm for capacitive energy storage, Electrochimica Acta, 220 (2016) 331-339.
[68] S. Rawal, B. Joshi, Y. Kumar, Synthesis and characterization of activated carbon from the biomass of Saccharum bengalense for electrochemical supercapacitors, Journal of Energy Storage, 20 (2018) 418-426.
[69] X.-L. Su, S.-H. Li, S. Jiang, Z.-K. Peng, X.-X. Guan, X.-C. Zheng, Superior capacitive behavior of porous activated carbon tubes derived from biomass waste-cotonier strobili fibers, Advanced Powder Technology, 29 (2018) 2097-2107.
[70] M. Song, Y. Zhou, X. Ren, J. Wan, Y. Du, G. Wu, F. Ma, Biowaste-based porous carbon for supercapacitor: The influence of preparation processes on structure and performance, Journal of colloid and interface science, 535 (2019) 276-286.
[71] S. Yang, K. Zhang, Converting corncob to activated porous carbon for supercapacitor application, Nanomaterials, 8 (2018) 181.
[72] T. Mitravinda, K. Nanaji, S. Anandan, A. Jyothirmayi, V.S.K. Chakravadhanula, C.S. Sharma, T.N. Rao, Facile synthesis of corn silk derived nanoporous carbon for an improved supercapacitor performance, Journal of the electrochemical society, 165 (2018) A3369.
[73] L. Yin, Y. Chen, X. Zhao, B. Hou, B. Cao, 3-Dimensional hierarchical porous activated carbon derived from coconut fibers with high-rate performance for symmetric supercapacitors, Materials & Design, 111 (2016) 44-50.
[74] M.U. Rani, K. Nanaji, T.N. Rao, A.S. Deshpande, Corn husk derived activated carbon with enhanced electrochemical performance for high-voltage supercapacitors, Journal of Power Sources, 471 (2020) 228387.
[75] N. Sudhan, K. Subramani, M. Karnan, N. Ilayaraja, M. Sathish, Biomass-derived activated porous carbon from rice straw for a high-energy symmetric supercapacitor in aqueous and non-aqueous electrolytes, Energy & Fuels, 31 (2017) 977-985.
[76] Z. Xu, X. Zhang, Y. Liang, H. Lin, S. Zhang, J. Liu, C. Jin, U. Choe, K. Sheng, Green synthesis of nitrogen-doped porous carbon derived from rice straw for high-performance supercapacitor application, Energy & Fuels, 34 (2020) 8966-8976.
[77] H. Jin, S. Wu, T. Li, Y. Bai, X. Wang, H. Zhang, H. Xu, C. Kong, H. Wang, Synthesis of porous carbon nano-onions derived from rice husk for high-performance supercapacitors, Applied Surface Science, 488 (2019) 593-599.
[78] H. Jin, J. Hu, S. Wu, X. Wang, H. Zhang, H. Xu, K. Lian, Three-dimensional interconnected porous graphitic carbon derived from rice straw for high performance supercapacitors, Journal of Power Sources, 384 (2018) 270-277.
[79] N. Parveen, A.I. Al-Jaafari, J.I. Han, Robust cyclic stability and high-rate asymmetric supercapacitor based on orange peel-derived nitrogen-doped porous carbon and intercrossed interlinked urchin-like NiCo2O4@ 3DNF framework, Electrochimica Acta, 293 (2019) 84-96.
[80] G.A. Ali, S. Supriya, K.F. Chong, E.R. Shaaban, H. Algarni, T. Maiyalagan, G. Hegde, Superior supercapacitance behavior of oxygen self-doped carbon nanospheres: a conversion of Allium cepa peel to energy storage system, Biomass Conversion and Biorefinery, 11 (2021) 1311-1323.

[81] M. Karuppannan, Y. Kim, Y.-E. Sung, O.J. Kwon, Nitrogen and sulfur co-doped graphene-like carbon sheets derived from coir pith bio-waste for symmetric supercapacitor applications, Journal of Applied Electrochemistry, 49 (2019) 57-66.
[82] A. Gopalakrishnan, S. Badhulika, Ultrathin graphene-like 2D porous carbon nanosheets and its excellent capacitance retention for supercapacitor, Journal of Industrial and Engineering Chemistry, 68 (2018) 257-266.
[83] K. Lee, L. Shabnam, S.N. Faisal, V.G. Gomes, Aerogel from fruit biowaste produces ultracapacitors with high energy density and stability, Journal of Energy Storage, 27 (2020) 101152.
[84] C. Lu, X.-Z. Qian, H.-Y. Zhu, Y.-X. Hu, Y.-S. Zhang, B.-M. Zhang, L.-B. Kong, M.-C. Liu, 3D hierarchical porous carbon derived from direct carbonization and in-situ chemical activation of potatoes toward high-performance supercapacitors, Materials Research Express, 6 (2019) 115615.
[85] H. Zhao, B. Xing, C. Zhang, G. Huang, Q. Liu, G. Yi, J. Jia, M. Ma, Z. Chen, C. Zhang, Efficient synthesis of nitrogen and oxygen co-doped hierarchical porous carbons derived from soybean meal for high-performance supercapacitors, Journal of Alloys and Compounds, 766 (2018) 705-715.
[86] Z. Wang, S. Yun, X. Wang, C. Wang, Y. Si, Y. Zhang, H. Xu, Aloe peel-derived honeycomb-like bio-based carbon with controllable morphology and its superior electrochemical properties for new energy devices, Ceramics International, 45 (2019) 4208-4218.
[87] W. Lu, X. Cao, L. Hao, Y. Zhou, Y. Wang, Activated carbon derived from pitaya peel for supercapacitor applications with high capacitance performance, Materials Letters, 264 (2020) 127339.
[88] T. Purkait, G. Singh, M. Singh, D. Kumar, R.S. Dey, Large area few-layer graphene with scalable preparation from waste biomass for high-performance supercapacitor, Scientific reports, 7 (2017) 1-14.
[89] L. Qin, Z. Hou, S. Lu, S. Liu, Z. Liu, E. Jiang, Porous carbon derived from pine nut shell prepared by steam activation for supercapacitor electrode material, Int. J. Electrochem. Sci, 14 (2019) 907-908.
[90] R. Srinivasan, E. Elaiyappillai, H.P. Pandian, R. Vengudusamy, P.M. Johnson, S.-M. Chen, R. Karvembu, Sustainable porous activated carbon from Polyalthia longifolia seeds as electrode material for supercapacitor application, Journal of Electroanalytical Chemistry, 849 (2019) 113382.
[91] N. Guo, M. Li, Y. Wang, X. Sun, F. Wang, R. Yang, Soybean root-derived hierarchical porous carbon as electrode material for high-performance supercapacitors in ionic liquids, ACS applied materials & interfaces, 8 (2016) 33626-33634.
[92] L.K. de Souza, J.C. Martins, D.P. Oliveira, C.S. Ferreira, A.A. Goncalves, R.O. Araujo, J. da Silva Chaar, M.J. Costa, D.V. Sampaio, R.R. Passos, Hierarchical porous carbon derived from acai seed biowaste for supercapacitor electrode materials, Journal of Materials Science: Materials in Electronics, 31 (2020) 12148-12157.
[93] C. Huang, T. Sun, D. Hulicova-Jurcakova, Wide electrochemical window of supercapacitors from coffee bean-derived phosphorus-rich carbons, ChemSusChem, 6 (2013) 2330-2339.
[94] J. Choi, C. Zequine, S. Bhoyate, W. Lin, X. Li, P. Kahol, R. Gupta, Waste coffee management: deriving high-performance supercapacitors using nitrogen-doped coffee-derived carbon, C, 5 (2019) 44.
[95] Z. Yang, M. Xiang, Z. Wu, J. Hui, Q. Huang, J. Zhang, H. Qin, A three-dimensional carbon electrode derived from bean sprout for supercapacitors, Ionics, 26 (2020) 5705-5714.
[96] A. Elmouwahidi, E. Bailón-García, A.F. Pérez-Cadenas, F.J. Maldonado-Hódar, F. Carrasco-Marín, Activated carbons from KOH and H3PO4-activation of olive residues and its application as supercapacitor electrodes, Electrochimica Acta, 229 (2017) 219-228.
[97] Coal – Statistical Review of World Energy 2021 - BP.
[98] H. Nalbandian, P. House, Non-fuel uses of coal, IEA Coal Research Center, London, UK, (2014).
[99] J. Voncken, The Origin and Classification of Coal, Geology of Coal Deposits of South Limburg, The Netherlands, Springer2020, pp. 25-40.

[100] X.-Y. Zhao, S.-S. Huang, J.-P. Cao, S.-C. Xi, X.-Y. Wei, J. Kamamoto, T. Takarada, KOH activation of a HyperCoal to develop activated carbons for electric double-layer capacitors, Journal of analytical and applied pyrolysis, 105 (2014) 116-121.
[101] M. Shi, Y. Xin, X. Chen, K. Zou, W. Jing, J. Sun, Y. Chen, Y. Liu, Coal-derived porous activated carbon with ultrahigh specific surface area and excellent electrochemical performance for supercapacitors, Journal of Alloys and Compounds, 859 (2021) 157856.
[102] Z. Peng, Z. Guo, W. Chu, M. Wei, Facile synthesis of high-surface-area activated carbon from coal for supercapacitors and high CO 2 sorption, RSC advances, 6 (2016) 42019-42028.
[103] L. Wang, F. Sun, F. Hao, Z. Qu, J. Gao, M. Liu, K. Wang, G. Zhao, Y. Qin, A green trace K2CO3 induced catalytic activation strategy for developing coal-converted activated carbon as advanced candidate for CO2 adsorption and supercapacitors, Chemical Engineering Journal, 383 (2020) 123205.
[104] D. Liu, B. Xu, J. Zhu, S. Tang, F. Xu, S. Li, B. Jia, G. Chen, Preparation of highly porous graphitic activated carbon as electrode materials for supercapacitors by hydrothermal pretreatment-assisted chemical activation, ACS omega, 5 (2020) 11058-11067.
[105] K. Kierzek, E. Frackowiak, G. Lota, G. Gryglewicz, J. Machnikowski, Electrochemical capacitors based on highly porous carbons prepared by KOH activation, Electrochimica Acta, 49 (2004) 515-523.
[106] F. Sun, J. Gao, Y. Yang, Y. Zhu, L. Wang, X. Pi, X. Liu, Z. Qu, S. Wu, Y. Qin, One-step ammonia activation of Zhundong coal generating nitrogen-doped microporous carbon for gas adsorption and energy storage, Carbon, 109 (2016) 747-754.
[107] M. Guo, J. Guo, F. Tong, D. Jia, W. Jia, J. Wu, L. Wang, Z. Sun, Hierarchical porous carbon spheres constructed from coal as electrode materials for high performance supercapacitors, RSC advances, 7 (2017) 45363-45368.
[108] T. Pei, F. Sun, J. Gao, L. Wang, X. Pi, Z. Qie, G. Zhao, Introducing catalytic gasification into chemical activation for the conversion of natural coal into hierarchically porous carbons with broadened pore size for enhanced supercapacitive utilization, RSC advances, 8 (2018) 37880-37889.
[109] L. Wang, F. Sun, J. Gao, X. Pi, T. Pei, Z. Qie, G. Zhao, Y. Qin, A novel melt infiltration method promoting porosity development of low-rank coal derived activated carbon as supercapacitor electrode materials, Journal of the Taiwan Institute of Chemical Engineers, 91 (2018) 588-596.
[110] D. Dong, Y. Zhang, T. Wang, J. Wang, C.E. Romero, W.-p. Pan, Enhancing the pore wettability of coal-based porous carbon as electrode materials for high performance supercapacitors, Materials Chemistry and Physics, 252 (2020) 123381.
[111] Y. Lv, L. Ding, X. Wu, N. Guo, J. Guo, S. Hou, F. Tong, D. Jia, H. Zhang, Coal-based 3D hierarchical porous carbon aerogels for high performance and super-long life supercapacitors, Scientific reports, 10 (2020) 1-11.
[112] H. Wang, C. Zhou, H. Zhu, Y. Li, S. Wang, K. Shen, Hierarchical porous carbons from carboxylated coal-tar pitch functional poly (acrylic acid) hydrogel networks for supercapacitor electrodes, RSC Advances, 10 (2020) 1095-1103.
[113] S. Guo, B. Guo, R. Ma, Y. Zhu, J. Wang, KOH activation of coal-derived microporous carbons for oxygen reduction and supercapacitors, RSC Advances, 10 (2020) 15707-15714.
[114] C. Zhang, D. Long, B. Xing, W. Qiao, R. Zhang, L. Zhan, X. Liang, L. Ling, The superior electrochemical performance of oxygen-rich activated carbons prepared from bituminous coal, Electrochemistry Communications, 10 (2008) 1809-1811.
[115] X.-j. He, X.-j. Li, X.-t. Wang, N. Zhao, M.-x. Yu, M.-b. Wu, Efficient preparation of porous carbons from coal tar pitch for high performance supercapacitors, New Carbon Materials, 29 (2014) 493-502.
[116] T. Guan, K. Li, J. Zhao, R. Zhao, G. Zhang, D. Zhang, J. Wang, Template-free preparation of layer-stacked hierarchical porous carbons from coal tar pitch for high performance all-solid-state supercapacitors, Journal of Materials Chemistry A, 5 (2017) 15869-15878.

[117] M.R. Lukatskaya, J.I. Feldblyum, D.G. Mackanic, F. Lissel, D.L. Michels, Y. Cui, Z. Bao, Concentrated mixed cation acetate “water-in-salt” solutions as green and low-cost high voltage electrolytes for aqueous batteries, Energy & Environmental Science, 11 (2018) 2876-2883.
[118] J. Shao, F. Ma, G. Wu, C. Dai, W. Geng, S. Song, J. Wan, In-situ MgO (CaCO3) templating coupled with KOH activation strategy for high yield preparation of various porous carbons as supercapacitor electrode materials, Chemical Engineering Journal, 321 (2017) 301-313.
[119] X.-t. Wang, H. Ma, X.-j. He, J.-x. Wang, J.-f. Han, Y. Wang, Fabrication of interconnected mesoporous carbon sheets for use in high-performance supercapacitors, New Carbon Materials, 32 (2017) 213-220.
[120] D. Liu, X. Zhao, R. Su, Z. Hao, B. Jia, S. Li, L. Dong, Highly Porous Graphitic Activated Carbons from Lignite via Microwave Pretreatment and Iron-Catalyzed Graphitization at Low-Temperature for Supercapacitor Electrode Materials, Processes, 7 (2019) 300.
[121] S. Tan, T.J. Kraus, K.D. Li-Oakey, Understanding the supercapacitor properties of electrospun carbon nanofibers from Powder River Basin coal, Fuel, 245 (2019) 148-159.
[122] H. Wang, H. Zhu, S. Wang, D. Qi, K. Shen, Dicarbonyl-tuned microstructures of hierarchical porous carbons derived from coal-tar pitch for supercapacitor electrodes, RSC Advances, 9 (2019) 20019-20028.
[123] Q.-Q. Zhuang, J.-P. Cao, X.-Y. Zhao, Y. Wu, Z. Zhou, M. Zhao, Y.-P. Zhao, X.-Y. Wei, Preparation of layered-porous carbon from coal tar pitch narrow fractions by single-solvent extraction for superior cycling stability electric double layer capacitor application, Journal of Colloid and Interface Science, 567 (2020) 347-356.
[124] Y. Yang, H. Niu, F. Qin, Z. Guo, J. Wang, G. Ni, P. Zuo, S. Qu, W. Shen, MnO2 doped carbon nanosheets prepared from coal tar pitch for advanced asymmetric supercapacitor, Electrochimica Acta, 354 (2020) 136667.
[125] J. Hao, X. Wang, Y. Wang, X. Lai, Q. Guo, J. Zhao, Y. Yang, Y. Li, Hierarchical structure N, O-co-doped porous carbon/carbon nanotube composite derived from coal for supercapacitors and CO2 capture, Nanoscale Advances, 2 (2020) 878-887.
[126] Y. Ding, T. Wang, D. Dong, Y. Zhang, Using Biochar and Coal as the Electrode Material for Supercapacitor Applications, Frontiers in Energy Research, 7 (2020).
[127] J.V.S. Moreira, E.J. Corat, P.W. May, L.D.R. Cardoso, P.A. Lelis, H. Zanin, Freestanding aligned multi-walled carbon nanotubes for supercapacitor devices, Journal of electronic materials, 45 (2016) 5781-5788.
[128] MARKET RESEARCH REPORT, 2021.
[129] G. Wang, L. Zhang, J. Zhang, A review of electrode materials for electrochemical supercapacitors, Chemical Society Reviews, 41 (2012) 797-828.
[130] A. González, E. Goikolea, J.A. Barrena, R. Mysyk, Review on supercapacitors: Technologies and materials, Renewable and Sustainable Energy Reviews, 58 (2016) 1189-1206.
[131] M. Sajjad, M.I. Khan, F. Cheng, W. Lu, A review on selection criteria of aqueous electrolytes performance evaluation for advanced asymmetric supercapacitors, Journal of Energy Storage, 40 (2021) 102729.
[132] J. Huang, K. Yuan, Y. Chen, Wide Voltage Aqueous Asymmetric Supercapacitors: Advances, Strategies, and Challenges, Advanced Functional Materials, (2021) 2108107.
[133] C. Xu, G. Yang, D. Wu, M. Yao, C. Xing, J. Zhang, H. Zhang, F. Li, Y. Feng, S. Qi, Roadmap on Ionic Liquid Electrolytes for Energy Storage Devices, Chemistry–An Asian Journal, 16 (2021) 549-562.
[134] T. Abdallah, D. Lemordant, B. Claude-Montigny, Are room temperature ionic liquids able to improve the safety of supercapacitors organic electrolytes without degrading the performances?, Journal of power sources, 201 (2012) 353-359.
[135] P. Wasserscheid, W. Keim, Ionic liquids—new “solutions” for transition metal catalysis, Angewandte Chemie International Edition, 39 (2000) 3772-3789.

[136] T. Welton, Room-temperature ionic liquids. Solvents for synthesis and catalysis, Chemical reviews, 99 (1999) 2071-2084.
[137] H. Liu, H. Yu, Ionic liquids for electrochemical energy storage devices applications, Journal of materials science & technology, 35 (2019) 674-686.
[138] T. Stettner, A. Balducci, Protic ionic liquids in energy storage devices: Past, present and future perspective, Energy Storage Materials, 40 (2021) 402-414.
[139] M. Galiński, A. Lewandowski, I. Stępniak, Ionic liquids as electrolytes, Electrochimica acta, 51 (2006) 5567-5580.
[140] S. Brunauer, P.H. Emmett, E. Teller, Adsorption of gases in multimolecular layers, Journal of the American chemical society, 60 (1938) 309-319.
[141] M. Thommes, K. Kaneko, A.V. Neimark, J.P. Olivier, F. Rodriguez-Reinoso, J. Rouquerol, K.S. Sing, Physisorption of gases, with special reference to the evaluation of surface area and pore size distribution (IUPAC Technical Report), Pure and applied chemistry, 87 (2015) 1051-1069.
[142] I. Langmuir, The constitution and fundamental properties of solids and liquids. Part I. Solids, Journal of the American chemical society, 38 (1916) 2221-2295.
[143] https://en.wikipedia.org/wiki/Molecular_dynamics.
[144] I. Yut, A. Zofka, Attenuated total reflection (ATR) Fourier transform infrared (FT-IR) spectroscopy of oxidized polymer-modified bitumens, Applied spectroscopy, 65 (2011) 765-770.
[145] B.H. Stuart, Infrared spectroscopy: fundamentals and applications, John Wiley & Sons2004.
[146] S. Zhang, N. Pan, Supercapacitors performance evaluation, Advanced Energy Materials, 5 (2015) 1401401.
[147] Y. Shao, M.F. El-Kady, J. Sun, Y. Li, Q. Zhang, M. Zhu, H. Wang, B. Dunn, R.B. Kaner, Design and mechanisms of asymmetric supercapacitors, Chemical reviews, 118 (2018) 9233-9280.
[148] B.K. Kim, S. Sy, A. Yu, J. Zhang, Electrochemical supercapacitors for energy storage and conversion, Handbook of clean energy systems, (2015) 1-25.
[149] M.D. Stoller, R.S. Ruoff, Best practice methods for determining an electrode material's performance for ultracapacitors, Energy & Environmental Science, 3 (2010) 1294-1301.
[150] J. Gamby, P. Taberna, P. Simon, J. Fauvarque, M. Chesneau, Studies and characterisations of various activated carbons used for carbon/carbon supercapacitors, Journal of power sources, 101 (2001) 109-116.
[151] K. Wang, N. Zhao, S. Lei, R. Yan, X. Tian, J. Wang, Y. Song, D. Xu, Q. Guo, L. Liu, Promising biomass-based activated carbons derived from willow catkins for high performance supercapacitors, Electrochimica Acta, 166 (2015) 1-11.
[152] M. Olivares-Marín, J.A. Fernández, M.J. Lázaro, C. Fernández-González, A. Macías-García, V. Gómez-Serrano, F. Stoeckli, T.A. Centeno, Cherry stones as precursor of activated carbons for supercapacitors, Materials Chemistry and Physics, 114 (2009) 323-327.
[153] W.-H. Qu, Y.-Y. Xu, A.-H. Lu, X.-Q. Zhang, W.-C. Li, Converting biowaste corncob residue into high value added porous carbon for supercapacitor electrodes, Bioresource technology, 189 (2015) 285-291.
[154] P. Yang, J. Xie, C. Zhong, Biowaste-derived three-dimensional porous network carbon and bioseparator for high-performance asymmetric supercapacitor, ACS Applied Energy Materials, 1 (2018) 616-622.
[155] R.S. Varma, Biomass-derived renewable carbonaceous materials for sustainable chemical and environmental applications, ACS sustainable chemistry & engineering, 7 (2019) 6458-6470.
[156] J. Wang, X. Zhang, Z. Li, Y. Ma, L. Ma, Recent progress of biomass-derived carbon materials for supercapacitors, Journal of Power Sources, 451 (2020) 227794.
[157] C.-S. Yang, Y.S. Jang, H.K. Jeong, Bamboo-based activated carbon for supercapacitor applications, Current Applied Physics, 14 (2014) 1616-1620.
[158] W. Tian, Q. Gao, Y. Tan, K. Yang, L. Zhu, C. Yang, H. Zhang, Bio-inspired beehive-like hierarchical nanoporous carbon derived from bamboo-based industrial by-product as a high

performance supercapacitor electrode material, Journal of Materials Chemistry A, 3 (2015) 5656-5664.
[159] X. Yu, Y. Wang, L. Li, H. Li, Y. Shang, Soft and wrinkled carbon membranes derived from petals for flexible supercapacitors, Scientific reports, 7 (2017) 1-8.
[160] D. Ma, G. Wu, J. Wan, F. Ma, W. Geng, S. Song, Oxygen-enriched hierarchical porous carbon derived from biowaste sunflower heads for high-performance supercapacitors, RSC advances, 5 (2015) 107785-107792.
[161] T.E. Rufford, D. Hulicova-Jurcakova, K. Khosla, Z. Zhu, G.Q. Lu, Microstructure and electrochemical double-layer capacitance of carbon electrodes prepared by zinc chloride activation of sugar cane bagasse, Journal of Power Sources, 195 (2010) 912-918.
[162] X. Su, S. Jiang, X. Zheng, X. Guan, P. Liu, Z. Peng, Hierarchical porous carbon materials from bio waste-mango stone for high-performance supercapacitor electrodes, Materials Letters, 230 (2018) 123-127.
[163] J. Mi, X.-R. Wang, R.-J. Fan, W.-H. Qu, W.-C. Li, Coconut-shell-based porous carbons with a tunable micro/mesopore ratio for high-performance supercapacitors, Energy & Fuels, 26 (2012) 5321-5329.
[164] C. Wu, S. Yang, J. Cai, Q. Zhang, Y. Zhu, K. Zhang, Activated microporous carbon derived from almond shells for high energy density asymmetric supercapacitors, ACS applied materials & interfaces, 8 (2016) 15288-15296.
[165] (UNESCO - Argan, practices and know-how concerning the argan tree, (2014).).
[166] F. Khallouki, R. Haubner, I. Ricarte, G. Erben, K. Klika, C.M. Ulrich, R.W. Owen, Identification of polyphenolic compounds in the flesh of Argan (Morocco) fruits, Food chemistry, 179 (2015) 191-198.
[167] B. Matthäus, D. Guillaume, S. Gharby, A. Haddad, H. Harhar, Z. Charrouf, Effect of processing on the quality of edible argan oil, Food chemistry, 120 (2010) 426-432.
[168] T. Chafik, Nanoporous carbonated materials prepared from the shell of the argan fruit 1–14, 2012.
[169] M. Dahbi, M. Kiso, K. Kubota, T. Horiba, T. Chafik, K. Hida, T. Matsuyama, S. Komaba, Synthesis of hard carbon from argan shells for Na-ion batteries, Journal of Materials Chemistry A, 5 (2017) 9917-9928.
[170] V. Boonamnuayvitaya, S. Sae-ung, W. Tanthapanichakoon, Preparation of activated carbons from coffee residue for the adsorption of formaldehyde, Separation and purification technology, 42 (2005) 159-168.
[171] C. Pongener, D. Kibami, K. Rao, R. Goswamee, D. Sinha, Adsorption studies of fluoride by activated carbon prepared from Mucuna prurines plant, Journal of Water Chemistry and Technology, 39 (2017) 108-115.
[172] D. Prahas, Y. Kartika, N. Indraswati, S. Ismadji, Activated carbon from jackfruit peel waste by H3PO4 chemical activation: Pore structure and surface chemistry characterization, Chemical Engineering Journal, 140 (2008) 32-42.
[173] N. Yoshizawa, K. Maruyama, Y. Yamada, E. Ishikawa, M. Kobayashi, Y. Toda, M. Shiraishi, XRD evaluation of KOH activation process and influence of coal rank, Fuel, 81 (2002) 1717-1722.
[174] Y. Zhu, S. Murali, M.D. Stoller, K. Ganesh, W. Cai, P.J. Ferreira, A. Pirkle, R.M. Wallace, K.A. Cychosz, M. Thommes, Carbon-based supercapacitors produced by activation of graphene, science, 332 (2011) 1537-1541.
[175] A.C. Ferrari, J. Robertson, Interpretation of Raman spectra of disordered and amorphous carbon, Physical review B, 61 (2000) 14095.
[176] J. Sun, J. Niu, M. Liu, J. Ji, M. Dou, F. Wang, Biomass-derived nitrogen-doped porous carbons with tailored hierarchical porosity and high specific surface area for high energy and power density supercapacitors, Applied Surface Science, 427 (2018) 807-813.

[177] J. Vatamanu, M. Vatamanu, D. Bedrov, Non-faradaic energy storage by room temperature ionic liquids in nanoporous electrodes, ACS nano, 9 (2015) 5999-6017.
[178] X. Li, C. Han, X. Chen, C. Shi, Preparation and performance of straw based activated carbon for supercapacitor in non-aqueous electrolytes, Microporous and Mesoporous Materials, 131 (2010) 303-309.
[179] E.E. Miller, Y. Hua, F.H. Tezel, Materials for energy storage: Review of electrode materials and methods of increasing capacitance for supercapacitors, Journal of Energy Storage, 20 (2018) 30-40.
[180] P. Taberna, P. Simon, J.-F. Fauvarque, Electrochemical characteristics and impedance spectroscopy studies of carbon-carbon supercapacitors, Journal of the Electrochemical Society, 150 (2003) A292.
[181] B.K. Saikia, S.M. Benoy, M. Bora, J. Tamuly, M. Pandey, D. Bhattacharya, A brief review on supercapacitor energy storage devices and utilization of natural carbon resources as their electrode materials, Fuel, 282 (2020) 118796.
[182] M. Mastragostino, C. Arbizzani, F. Soavi, Conducting polymers as electrode materials in supercapacitors, Solid state ionics, 148 (2002) 493-498.
[183] Y. Zhou, W. Guo, T. Li, A review on transition metal nitrides as electrode materials for supercapacitors, Ceramics International, 45 (2019) 21062-21076.
[184] M.A.A.M. Abdah, N.H.N. Azman, S. Kulandaivalu, Y. Sulaiman, Review of the use of transition-metal-oxide and conducting polymer-based fibres for high-performance supercapacitors, Materials & Design, 186 (2020) 108199.
[185] Y. Han, Z. Lai, Z. Wang, M. Yu, Y. Tong, X. Lu, Designing carbon based supercapacitors with high energy density: a summary of recent progress, Chemistry–A European Journal, 24 (2018) 7312-7329.
[186] X.-Q. LI, L. CHANG, S.-L. ZHAO, C.-L. HAO, C.-G. LU, Y.-H. ZHU, Z.-Y. TANG, Research on carbon-based electrode materials for supercapacitors, Acta Physico-Chimica Sinica, 33 (2017) 130-148.
[187] F. Ran, X. Yang, L. Shao, Recent progress in carbon-based nanoarchitectures for advanced supercapacitors, Advanced Composites and Hybrid Materials, 1 (2018) 32-55.
[188] L.L. Zhang, X. Zhao, Carbon-based materials as supercapacitor electrodes, Chemical Society Reviews, 38 (2009) 2520-2531.
[189] A. Linares-Solano, M.A. Lillo-Rodenas, J.P. Marco Lozar, M. Kunowsky, A.J. Romero Anaya, NaOH and KOH for preparing activated carbons used in energy and environmental applications, (2012).
[190] J.M. Andrésen, C.E. Burgess, P.J. Pappano, H.H. Schobert, New directions for non-fuel uses of anthracites, Fuel processing technology, 85 (2004) 1373-1392.
[191] S. Xiong, J. Fan, Y. Wang, J. Zhu, J. Yu, Z. Hu, A facile template approach to nitrogen-doped hierarchical porous carbon nanospheres from polydopamine for high-performance supercapacitors, Journal of Materials Chemistry A, 5 (2017) 18242-18252.
[192] D. Hulicova-Jurcakova, M. Seredych, G.Q. Lu, T.J. Bandosz, Combined effect of nitrogen-and oxygen-containing functional groups of microporous activated carbon on its electrochemical performance in supercapacitors, Advanced functional materials, 19 (2009) 438-447.
[193] Z. Zapata-Benabithe, C. Moreno-Castilla, F. Carrasco-Marín, Effect of dilution ratio and drying method of resorcinol–formaldehyde carbon gels on their electrocapacitive properties in aqueous and non-aqueous electrolytes, Journal of Sol-Gel Science and Technology, 75 (2015) 407-412.
[194] V. Ruiz, T. Huynh, S.R. Sivakkumar, A. Pandolfo, Ionic liquid–solvent mixtures as supercapacitor electrolytes for extreme temperature operation, RSC advances, 2 (2012) 5591-5598.
[195] M. Ue, K. Ida, S. Mori, Electrochemical properties of organic liquid electrolytes based on quaternary onium salts for electrical double-layer capacitors, Journal of the Electrochemical Society, 141 (1994) 2989.

[196] C. Zequine, C. Ranaweera, Z. Wang, S. Singh, P. Tripathi, O. Srivastava, B.K. Gupta, K. Ramasamy, P. Kahol, P. Dvornic, High per formance and flexible supercapacitors based on carbonized bamboo fibers for wide temperature applications, Scientific reports, 6 (2016) 1-10.
[197] A. Balducci, Electrolytes for high voltage electrochemical double layer capacitors: A perspective article, Journal of Power Sources, 326 (2016) 534-540.
[198] R. Younesi, G.M. Veith, P. Johansson, K. Edström, T. Vegge, Lithium salts for advanced lithium batteries: Li–metal, Li–O 2, and Li–S, Energy & Environmental Science, 8 (2015) 1905-1922.
[199] V. Sharova, A. Moretti, T. Diemant, A. Varzi, R.J. Behm, S. Passerini, Comparative study of imide-based Li salts as electrolyte additives for Li-ion batteries, Journal of Power Sources, 375 (2018) 43-52.
[200] L. Dagousset, G.T. Nguyen, F. Vidal, C. Galindo, P.-H. Aubert, Ionic liquids and γ-butyrolactone mixtures as electrolytes for supercapacitors operating over extended temperature ranges, RSC advances, 5 (2015) 13095-13101.
[201] L. Suo, O. Borodin, T. Gao, M. Olguin, J. Ho, X. Fan, C. Luo, C. Wang, K. Xu, "Water-in-salt" electrolyte enables high-voltage aqueous lithium-ion chemistries, Science, 350 (2015) 938-943.
[202] D.P. Leonard, Z. Wei, G. Chen, F. Du, X. Ji, Water-in-salt electrolyte for potassium-ion batteries, ACS Energy Letters, 3 (2018) 373-374.
[203] X. Bu, L. Su, Q. Dou, S. Lei, X. Yan, A low-cost "water-in-salt" electrolyte for a 2.3 V high-rate carbon-based supercapacitor, Journal of Materials Chemistry A, 7 (2019) 7541-7547.
[204] L. Xia, L. Yu, D. Hu, G.Z. Chen, Electrolytes for electrochemical energy storage, Materials Chemistry Frontiers, 1 (2017) 584-618.
[205] J. Zhang, X. Yao, R.K. Misra, Q. Cai, Y. Zhao, Progress in electrolytes for beyond-lithium-ion batteries, Journal of Materials Science & Technology, 44 (2020) 237-257.
[206] T.P.T. Pham, C.-W. Cho, Y.-S. Yun, Environmental fate and toxicity of ionic liquids: a review, Water research, 44 (2010) 352-372.
[207] Y. Yamada, J. Wang, S. Ko, E. Watanabe, A. Yamada, Advances and issues in developing salt-concentrated battery electrolytes, Nature Energy, 4 (2019) 269-280.
[208] P. Lannelongue, R. Bouchal, E. Mourad, C. Bodin, M. Olarte, S. Le Vot, F. Favier, O. Fontaine, "Water-in-Salt" for supercapacitors: a compromise between voltage, power density, energy density and stability, Journal of The Electrochemical Society, 165 (2018) A657.
[209] L. Suo, F. Han, X. Fan, H. Liu, K. Xu, C. Wang, "Water-in-Salt" electrolytes enable green and safe Li-ion batteries for large scale electric energy storage applications, Journal of Materials Chemistry A, 4 (2016) 6639-6644.
[210] Q. Dou, S. Lei, D.-W. Wang, Q. Zhang, D. Xiao, H. Guo, A. Wang, H. Yang, Y. Li, S. Shi, Safe and high-rate supercapacitors based on an "acetonitrile/water in salt" hybrid electrolyte, Energy & Environmental Science, 11 (2018) 3212-3219.
[211] Z. Tian, W. Deng, X. Wang, C. Liu, C. Li, J. Chen, M. Xue, R. Li, F. Pan, Superconcentrated aqueous electrolyte to enhance energy density for advanced supercapacitors, Functional Materials Letters, 10 (2017) 1750081.
[212] R.M. Maier, T.J. Gentry, Microorganisms and organic pollutants, Environmental microbiology, Elsevier2015, pp. 377-413.
[213] J.A. Maier, C. Martinez, K. Kasavajhala, L. Wickstrom, K.E. Hauser, C. Simmerling, ff14SB: improving the accuracy of protein side chain and backbone parameters from ff99SB, Journal of chemical theory and computation, 11 (2015) 3696-3713.
[214] M.W. Mahoney, W.L. Jorgensen, A five-site model for liquid water and the reproduction of the density anomaly by rigid, nonpolarizable potential functions, The Journal of chemical physics, 112 (2000) 8910-8922.
[215] D. Cerutti, T. Cheatham III, T. Darden, R. Duke, T. Giese, H. Gohlke, A. Goetz, N. Homeyer, S. Izadi, P. Janowski, AMBER 16, University of California: San Francisco, CA, (2016).

[216] D.R. Roe, T.E. Cheatham III, PTRAJ and CPPTRAJ: software for processing and analysis of molecular dynamics trajectory data, Journal of chemical theory and computation, 9 (2013) 3084-3095.
[217] Y. Korenblit, M. Rose, E. Kockrick, L. Borchardt, A. Kvit, S. Kaskel, G. Yushin, High-rate electrochemical capacitors based on ordered mesoporous silicon carbide-derived carbon, Acs Nano, 4 (2010) 1337-1344.
[218] A. Bello, F. Barzegar, M. Madito, D.Y. Momodu, A.A. Khaleed, T. Masikhwa, J.K. Dangbegnon, N. Manyala, Stability studies of polypyrole-derived carbon based symmetric supercapacitor via potentiostatic floating test, Electrochimica Acta, 213 (2016) 107-114.
[219] T.G. Pedersen, A. Hvidt, Volumetric effects due to ion-solvent interaction in aqueous electrolyte solutions, Carlsberg Research Communications, 50 (1985) 193.
[220] D.E. Goldsack, R. Franchetto, The viscosity of concentrated electrolyte solutions. I. Concentration dependence at fixed temperature, Canadian Journal of Chemistry, 55 (1977) 1062-1072.
[221] H. Peng, A.V. Nguyen, A link between viscosity and cation-anion contact pairs: Adventure on the concept of structure-making/breaking for concentrated salt solutions, Journal of Molecular Liquids, 263 (2018) 109-117.
[222] M. Kaminsky, Ion-solvent interaction and the viscosity of strong-electrolyte solutions, Discussions of the Faraday Society, 24 (1957) 171-179.
[223] M. Petrowsky, R. Frech, Salt concentration dependence of the compensated Arrhenius equation for alcohol-based electrolytes, Electrochimica Acta, 55 (2010) 1285-1288.
[224] S. Fang, L. Yang, J. Wang, M. Li, K. Tachibana, K. Kamijima, Ionic liquids based on functionalized guanidinium cations and TFSI anion as potential electrolytes, Electrochimica acta, 54 (2009) 4269-4273.
[225] N. NIST, Standard Reference Database 69: NIST Chemistry WebBook, National Institute of Standards and Technology, (2010).
[226] D. Ellerbrock, D.D. Macdonald, Passivity of titanium, part 1: film growth model diagnostics, Journal of Solid State Electrochemistry, 18 (2014) 1485-1493.
[227] W. Giurlani, L. Sergi, E. Crestini, N. Calisi, F. Poli, F. Soavi, M. Innocenti, Electrochemical stability of steel, Ti, and Cu current collectors in water-in-salt electrolyte for green batteries and supercapacitors, Journal of Solid State Electrochemistry, (2020) 1-11.
[228] M. Lazzari, F. Soavi, M. Mastragostino, High voltage, asymmetric EDLCs based on xerogel carbon and hydrophobic IL electrolytes, Journal of Power Sources, 178 (2008) 490-496.